ITALIAN INSTITUTE OF TECHNOLOGY

UNIVERSITY OF GENOVA

DOCTORAL THESIS

Design and Control of Compliant Actuation Topologies for Energy-Efficient Articulated Robots

---

Author:
Wesley ROOZING

Advisor:
Dr. Nikolaos G. TSAGARAKIS

A thesis submitted in partial fulfillment of the requirements
for the degree of Doctor of Philosophy

in the

Humanoids & Human Centered Mechatronics
Department of Advanced Robotics
Italian Institute of Technology

January 18, 2018

Humanoids & Human Centered Mechatronics
Department of Advanced Robotics
Italian Institute of Technology

Advisor: Dr. Nikolaos G. Tsagarakis

Examiners: Prof. x
Prof. y
Prof. z

Humanoids & Human Centered Mechatronics
Department of Advanced Robotics
Italian Institute of Technology
Via Morego 30, 16163 Genova, Italy
Tel.: +39 010 71781 481
Fax.: +39 010 71781 232

Department of Informatics, Bioengineering, Robotics, and System Engineering
University of Genova
Via All'Opera Pia 13, 16145 Genova, Italy
Tel.: +39 010 3532 983
Fax.: +39 010 3532 948

Department of Informatics, Bioengineering, Robotics, and
System Engineering (DIBRIS)
University of Genova

Declaration of Authorship

I, Wesley ROOZING, declare that this thesis titled, "Design and Control of Compliant Actuation Topologies for Energy-Efficient Articulated Robots" and the work presented in it are my own. I confirm that:

- This work was done wholly or mainly while in candidature for a research degree at this University.
- Where any part of this thesis has previously been submitted for a degree or any other qualification at this University or any other institution, this has been clearly stated.
- Where I have consulted the published work of others, this is always clearly attributed.
- Where I have quoted from the work of others, the source is always given. With the exception of such quotations, this thesis is entirely my own work.
- I have acknowledged all main sources of help.
- Where the thesis is based on work done by myself jointly with others, I have made clear exactly what was done by others and what I have contributed myself.

Signed:

_____

Date:

_____

"I was born not knowing and have had only a little time to change that here and there."

Richard P. Feynman

Abstract

Design and Control of Compliant Actuation Topologies for Energy-Efficient Articulated Robots

by Wesley ROOZING

Considerable advances have been made in the field of robotic actuation in recent years. At the heart of this has been increased use of compliance. Arguably the most common approach is that of Series-Elastic Actuation (SEA), and SEAs have evolved to become the core component of many articulated robots. Another approach is integration of compliance in parallel to the main actuation, referred to as Parallel-Elastic Actuation (PEA). A wide variety of such systems has been proposed. While both approaches have demonstrated significant potential benefits, a number of key challenges remain with regards to the design and control of such actuators.

This thesis addresses some of the challenges that exist in design and control of compliant actuation systems. First, it investigates the design, dynamics, and control of SEAs as the core components of next-generation robots. We consider the influence of selected physical stiffness on torque controllability and backdrivability, and propose an optimality criterion for impedance rendering. Furthermore, we consider disturbance observers for robust torque control. Simulation studies and experimental data validate the analyses. Secondly, this work investigates augmentation of articulated robots with adjustable parallel compliance and multi-articulated actuation for increased energy efficiency. Particularly, design optimisation of parallel compliance topologies with adjustable pretension is proposed, including multi-articulated arrangements. Novel control strategies are developed for such systems. To validate the proposed concepts, novel hardware is designed, simulation studies are performed, and experimental data of two platforms are provided, that show the benefits over state-of-the-art SEA-only based actuation.

Acknowledgements

The last years at the Italian Institute of Technology have been some of the most enjoyable, both professionally and personally. The institute has bestowed me with many opportunities and it truly is a great place for research.

First of all I would like to thank my advisor Nikolaos Tsagarakis, whose guidance has been invaluable throughout my time at IIT. His input on conceptual design, hardware, and scientific writing have made me a better researcher.

I would like to thank Zhibin Li, who played a key role during my first years at IIT. He encouraged me to push further, leading to my first journal publications. His advice on writing was very valuable and I still benefit from it today.

My discussions with my good friends Navvab Kashiri and Jörn Malzahn have been some of the most valuable throughout my career. Especially in the area of series-elastic actuators we have learned a lot from each other and it has been a pleasure collaborating with them.

Realisation of the new leg prototype would not have been possible without the help of Zeyu Ren. His skill in and insights into mechanical design have been crucial for development of the ideas into a real-world hardware. Many thanks also go out to the technicians, whom provided important support in fabrication and assistance with hardware, embedded electronics, and software.

Arash, Edwin, Jinoh, Luka, Martijn & Jana, Wansoo, and all the others, some of which have come and gone (life in academia), thank you, for making my life so much fun over the years.

Finally, thank you to Renske, who embarked with me on this journey and many others over the years, for her endless support and love.

Contents

List of Figures

List of Tables

List of Acronyms

ACA Asymmetric Compliant Actuation

BLDC Brush-Less Direct Current

CAD Computer–Aided Design

CJT Compliant Joint Toolbox

DSP Digital Signal Processor

DC Direct Current

DOB Disturbance Observer

DROC Disturbance observer Region Of Convergence

DoF Degree-of-Freedom

EMF Electro-Motive Force

ESB Energy Storage Branch

LPF Low-Pass Filter

PB Power Branch

PD Proportional Derivative

PEA Parallel Compliant Actuation

RMS Root Mean Square

SEA Series-Elastic Actuation

VSA Variable Stiffness Actuation

1

Introduction

One of the primary challenges in robotic actuation today is the development of high-performance energy efficient actuation concepts that allow for more efficient machines with larger capabilities and more autonomy. Recent years have seen a paradigm shift in the field of robotic actuation from stiff, mainly position controlled concepts to compliant actuators in force control. This paradigm shift has sparked significant discussion on how to design and control these actuators, and the search for high-performance energy efficient robotic actuators has resulted in rapid developments.

Many of the proposed concepts take inspiration from biological systems, in both their topology as well as the capacity for energy storage and release during motion. In robotic systems, they provide significant further benefits such as improved force control performance and physical robustness against impacts. This increased focus on use of compliance has taken place by addition of elastic elements both in series

with motor drives, and in parallel to the main actuation of robotic systems.

Arguably the most popular approach to the use of compliance in actuation has been that of SEA. SEAs have evolved to become the core component of many articulated robots, and they are finding their way into industry as commercial products as integrated actuation solutions. However, in the academic field, much discussion still exists as to how best to design and control such actuators. Many real-world scenarios involve articulated robots in unstructured environments, where demands are continuously changing and unexpected collisions are common. This requires their actuation systems to provide robustness both in terms of control performance and stability, as well as physical robustness.

To achieve these goals, many solutions have been proposed both in terms of design as well as control strategies. However, a number of open questions remain. Particularly, the level of physical compliance that is suitable and beneficial for a given application is unclear. Furthermore, the continuously changing environment provides unique challenges in terms of robust torque control of such actuators.

A different approach to the integration of compliance into robotic actuation is that of parallel compliance, commonly referred to as Parallel Compliant Actuation (PEA). In this field, a large variety of concepts has been proposed, ranging from simple static parallel springs to more complex topologies involving multiple overlapping branches, multi-articulation, and adjustability mechanisms. The latter has taken many forms such as variable transmission mechanisms, clutches/switches, and pretensioning mechanisms. While this concept has seen far less adoption than SEA due to some of its unique challenges, significant benefits have been demonstrated, particularly in terms of energy efficiency.

In contrast to research on SEA which has mostly focused on the single actuator level, the scope of PEA based research tends to encompass the system level, designing the actuation topology and its parameters based around the system of application. From this larger scope follows larger design freedom which has lead to some very interesting designs indeed. Particularly the synthesis of multi-articulated compliant actuation topologies with optimised design parameters is an interesting field with

many potential benefits demonstrated recently. However, much of this work is in its infancy, and it remains to be seen which of the concepts proposed in literature will survive the journey from lab prototype to broader real-world systems.

1.1 Objectives & Approach

This thesis addresses some of the existing challenges highlighted in the previous Section. Particularly, it:

1. investigates the design, dynamics, and control of SEAs as the core components of next-generation robots, and;
2. investigates the use of adjustable parallel compliance and multi-articulation in articulated robots for increased energy efficiency.

To achieve these objectives, we take a two-part approach. Part I considers the influence of design and control parameters on SEA dynamics, force control performance, output impedance, and backdrivability/transparency. Particularly, the influence of physical stiffness is investigated in-depth, as well as the application of disturbance observer based approaches for robust torque control of SEAs. Part II considers the augmentation of articulated robots, driven by SEAs, with the addition of adjustable parallel compliance, including multiple branches and multi-articulation. Starting with a single Degree-of-Freedom (DoF) proof-of-concept prototype leg, we gradually expand the concepts into multi-DoF, multi-articulation, advanced control methods, and a 3-DoF prototype leg which is used to effectively demonstrate the concepts on a real-world system.

Both parts of this thesis fall into the broader theme of high-performance and energy-efficient compliant robotic actuation. Therefore, the two parts are closely interconnected: series-elastic actuators are a core component of the concepts proposed in the second part. This is depicted graphically in Fig. 1.1, which gives an overview of the two parts and their constituent Chapters.

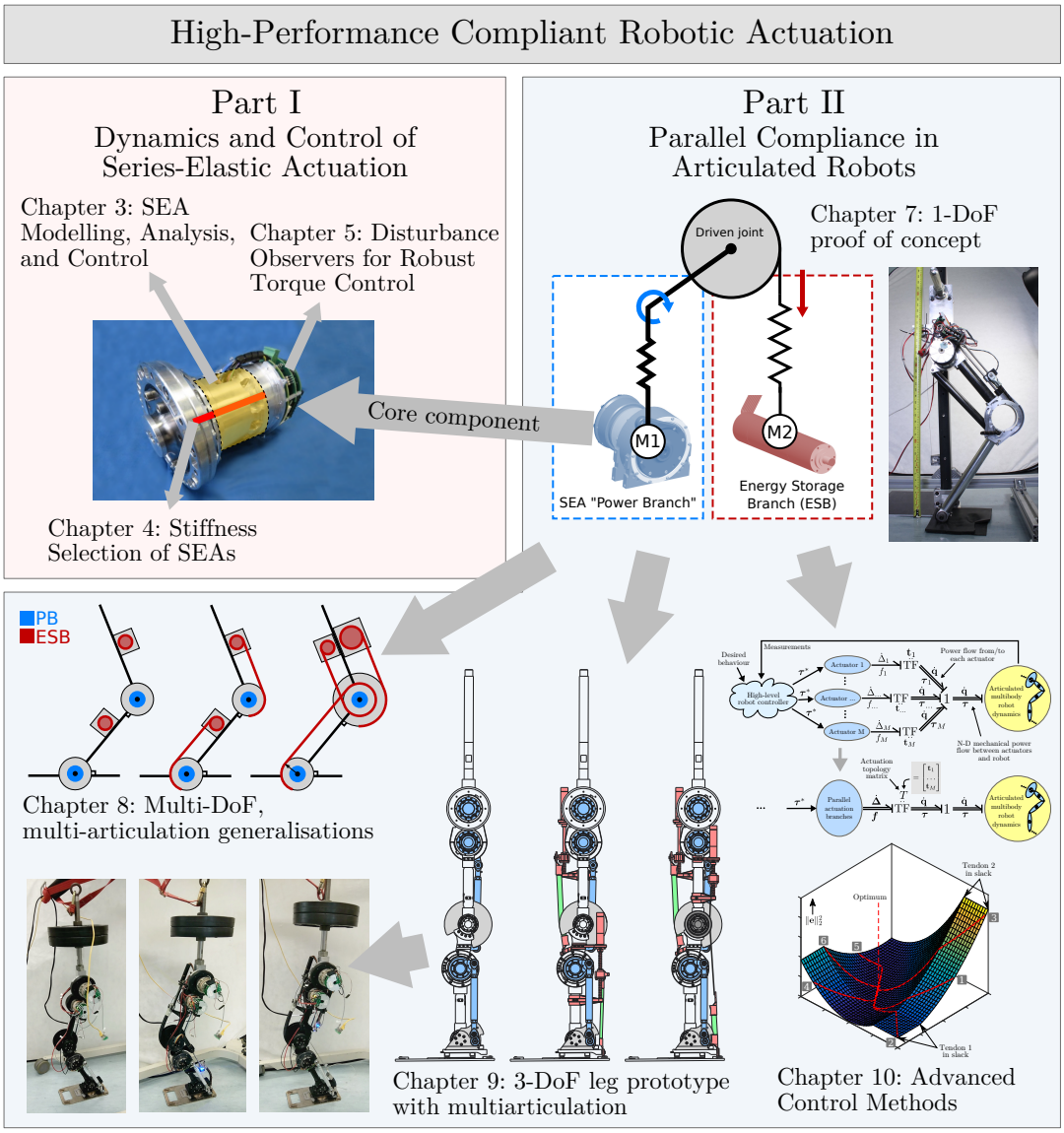

FIGURE 1.1: The Chapters of this thesis in the context of the overarching theme of high-performance compliant robotic actuation.

1.2 Contributions

This thesis presents a number of contributions, which we believe significantly extend the state-of-the-art in compliant robotic actuation. While they are elaborated on in more detail in the first Chapter of both parts (Chapters 2 and 6) in the context of existing literature, we briefly summarise them here.

Part I

- We consolidate several analyses on SEA dynamics and control, including the effects of active/passive compliance, on the performance of actuation drives

in terms of tracking zero and non-zero torques in the presence of load motion, as well as active impedance rendering;

- Based on this analysis, we propose a novel method for optimal stiffness selection, relying upon the trade-off between torque tracking bandwidth and backdrivability/transparency, thereby maximising the frequency up to which an impedance can be rendered accurately. To validate the analyses, we present simulations and experimental results;

- We analyse and compare two DOB based torque control configurations, demonstrating the equivalence of the two approaches in terms of robustness against disturbances and enforcing nominal dynamics of linear models. We present a simulation study on models of the SEAs of the WALK-MAN humanoid [1], [2], showing that both approaches significantly increase performance of the highly nonlinear system, but no significant difference exists between the two;

Part II

- Building on the previous work by Tsagarakis et al. [3], [4], we contribute on the modelling, tuning and control of a 1-DoF prototype leg with series and parallel elastic actuation for energy efficient operation, in a concept referred to as Asymmetric Compliant Actuation (ACA). Specifically, we propose a novel distributed control strategy which actively utilises both actuation branches and achieves significant energy efficiency improvements in both simulation and experimental validation;

- We extend and generalise the design and control concepts of ACA to multi-DoF systems and multi-articulated actuation topologies. A novel method is proposed for optimizing the parameters of these multi-DoF asymmetric compliant actuation configurations to improve their energy efficiency. A simulation study reports significant energy efficiency benefits in articulated robotic systems;

- On the basis of the aforementioned contributions, we introduce the novel design of a 3-DoF prototype leg with series and parallel compliant actuation, both

with monoarticulated and biarticulated parallel actuation topologies, which are rapidly interchangeable;

- Through an experimental comparison study on energetic performance using the 3-DoF prototype hardware, we provide initial indications on how the three actuation configurations affect the energetic economy of the leg. We present experimental results that illustrate the potential of the monoarticular and biarticular principles compared to state-of-the-art SEA actuation;
- We propose an elegant modular formulation that describes the energy exchange between actuation's compliant elements and articulated multi-body robot dynamics using power flows and a single matrix that describes the entire actuation topology. Using this formulation, we derive a novel gradient descent based control law for compliant actuation structures with adjustable pretension, with proven convexity for arbitrary actuation topologies. A simulation study on a model of the aforementioned 3-DoF leg prototype demonstrates the effectiveness of this control approach on multi-articulated compliant actuation topologies on articulated robots.

These contributions have been presented in a number of conference and journal publications, which are listed on page 149 of this thesis.

1.3 Attribution

As with all scientific works, the work presented in this thesis builds upon the work of others. An overview of the state-of-the-art in literature for both parts of this thesis is presented in Chapters 2 and 6. However, it is important to clarify where previous work ends and the work of this thesis began; the 1-DoF prototype leg hardware, considered in Chapter 7, was developed as part of previous work by Tsagarakis et al. [3], [4]. This work has been the foundation of the advancements presented in Part II of this thesis.

Furthermore, some of the work presented in this thesis has been the result of active collaboration with others, and their efforts should not go unnoticed:

- The modelling and identification of WALK-MAN joints (Sec. 3.1), as well as the development of the Compliant Joint Toolbox (CJT) for MATLAB/Simulink (Sec. 3.3), were part of a collaboration with Dr. Jörn Malzahn;
- The development of the actuation concepts, conceptual design, and design optimisation of the 3-DoF prototype leg (Chapter 9) were part of the work done for this thesis. However the Computer–Aided Design (CAD) and physical hardware realisation would not have been possible without the collaboration with Zeyu Ren.

1.4 Thesis Outline

This thesis consists of the following two Parts and their constituent Chapters.

Part I: Dynamics and Control of Series-Elastic Actuation

- **Chapter 2** provides an overview of the state-of-the-art in Series-Elastic Actuation and elaborates on the contributions provided by Part I in detail;
- **Chapter 3** formulates the prerequisites for Chapters 4 and 5, by introducing dynamics models and control of SEAs, and introducing the Compliant Joint Toolbox (CJT) for MATLAB/Simulink;
- **Chapter 4** considers stiffness selection of SEAs in the context of torque control, backdrivability/transparency, and impedance rendering;
- **Chapter 5** focuses on robust torque control of SEAs using disturbance observers;

Part II: Parallel Compliance in Articulated Robots

- **Chapter 6** discusses the state-of-the-art in literature on parallel compliance in articulated robots, and describes the contributions of Part II;
- **Chapter 7** presents the development of the distributed control strategy for the 1-DoF prototype leg;
- **Chapter 8** generalises and extends the concepts to multi-DoF and multi-articulation;

- **Chapter 9** introduces the design of the novel 3-DoF prototype leg with series and parallel compliant actuation;
- **Chapter 10** elaborates on the modular modelling approach of compliant actuation through energy exchange and presents the gradient descent based control law.

Chapter 11 concludes the thesis with a discussion of the results and suggestions on how future work may further develop the ideas presented in this work, followed by a list of conference and journal publications which are part of the dissemination of the contributions presented in this thesis.

A few final notes on form. First, with exception of the literature review Chapters 2 and 6 and the conclusions Chapter 11, each Chapter starts with a brief summary of its contents, followed by an outline of its constituent Sections. Secondly, Chapters end with a discussion of their results. Lastly, note that the mathematical notation for each Chapter in this thesis is self-contained, unless stated otherwise.

Part I

Dynamics and Control of Series-Elastic Actuation

2

Background, Related Work, and Contributions

Out of the compliant actuation concepts proposed in literature, compliance in series with the actuation drive, known as SEA and pioneered by Pratt in the 90's [5], has been the most widely adopted. SEAs have evolved to become the core component of many articulated robots [1], [5]–[14]. Pratt et al. demonstrated the beneficial properties of compliant actuation, including energy storage, interaction safety and improved force control. A mechanical torsion spring was placed in series with a stiff actuator, resulting in series-elastic actuation with constant intrinsic compliance. In that work, the authors suggested that investigations into designs with variable stiffness and those with parallel actuation branches could further improve performance. The latter suggestion is part of the focus of Part II of this thesis.

Other authors have since demonstrated that the SEA concept is able to significantly improve energy efficiency [15]–[18], peak output power [19], interaction safety [6],

[20], torque control performance and stability [21]–[23], and physical robustness [1].

In terms of energy efficiency benefits gained by adding series compliance, it has been shown that by tuning the joint compliance to the natural frequency of a system, the energy consumption can be significantly reduced while executing harmonic motions [18], [24]. However, for non-periodic tasks or multi-DoF systems in which the natural dynamics with respect to the joint are continuously changing, this approach is generally not feasible.

The addition of compliant behaviour into actuation indeed comes with increased complexity of dynamics and control, in some cases resulting from oscillations due to reduced bandwidth. In [25] the addition of variable physical damping to compliant actuators was studied to provide damping on demand, providing higher joint control performance. The authors showed the ability to change the damping ratio as desired on a single joint.

2.1 Variable Stiffness Actuators

Actuators with adjustable series compliance, commonly known as Variable Stiffness Actuation (VSA), have also been proposed in literature [17]–[20], [24], [26]–[29]. In [26] a lever arm connected to a linear spring was used to provide compliant coupling between two links. By setting the lever arm position and spring pretension independently, the equilibrium position and stiffness could be regulated independently. The design was improved in [18] by using a profiled cam instead of a lever arm, allowing to shape the deflection–torque profile. A design that uses two superimposed profiled cam mechanisms was proposed in [27]. The cams have a profile that combined with rollers extends an internal spring upon deflection. By moving one of the cams, the spring can be pretensioned to increase joint stiffness. The design described in [30] obtained a nonlinear stiffness characteristic by using nonlinear transmissions between the internal degrees of freedom and the output link, coupled by elastic elements. The authors also showed the intrinsic safety obtained with variable stiffness actuation by impact experiments. The design proposed in [28] varied the stiffness by changing the transmission ratio between the elastic elements and the output, instead

of pretensioning the elastic elements. This allowed to change the apparent output stiffness without changing the energy stored in the elastic elements. A similar design was proposed in [29] and it was shown that human-like ankle stiffness profiles from walking gait can be obtained.

While variable stiffness actuators show clear potential benefits, as evidenced by the results obtained in the above works, these have not been commonly demonstrated in real-world scenarios. The added design complexity combined with the poorly understood relation between stiffness level and performance results in many practical systems being designed with fixed series compliance actuators. This latter question of stiffness level has been considered in some works, as will be elaborated on in the next Section.

2.2 Stiffness Selection for SEAs

While the concept of Series Elastic Actuators was first introduced in the work of Pratt et al., torque controlled actuators have a longer history in literature. In a sense, any actuator can be considered compliant due to the finite rigidity of its structural components; indeed, by measuring the deformations of its internal components, even a "stiff" actuator can be seen as a compliant actuator that can be force controlled [7], [22], [31]. Therefore, the point at which a "stiff" actuator becomes a compliant actuator is not clear, and what level of compliance is suitable and beneficial for a given application is still an open research question. In recent literature the characterization of an actuator as compliant and its distinction from a stiff drive is mostly based on the *intentional* addition of compliance within the transmission system of the actuator. SEAs have have seen significant adoption in recent years, and throughout these works, very different stiffness values have been adopted, ranging roughly from 100 to 50,000 Nm/rad.

Some works that consider stiffness selection for SEAs exist. In [21] a dimensionless analysis was presented that investigates the influence of system parameters on torque control performance and output impedance. [32], [33] demonstrated how the presence of compliance enables stable force control in uncertain environments.

The influence of load motion on the torque tracking performance was investigated in [34]. In terms of impedance rendering, [22], [23] suggested that if passive operation is desired the selected mechanical stiffness should be higher than the rendered stiffness. However, while all these works provide guidelines in the form of upper or lower bounds of the mechanical stiffness, none of them provide optimalities with regards to for example energy efficiency or impedance rendering.

Important applications of force controlled actuators include interaction with humans and/or the environment, such as in rehabilitation [23] or assistive [11] devices, humanoids and field robots [1], [13], [14], [35], [36] meant to operate in partially known and unstructured workspaces, where unexpected collisions are common. Therefore, output impedance over the entire frequency range, not only the controllable torque bandwidth, is an important aspect of these actuators.

Conventional performance metrics for stiff actuators, such as closed-loop tracking bandwidth, do not seem as useful for compliant actuators. For example, the torque tracking bandwidth, commonly defined in fixed-output configuration, conveys only limited information about the output impedance or interaction performance of an actuator. Interaction performance can be defined as the actuator's ability to track desired torques in the presence of output motion. If the desired torque is zero, the output impedance consists of torques arising from backdriving the actuator. For these cases, we refer to the backdriving output impedance as the *transparency* of the actuator in this work.

Chapter 4 investigates the influence of the selected stiffness level and control parameters in a compliant actuation unit. The main contribution is a novel method for optimal stiffness selection, relying upon the trade-off between torque tracking bandwidth and transparency, thereby maximising the frequency up to which an impedance can be rendered accurately. To this end, it consolidates several analyses on SEA dynamics and control including the effects of active/passive compliance on the performance of actuation drives in terms of tracking zero and non-zero torques in the presence of load motion, as well as active impedance rendering. To validate the analyses, we present simulations and experimental results.

2.3 Disturbance Observers

One aspect that makes compliant actuators particularly interesting is their suitability for force/torque control. By regulating the deflection of the compliant element, the output torque of the actuator can be controlled with high fidelity. Many approaches to torque control for SEAs have been proposed, ranging from classical cascaded schemes [7], [8], [37] and optimal control approaches [9], to DOB based approaches [10]–[13], [38]–[41]. DOB-based approaches have gained in popularity recently due to the following two properties:

- rejection of unmodelled, unmeasured (external) disturbances to the system;
- ability to enforce nominal plant model dynamics onto the DOB augmented plant.

Frequently, the unmodelled plant dynamics are the nonlinear and possibly time variant actuator friction effects. These are sometimes rejected through friction compensation techniques; however, they are generally difficult to identify. Their rejection by means of a DOB greatly simplifies the controller design. Additionally, [13] showed that changes in dynamics to due variable output loads can be rejected. This is an important feature for multi-DoF articulated systems. Previous works [13], [39], [40] made efforts to analyse the robustness properties of DOB-based approaches, and [41] developed a technique to account for time delays in the plant.

In existing literature, the DOB has been applied to the torque control problem of SEAs in two configurations, which we refer to as *Open-loop DOB* and *Closed-loop DOB*:

- Open-loop DOB: applying the DOB to the plant only, enforcing a nominal plant model, the result of which is then controlled by an outer control loop [10], [38]–[41].
- Closed-loop DOB: including the controller dynamics into the nominal model and applying the DOB to plant+controller, thus enforcing closed-loop behaviour [11]–[13].

Chapter 5 compares these approaches for applying disturbance observers to the torque control problem of series elastic actuators. The contribution of the Chapter is threefold:

1. we analyse and compare both these DOB-based torque control configurations on models of the large-size SEAs of the WALK-MAN humanoid [1], [2];
2. we demonstrate the equivalence of the two approaches in terms of robustness against disturbances and enforcing nominal dynamics of linear models;
3. we present a simulation study showing that both approaches significantly increase performance of the highly nonlinear system, but no significant difference exists between the two.

Chapter 3 presents prerequisites for the work presented in Chapters 4 and 5. It introduces the linear and nonlinear dynamics models of SEAs used throughout these works, derives its torque dynamics and presents the control pole placement procedure. Furthermore, it provides an overview of the Compliant Joint Toolbox (CJT), an open-source MATLAB/Simulink based toolbox for rapid development of models and controllers for SEAs, which was developed as part of this work.

3

Modelling, Analysis & Control

This Chapter presents the prerequisites for the work presented in Chapters 4 and 5, and is structured as follows. Sec. 3.1 introduces the linear and nonlinear dynamics models of SEAs used throughout these works, and relevant simplifications. Sec. 3.2 derives its torque dynamics and presents the control pole placement procedure. Lastly, 3.3 provides an overview of the Compliant Joint Toolbox (CJT), an open-source MATLAB/Simulink based toolbox for rapid development of models and controllers for SEAs, which was developed as part of this work.

3.1 Modelling

3.1.1 Linear Dynamics

Fig. 3.1 shows the linear dynamics model of a general SEA. The model consists of motor rotor and gearbox inertiae I_m, I_g, coupled through a spring-damper element

with stiffness k_g and internal damping d_{mg}, modelling the finite rigidity of the Harmonic Drive gearbox. The gearbox inertia and load inertia I_l are coupled through the flexible transmission element, modelled as a spring-damper element with stiffness and internal damping k_b and d_{gl}. The inertiae experience viscous friction with the environment through bearings, with respective parameters d_m, d_g, d_l. We denote their positions as q_m, q_g, q_l respectively, and define the torques acting on the motor rotor due to winding current and on the load through environmental interaction as τ_m and τ_e respectively.

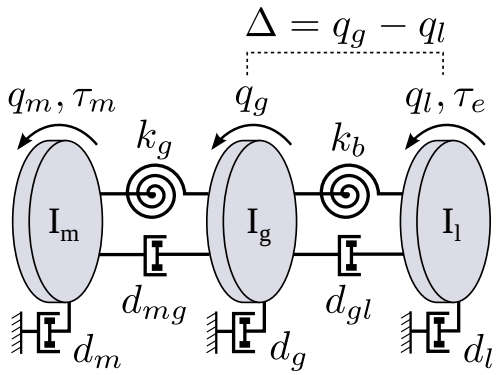

FIGURE 3.1: Linear Dynamics Model.

The equations of motion for the joint model of Fig. 3.1 are derived from the torque balance of each individual inertia:

$$\begin{aligned}
I_m\,\ddot{q}_m = \tau_m \quad & -d_m\,\dot{q}_m \quad && +d_{mg}\,(\dot{q}_g - \dot{q}_m) && +k_g\,(q_g - q_m) \\
I_g\,\ddot{q}_g = \quad & -d_g\,\dot{q}_g && -d_{mg}\,(\dot{q}_g - \dot{q}_m) && -k_g\,(q_g - q_m) \\
& && +d_{gl}\,(\dot{q}_l - \dot{q}_g) && +k_b\,(q_l - q_g) \\
I_l\,\ddot{q}_l = \tau_e \quad & -d_l\,\dot{q}_l && -d_{gl}\,(\dot{q}_l - \dot{q}_g) && -k_b\,(q_l - q_g)\,,
\end{aligned} \tag{3.1}$$

where $\tau_m = k_\tau\, n\, i_m$ is the torque generated by the winding current i_m, k_τ denotes the torque constant in Nm/A, and n denotes the gearbox transmission ratio. The motor rotor inertia and damping values are reflected across the gearbox by n^2 accordingly.

We explicitly define the deflection variable $\Delta = q_g - q_l$, and the torque transmitted to the load $\tau = k_b\,\Delta + d_{gl}\,\dot{\Delta}$. In estimating the torque for control, the damping component d_{gl} is usually ignored, i.e. $\tau \approx k_b\,\Delta$, due to the very low damping properties of metal elastic elements usually employed.

The linear model formulation results in a 6^{th} order model. In the following Section, we simplify the dynamics equations, which will prove useful later in analysis and controller design.

3.1.2 Model Simplifications

In analysis of torque control performance of SEAs, it is often assumed that the dominant behaviour of the link is at significantly lower frequencies than that of the motor. Thus it is often considered fixed to simplify the analysis, reducing the model to 4^{th} order. The practical applicability of controllers designed and performance obtained in locked-output scenarios is often debated, and indeed, it has been shown that performance and even stability can significantly deteriorate in practice when the output is unlocked. We shall investigate this more in Chapter 4.

A second common assumption is that the Harmonic Drive can be considered significantly stiffer than the flexible transmission element. Therefore, a significant simplification can be obtained by considering the Harmonic Drive to be rigid, again resulting in a 4^{nd} order model. Combining the two assumptions results in a 2^{nd} order SEA model which is much simpler to analyse.

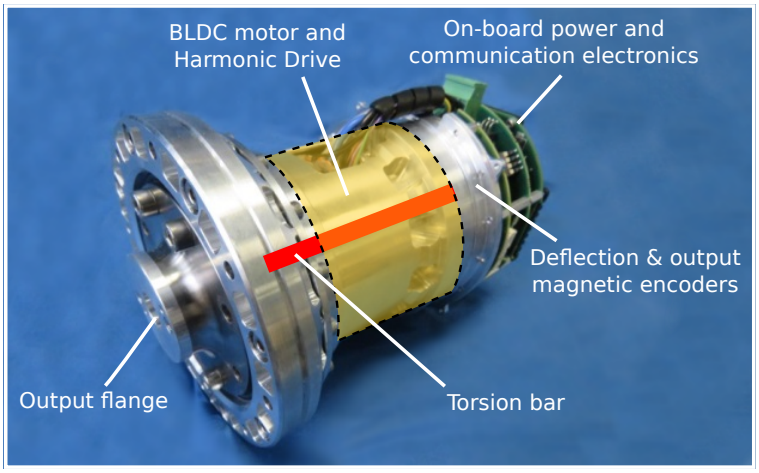

FIGURE 3.2: WALK-MAN Series-Elastic Actuator.

To assess the viability of the rigid gearbox assumption, we compare an experimental open-loop frequency sweep of a large-size WALK-MAN actuator (Fig. 3.2) in locked-output configuration with 2^{nd} and 4^{th} order fits. Fig. 3.3 shows that both fits

accurately capture the torsion bar resonance peak around 12 Hz. The fits start to differ significantly around 70 Hz, which corresponds to the expected (highly damped) resonance of the gearbox. Given the considered actuator input current limitation of 40 A, we consider this frequency to be above the control bandwidth of the actuator. However, even at frequencies lower than the gearbox resonance frequency, the phase lag associated with gearbox flexibility can result in closed-loop instability. Therefore, to ensure stability, we will use non-rigid gearbox models for simulation.

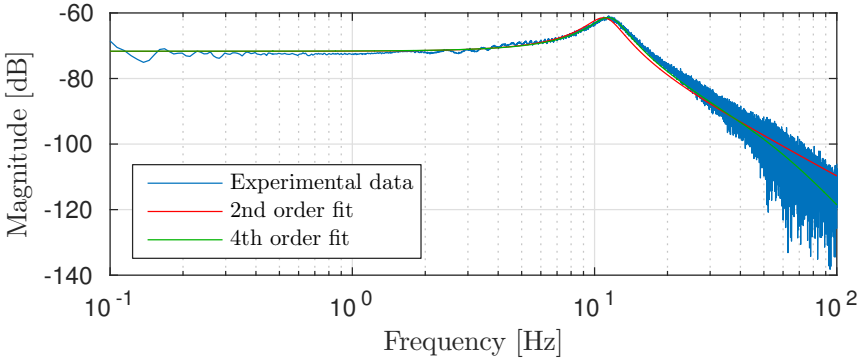

FIGURE 3.3: Open-loop sweep and 2nd and 4th order fits of a large-size WALK-MAN SEA.

Next we proceed to derive the simplified models of the full model (3.1), resulting from the aforementioned simplifications.

Locked-output

Starting with locked-output, setting $q_l \equiv \dot{q}_l \equiv \ddot{q}_l \equiv 0$, (3.1) reduces to the 4th order dynamics

$$\begin{aligned} I_m\ddot{q}_m = \tau_m \quad & -d_m\dot{q}_m \quad & +d_{mg}\left(\dot{q}_g - \dot{q}_m\right) \quad & +k_g\left(q_g - q_m\right) \\ I_g\ddot{q}_g = \quad & -d_g\dot{q}_g \quad & -d_{gl}\dot{q}_g \quad & -k_b q_g \\ & & -d_{mg}\left(\dot{q}_g - \dot{q}_m\right) \quad & -k_g\left(q_g - q_m\right), \end{aligned} \tag{3.2}$$

Rigid-gearbox

For the rigid-gearbox assumption we set $q_m \equiv q_g$, $\dot{q}_m \equiv \dot{q}_g$, and $\ddot{q}_m \equiv \ddot{q}_g$, by which (3.1) reduces to the 4th order dynamics

$$\begin{aligned} (I_m + I_g)\ \ddot{q}_g = \tau_m \quad & +k_b\,(q_l - q_g) \quad & +d_{gl}\,(\dot{q}_l - \dot{q}_g) \\ & -(d_m + d_g)\,\dot{q}_g, & (3.3) \\ I_l\ \ddot{q}_l = \tau_e \quad & -k_b\ (q_l - q_g) \quad & -d_{gl}\ (\dot{q}_l - \dot{q}_g) \\ & -d_l\,\dot{q}_l. & (3.4) \end{aligned}$$

Locked-output, rigid-gearbox

Lastly we derive the 2nd order model following from combining the locked-output and rigid-gearbox simplifications. Setting $q_l \equiv \dot{q}_l \equiv \ddot{q}_l \equiv 0$ for the fixed output, as well as $q_m \equiv q_g$, $\dot{q}_m \equiv \dot{q}_g$ for the rigid gearbox, (3.1) reduces to

$$(I_m + I_g)\,\ddot{q}_g = \tau_m + (d_m + d_g + d_{gl})\,\dot{q}_g + k_b\,q_g \tag{3.5}$$

3.1.3 Nonlinear Dynamics

Several nonlinear components were implemented to enhance the realism of the simulations and to show phenomena that do not exist in linear analysis. In the next two Sections, we describe the inclusion of asymmetric (Coulomb) friction and torque ripple dynamics, two components that have a noticeable impact on real-world behaviour of SEAs.

In practice, other sources of static and dynamic friction may exist, as well as play, hysteresis, and other nonlinearities. Furthermore, these effects may vary as a function of position and temperature. Examples are temperature dependence of friction, alignment of bearings and other components, nonlinear stiffness of compliant components, and lubrication. We shall neglect these effects in our modelling, as they

are not the dominant dynamics of an SEA and any practically feasible control algorithm should provide robust stability and performance without explicit knowledge of these phenomena.

Asymmetric (Coulomb) Friction

For mechanisms with sliding surfaces Coulomb friction is an important nonlinear damping component which becomes dominant at low velocities. The bearing damping elements d_m, d_g, d_l in Fig. 3.1 are complemented with asymmetric viscous and Coulomb friction. We allow the Coulomb friction to be asymmetric, i.e. changing in magnitude depending on sign of the velocity. To ensure the resulting functions are continuous, we employ the hyperbolic tangent function:

$$\tau_c(\dot{q}) = \begin{cases} -d_c^+ \tanh(\gamma\,\dot{q}) & \dot{q} \geq 0 \\ -d_c^- \tanh(\gamma\,\dot{q}) & \dot{q} < 0 \end{cases}, \tag{3.6}$$

where $\gamma = 500$, $\dot{q}$ denotes the velocity of the element in question, and d_c^+, d_c^- denote the positive and negative Coulomb friction magnitudes, respectively.

The friction parameters were identified from experiments on a large-size WALK-MAN actuator with amplitude modulated pseudo-random binary signals covering the entire position, velocity and acceleration range of the actuator. An example of one such identification is shown in Fig. 3.4. Due to the involvement of non-zero acceleration in these experiments, we include estimation of the inertia.

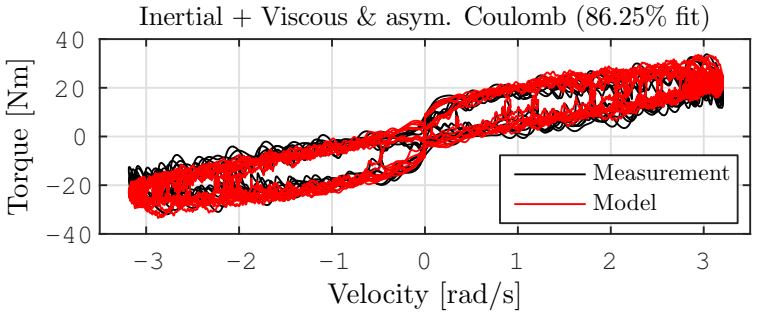

FIGURE 3.4: Experimental identification of inertia and friction parameters for a large-size WALK-MAN actuator.

Torque Ripple

There are two primary torque ripple sources present in the system that we take into account. The first is magnetic cogging (or 'detent torque'), originating from the position-dependent interaction between the Direct Current (DC) motor's permanent magnets and the stator slots, and acting as a sinusoidal torque on the motor rotor (amplitude of $15\,n$ mNm with a spatial frequency of $6\,n$ periods/rev). The second is the Harmonic Drive torque ripple, which is both position- and torque-dependent, scaling linearly with the torque transmitted through the gearbox (amplitude of $10^{-4}\,n$ Nm/Nm with a frequency of $2\,n$ periods/rev). The magnitudes for both sources are approximated from manufacturer data and measurements.

3.2 Linear Analysis & Torque Control

In this Section we analyse the torque dynamics and derive an intuitive control tuning rule for torque control of SEAs.

3.2.1 Torque Dynamics

To obtain the torque dynamics, we take the Laplace transform of (3.3) and rewrite in terms of deflection $q_g(s) - q_l(s) := \Delta(s)$:

$$\begin{aligned}\left[Is^2 + (d_M + d_{gl})\,s + k_b\right]\Delta(s) = \\ -\left[Is^2 + d_M\,s\right]q_l(s) + \tau_m(s),\end{aligned} \tag{3.7}$$

where now $I = I_m + I_g$ and $d_M = d_m + d_g$. The most common torque control scheme consists of a feedback controller of the form $C(s) = K_p + K_d\,s$ (which measures deflection and uses $\tau(s) \approx k_b\,\Delta(s)$) with feed-forward term $\lambda(s)$:

$$\tau_m(s) = C(s)\left[\tau^*(s) - k_b\,\Delta(s)\right] + \lambda(s)\,\tau^*(s), \tag{3.8}$$

where $\tau^*(s)$ denotes the desired torque in the Laplace domain. Substituting into (3.7), we obtain

$$\begin{aligned}\left[Is^2 + (d_M + d_{gl})\, s + k_b\,(1 + C(s))\right]\Delta(s) = \\ -\left[Is^2 + d_M\, s\right] q_l(s) + \left[C(s) + \lambda(s)\right]\tau^*(s),\end{aligned} \tag{3.9}$$

Considering that $\tau(s) = (k_b + d_{gl}\, s)\,\Delta(s)$, (3.9) can be solved for $\tau(s)$ as the sum of input responses from $\tau^*(s)$ and $q_l(s)$:

$$\tau(s) = (k_b + d_{gl}\, s)\left[\Delta_{\tau^*}(s)\,\tau^*(s) + \Delta_{q_l}(s)\, q_l(s)\right], \tag{3.10}$$

where

$$\begin{aligned}\Delta_{\tau^*}(s) &= \frac{\Delta(s)}{\tau^*(s)} = \frac{K_d\, s + K_p + \lambda(s)}{I\, s^2 + D_\Delta\, s + K_\Delta}, \\ \Delta_{q_l}(s) &= \frac{\Delta(s)}{q_l(s)} = \frac{-\left(Is^2 + d_M\, s\right)}{I\, s^2 + D_\Delta\, s + K_\Delta},\end{aligned} \tag{3.11}$$

and

$$\begin{aligned}D_\Delta &= k_b\, K_d + d_M + d_{gl}, \\ K_\Delta &= k_b\,(K_p + 1).\end{aligned} \tag{3.12}$$

To convince oneself the dichotomy described by (3.10) is valid, consider that by setting $q_l(s) \equiv 0$, the torque dynamics simplify to those of the fixed-output, rigid-gearbox system of (3.5) in the Laplace domain. Conversely, choosing $q_l(s)$ as the load admittance described by (3.4), one obtains the complete rigid-gearbox model described by (3.3) and (3.4), with inputs $\tau^*(s)$ and $\tau_e(s)$. This is depicted graphically in Fig. 3.5.

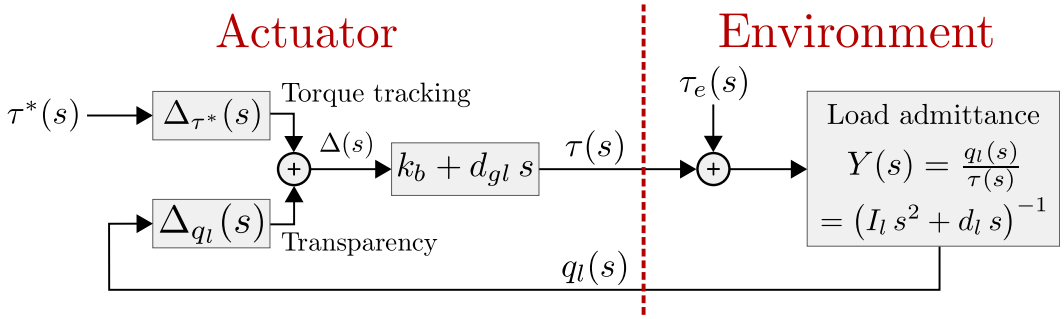

FIGURE 3.5: Torque Dynamics of an SEA driving a load admittance.

The load admittances $Y(s)$ and $Y_e(s)$ (for the environmental interaction force) are derived by rewriting (3.4):

$$\begin{aligned} I_l\, \ddot{q}_l &= \tau_e - k_b\, (q_l - q_g) - d_{gl}\, (\dot{q}_l - \dot{q}_g) - d_l\, \dot{q}_l \\ &= \tau_e + \tau - d_l\, \dot{q}_l \\ I_l\, \ddot{q}_l + d_l\, \dot{q}_l &= \tau_e + \tau \end{aligned} \tag{3.13}$$

and performing the Laplace transform:

$$\begin{aligned} q_l(s) &= \left(I_l\, s^2 + d_l\, s\right)^{-1} (\tau(s) + \tau_e(s)) \\ \implies Y(s) &= Y_e(s) = \left(I_l\, s^2 + d_l\, s\right)^{-1} \end{aligned} \tag{3.14}$$

Given that $Y(s) = Y_e(s)$, $\tau(s)$ and $\tau_e(s)$ may simply be summed to obtain Fig. 3.5. Furthermore, note that in the dotted boundary between actuator and environment in Fig. 3.5 defines the exchange of mechanical power P between the actuator and its environment, which can be defined as $P = \dot{q}_l\, \tau$.

However, instead of choosing a predefined admittance, (3.10) is more general, and useful for obtaining the robust torque control performance in the presence of arbitrary output motion from an unknown environment, as well as assessing actuator transparency as seen from the environment. In Chapter 4 we shall further investigate this dichotomy, in the form of the two boundary cases of (3.10). First, we discuss the procedure for pole placement that governs both.

3.2.2 Torque Control: Pole Placement Procedure

Inspecting (3.9)–(3.11), we observe that $\Delta_{\tau^*}(s)$ and $\Delta_{q_l}(s)$ have equal denominators. Consequently, an appropriate choice of $C(s)$ allows us to arbitrarily place the closed-loop poles for both, by selection of K_p, K_d. Using the characteristic polynomial of a general 2nd order system:

$$s^2 + 2\,\zeta\,\omega_0\,s + \omega_0^2 = 0, \tag{3.15}$$

where ω_0 is the characteristic frequency and ζ is the damping ratio, allows us to place the poles of the closed-loop system in desired locations. Writing the denominators of (3.11) in the form of (3.15) and solving for K_d, we obtain the controller derivative gain as a function of the closed-loop damping ratio ζ and proportional gain K_p:

$$K_d = \frac{2\,I\,\omega_0\,\zeta - (d_M + d_{gl})}{k_b}, \tag{3.16}$$

where

$$\omega_0 = \sqrt{K_\Delta / I} = \sqrt{k_b\,(K_p + 1)\,/\,I}. \tag{3.17}$$

Using (3.16) and choosing $\zeta = 1$, the gain selection is simplified to selection of only the proportional gain K_p, which is now equivalent to selection of the pole frequency ω_0 (solving (3.17) for K_p):

$$K_p = \frac{\omega_0^2\,I}{k_b} - 1 = \frac{\omega_0^2}{\omega_n^2} - 1, \tag{3.18}$$

where the natural frequency $\omega_n = \sqrt{k_b/I}$ is given by the zeroes of the denominators in (3.11)[1]. Choosing the closed-loop poles, that define the control bandwidth, as a constant times the system's natural frequency:

$$\omega_0 = \alpha\,\omega_n, \tag{3.19}$$

[1]Note that if one "closes the loop" using the load admittance as in Fig. 3.5, the effective natural frequency is equal to $\omega_n = \sqrt{\frac{k_b(I+I_l)}{I\,I_l}}$. Although this converges to $\sqrt{k_b/I}$ for $I_l \gg I$, one can easily see that for small load inertia the performance may quickly deteriorate due to torque arising from significant load motion $q_l(s)$ in (3.10). The factors that influence this will be investigated in Chapter 4.

results in a simple tuning rule with α as the only parameter, which is independent of stiffness: $K_p = \alpha^2 - 1$. Note that a positive control gain $K_p > 0$ requires the closed-loop pole frequency to be at least as high as the natural plant frequency: $\omega_0 > \omega_n$. Or equivalently, $\alpha > 1.0$. Similarly, we constrain $K_d \geq 0$, as small values of the stiffness k_b may result in plants that are naturally overdamped. Lastly, from the two-input system described by (3.10)–(3.12), one can observe that the feed-forward gain $\lambda(s)$ affects $\Delta_{\tau^*}(s)$, while $\Delta_{q_l}(s)$ is independent of $\lambda(s)$. Hence, we proceed the analysis with $\lambda(s) \equiv 1$, resulting in zero steady-state error for $\Delta_{\tau^*}(s)$.

3.3 Compliant Joint Toolbox (CJT)

As part of the work presented in this thesis, the Compliant Joint Toolbox (CJT) [42] was developed, a MATLAB/Simulink toolbox for SEAs. The goal is to provide rapid iteration of different models and architectures by providing a number of pre-built components with consistent interfaces, together with a set of tools to build new ones. For example, it allows to rapidly generate joint models, prototype controllers and observers, perform simulation, and apply the developed control systems directly to the real hardware using Simulink Real-Time. This Section provides a brief overview of the toolbox and its capabilities. The toolbox is available on GitHub at https://github.com/geez0x1/CompliantJointToolbox.

A global overview of the toolbox is shown in Fig. 3.6. It mainly consists of a number of classes, together with helper functions. Using the `jointBuilder` class, custom joint classes can be constructed. The joint builder utilises the well-known factory design pattern. This means it builds (almost) self-contained joint classes with the requested parameters, models, and nonlinear components (shown in Fig. 3.6 as the `jointModel` class). Ingredients to create new joint classes from the user perspective are actuator parameters, selected linear dynamics model (Sec. 3.1.1), and the nonlinear components the user wishes to include (Sec. 3.1.3).

The library provides a number of pre-built controllers and observers, as well as building blocks to create new components, which can be used in simulation to design the control system. After simulation, these can then be applied without changes

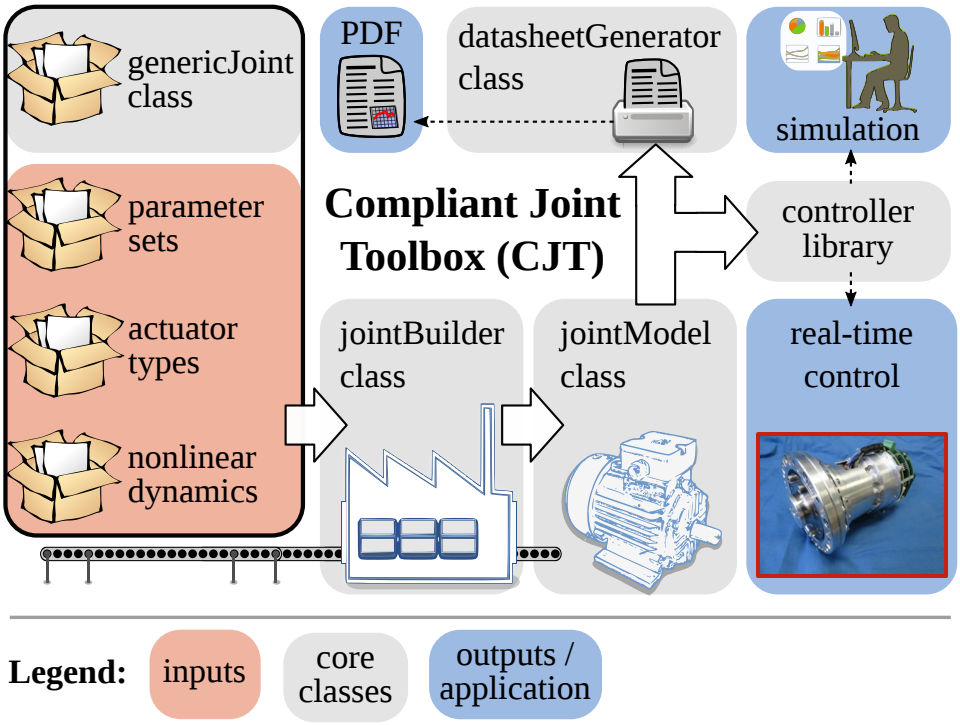

FIGURE 3.6: Overview of the Compliant Joint Toolbox for MATLAB/Simulink. Figure courtesy of Dr. Jörn Malzahn.

to the physical hardware, using Simulink Real-Time. Furthermore, one can generate PDF datasheets for joints using the `datasheetGenerator` class.

The basic Simulink joint models themselves are shown in Fig. 3.7. Linear actuator dynamics are formulated as state-space models, with state-space matrices A, B, C, D. Nonlinear dynamics components are contained in $\mathbf{g}$. Gaussian input and output noise are denoted by η_i and $\boldsymbol{\eta}_o$, respectively, and input/output delay can be added as desired. Measurements are quantised, denoted by $\boldsymbol{\epsilon}_o$ in Fig. 3.7.

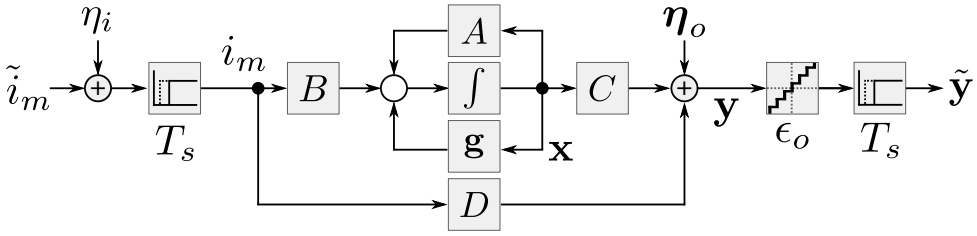

FIGURE 3.7: Compliant Joint Toolbox `jointModel` structure.

The measurement principles and controllers are implemented similar to their hardware counterparts (which run on Digital Signal Processors (DSPs));

- Discrete-time with 2 kHz sample rate;

- One timestep of input and output delay;
- Derivative filtering (200 Hz);
- Gaussian current and sensor noise with variances 14 mA and 1.8e-10 rad, respectively;
- Encoder quantisation (19 bits);
- Current limitation (40 A).

4

Stiffness Selection of SEAs

Series-elastic actuators are quickly becoming the core component of robots operating in real world environments, allowing for robust, safe, torque controlled robots. This Chapter investigates the influence of the selected stiffness and control parameters. By consolidating several analyses, it is shown two opposing criteria exist for the choice of stiffness: lowering stiffness increases actuator transparency, while increasing stiffness increases torque tracking bandwidth. This fact is used in the context of impedance rendering to propose an optimal stiffness selection criterion that maximises the renderable impedance frequency. This provides a concrete method for choosing stiffness based on the application of the joint. Extensive simulation and experimental results are presented that validate the analyses.

This Chapter is organised as follows. Sec. 4.1 analyses the dichotomy of SEA dynamics presented in Chapter 3. A stiffness selection guideline for impedance rendering is proposed in Sec. 4.2, followed by simulations and experimental results in Sec. 4.3

and 4.4. Concluding remarks are reported in Sec. 4.5.

4.1 Transparency and Torque Tracking

In this Section we further investigate the SEA dynamics presented in Chapter 3, in the form of the two boundary cases of (3.10):

1. $\tau^*(s) \equiv 0$ (the actuator should be transparent, or its output impedance ideally zero);
2. $q_l(s) \equiv 0$ (the load is fixed or sufficiently large).

A similar analysis was performed in [21], however we report some additional insights with regards to the transfer functions zeroes.

4.1.1 Transparency: Load Motion to Residual Torque

The transparency of an actuator in this context is defined as the ability to track zero torque in the presence of output motion (i.e. backdriving the actuator); transparency is the inverse of the residual torques given an imposed output motion.

Setting $\tau^*(s) \equiv 0$ in (3.10) and solving for $\frac{\tau(s)}{q_l(s)}$, we obtain

$$\frac{\tau(s)}{q_l(s)} = \frac{-\left(k_b + d_{gl}\, s\right)\left(I s^2 + d_M\, s\right)}{I\, s^2 + D_\Delta\, s + K_\Delta}. \tag{4.1}$$

We hereafter refer to (4.1) as the *transparency function* of the actuator. Using $s = j\omega$ with $j = \sqrt{-1}$, we find the high frequency gain of (4.1) is given by $-(k_b + d_{gl}\, s)$, i.e. the passive impedance of the flexible element. Hence, the high frequency transparency is upper bounded by the flexible element stiffness, since it is reasonable to assume d_{gl} to be a function of k_b due to the mechanical implementation. However, since for $\omega \to 0$ we have (4.1) $\to 0$ (applying the final value theorem), we find that in principle the actuator can be made arbitrarily transparent at a given frequency by placing the poles at an arbitrarily high frequency.

The transparency function shows that the transparency of the actuator is determined by 1) the frequency ω_0 of the closed-loop poles and 2) the stiffness k_b. Fig. 4.1 shows the effect of varying both these parameters.

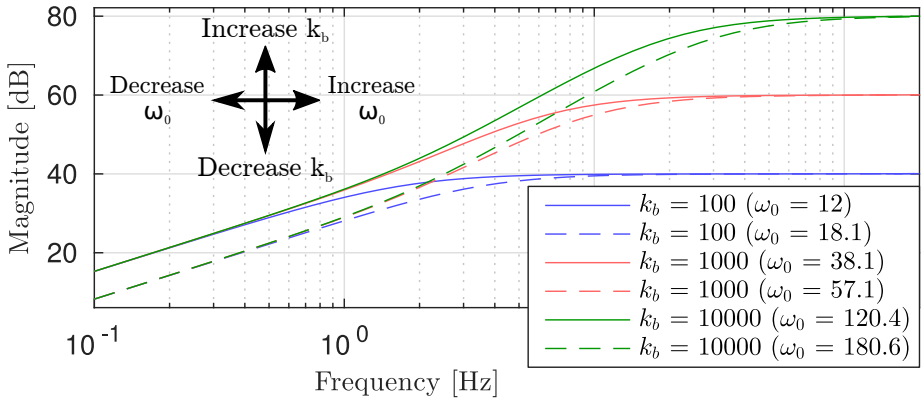

FIGURE 4.1: Varying k_b and ω_0 in (4.1): Residual torque from load motion for various stiffness values and closed-loop poles. Here we have chosen α =1.2 and 1.8 for each stiffness value.

At low frequency the transparency depends only on α (i.e. control gain), whereas at high frequency it depends only on k_b, with a transition period in between. At high frequencies each actuator converges to a gain of k_b, with lower stiffness actuators showing lower residual torques, i.e. higher transparency. Furthermore, Fig. 4.1 shows that increased control bandwidth improves the transparency; however, such an increase for stiffer actuators only results in surpassing the transparency of lower stiffness actuators up to a limited frequency, as the transparency of stiffer actuators intrinsically deteriorates at higher frequencies due to the upper bound defined by increased stiffness. High frequency transparency is however important in impacts due to their impulsive nature; high stiffness SEAs may provide insufficient protection against impacts, despite high control bandwidth.

Consider two actuators with different stiffness values $k_{b,1}$ and $k_{b,2}$, with the closed-loop pole frequency of the first actuator given by ω_1. By calculating the intersection between the extrapolation of the +40 dB/dec slope of the first actuator and the stiffness of the second actuator in dB, the pole frequency ω_2 required for the second actuator to obtain the same transparency (up to ω_1) can be derived:

$$\omega_2 = \exp\left[\frac{1}{2}\ln\left(\frac{k_{b,2}}{k_{b,1}}\right) + \ln(\omega_1)\right] = \sqrt{\frac{k_{b,2}}{k_{b,1}}}\,\omega_1, \tag{4.2}$$

which, by substituting $\omega_1 = \alpha_1 \sqrt{\frac{k_{b,1}}{I}}$ and $\omega_2 = \alpha_2 \sqrt{\frac{k_{b,2}}{I}}$, gives $\alpha_1 = \alpha_2$, confirming the equal low frequency transparency for constant values of α in Fig. 4.1. In other words, choosing α enables us to choose the low frequency transparency independently of stiffness.

Inspecting the numerator of (4.1), the first zero (other than $s = 0$) is located at $s = -d_M/I$, which corresponds to the intuition that lowering the motor-side damping increases the transparency. Apart from clever mechanical design to minimise friction, active solutions have been proposed, such as friction compensators, and more recently, disturbance observers [11], [13]. The presence of s in each term reveals the velocity dependence, and in fact feeding back the link velocity signal can effectively remove the zero at $s = -d_M/I$ in velocity sourced actuators [34]. Hereafter the zero at $s = -k_b/d_{gl}$ will be disregarded, since due to $k_b \gg d_{gl}$ it falls outside the frequency range of interest.

4.1.2 Torque Tracking

Setting $q_l(s) \equiv 0$ in (3.10) and solving for $\frac{\tau(s)}{\tau^*(s)}$, we obtain

$$\frac{\tau(s)}{\tau^*(s)} = \frac{(k_b + d_{gl}\, s)\,(K_d\, s + K_p + 1)}{I\, s^2 + D_\Delta\, s + K_\Delta}. \tag{4.3}$$

We hereafter refer to (4.3) as the *torque tracking function* of the actuator. Eq. (4.3) has a denominator identical to that of (4.1) which allows for pole placement as presented in Sec. 3.2.2, however in (4.3) the control gains also affect the closed-loop zeroes. Fig. 4.2 shows the effect of varying both k_b and ω_0 in (4.3). The low frequency zero in (4.3) is given by

$$s = -\frac{K_p + 1}{K_d} = -\frac{I\,\omega_0^2}{2\,I\,\omega_0\,\zeta - (d_M + d_{gl})}. \tag{4.4}$$

For $\omega_0 > 0$, this zero quickly converges to $\approx \omega_0/(2\,\zeta)$; as the chosen pole frequency increases, the distance between this zero and the poles increases, which may result in a ripple in the torque response despite critical damping of the poles.

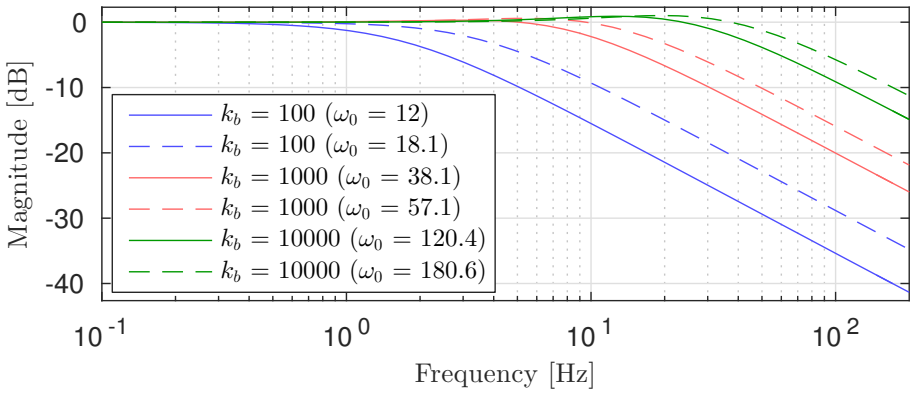

FIGURE 4.2: Varying k_b and ω_0 in (4.3): Torque tracking. Here we have chosen α = 1.2 and 1.8 for each stiffness value.

4.1.3 Motor Power

An oft-cited disadvantage of SEAs with lower stiffness is higher power consumption due to the larger motor movements required to achieve the deflection needed for a certain desired torque. To investigate this, we use (3.7) in the same boundary case as Sec. 4.1.2 with $\tau(s) = (k_b + d_{gl}\, s)\, \Delta(s)$:

$$\left.\frac{\tau_m(s)}{\tau(s)}\right|_{q_l(s)\equiv 0} = \frac{Is^2 + (d_M + d_{gl})\, s + k_b}{k_b + d_{gl}\, s}, \tag{4.5}$$

which can be observed (Fig. 4.3) to increase with +40 dB/dec after the mechanical resonance now present in the numerator. Due to input torque limitation arising from maximum allowable current, further exasperated by a reduction in torque resulting from the back-EMF component and operating voltage, achievable motor power is limited. Thus, the mechanical resonance frequency is an inherent source of torque tracking bandwidth limitation, regardless of control strategy [21]. In the other boundary case (transparency, Sec. 4.1.1), the deflection is ideally zero and the required motor torque difference between actuators of different stiffness values disappears, i.e. becomes independent of k_b. This is shown by solving (3.7) for $\frac{\tau_m(s)}{q_l(s)}$ while setting $\Delta(s) \equiv 0$:

$$\left.\frac{\tau_m(s)}{q_l(s)}\right|_{\Delta(s)\equiv 0} = Is^2 + d_M\, s, \tag{4.6}$$

which depends only on I and d_M. In conclusion, the motor torque for a lower stiffness SEA is much higher while tracking torque profiles above the mechanical resonance. However, this is not the case for lower frequencies or interaction with small torques, which require approximately identical power regardless of stiffness.

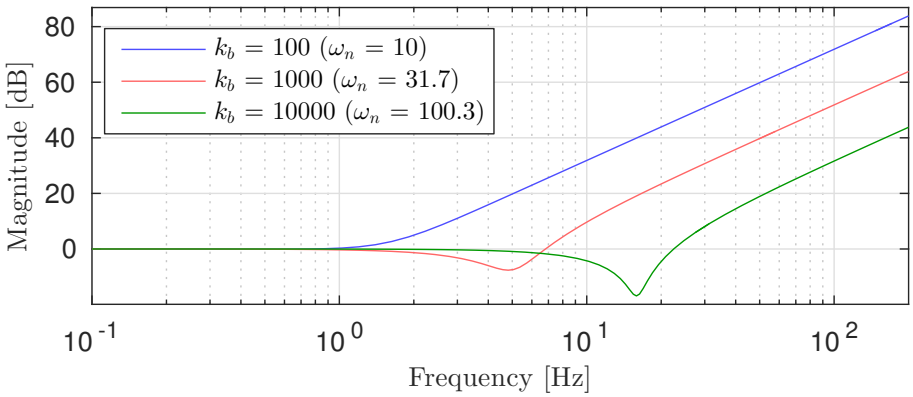

FIGURE 4.3: Motor torque as function of delivered output torque.

4.2 Optimal Stiffness Selection for Impedance Rendering

4.2.1 Impedance Rendering and Motion Control

In many real-world applications the torque control loop is supplemented by an outer loop to provide motion control and impedance rendering to the robotic system. The desired torque is commonly given by a 1st order impedance:

$$\tau^* = K\left(q_l^0 - q_l\right) + D\left(\dot{q}_l^0 - \dot{q}_l\right), \tag{4.7}$$

where $q_l^0, \dot{q}_l^0$ denote the reference position of the link and its derivative, and K, D denote stiffness in Nm/rad and damping in Nms/rad, respectively. Given a stable torque control loop and $K_d \geq 0$, both the zeroes and the poles of the inner loop will be in the left-hand complex plane, and as such for $K, D \geq 0$ the entire closed-loop system will be asymptotically stable. However, it is well known that in practical systems with nonlinear effects like friction, discrete-time control, delays, filtering, noise and quantisation, increasing the gains of the inner (torque) loop can have a detrimental effect on the stability of the overall system, despite the inner loops themselves being stable. This results in a limitation on the achievable closed-loop pole

frequency (Sec. 3.2.2), and therefore stiffness selection requires careful consideration. For an elaborate discussion and experimental results, see e.g. Focchi et al. [36]. To investigate impedance rendering, we set $q_l^0 \equiv \dot{q}_l^0 \equiv 0$ in (4.7) and transform into the Laplace domain:

$$\tau^*(s) = -\left(K + D\,s\right)\, q_l(s). \tag{4.8}$$

Substituting (4.8) into (3.10) and solving for the rendered impedance $Z(s)$, we obtain:

$$\begin{aligned} Z(s) &= \frac{\tau(s)}{q_l(s)} \\ &= \left(k_b + d_{gl}\,s\right)\left[-\left(K + D\,s\right)\Delta_{\tau^*}(s) + \Delta_{q_l}(s)\right] q_l(s) \\ &= -\left(k_b + d_{gl}\,s\right)\frac{a\,s^2 + b\,s + c}{I\,s^2 + d\,s + e}, \end{aligned} \tag{4.9}$$

with

$$\begin{aligned} a &= I + K_d\,D, & d &= k_b\,K_d + d_M + d_{gl}, \\ b &= D\,(K_p + 1) + K_d\,K + d_M, & e &= k_b\,(K_p + 1), \\ c &= K\,(K_p + 1), \end{aligned} \tag{4.10}$$

which is functionally equal to Fig. 4.4. Contrary to pure torque tracking where the objective is tracking torque independent of the load motion, the objective here is accurate rendering of desired output impedance $Z(s) = \frac{\tau(s)}{q_l(s)}$; perfect rendering would imply $Z(s) = -K - D\,s$.

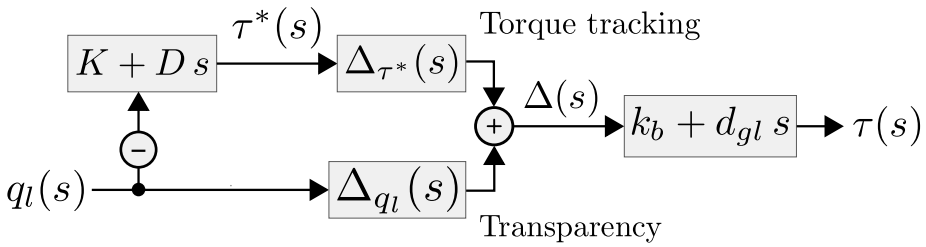

FIGURE 4.4: Impedance rendering block diagram.

The structure of (4.9) suggests both the torque tracking bandwidth and transparency function can limit the impedance rendering capability of an actuator. We demonstrate this with an example of two actuators with stiffness values of 10000 and 100 Nm/rad respectively, both rendering a reference impedance of K = 1000 Nm/rad and D =

20 Nms/rad. The former case is shown in Fig. 4.5, which displays a plot of the rendered impedance (4.9), a reference impedance $K + D\,s$, the transparency function (4.1), and the torque tracking function (4.3). Fig. 4.5 reveals that the actuator transparency is a limiting factor; the minimum renderable impedance is dictated by the transparency function.

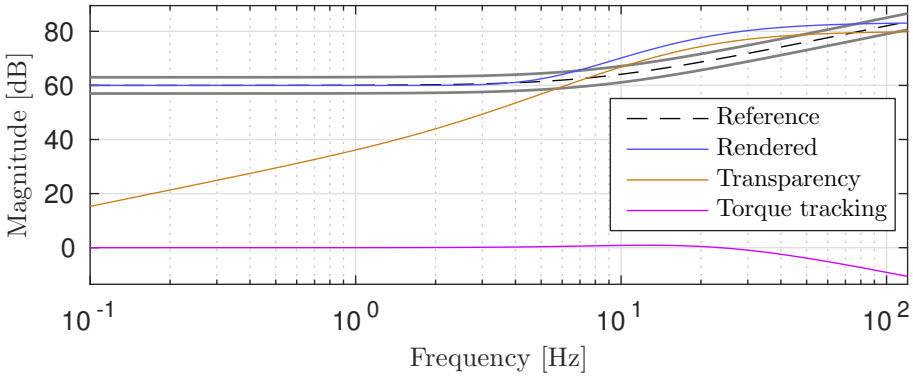

FIGURE 4.5: Impedance rendering for k_b = 10000 Nm/rad, limited by the transparency function. Here K = 1000 and D = 20.

Conversely, Fig. 4.6 shows the same reference impedance rendered by the lower stiffness actuator. In this case, the substantially reduced torque tracking bandwidth is the limiting factor to the impedance rendering bandwidth. In both figures, the solid grey lines denote the ± 3 dB margin.

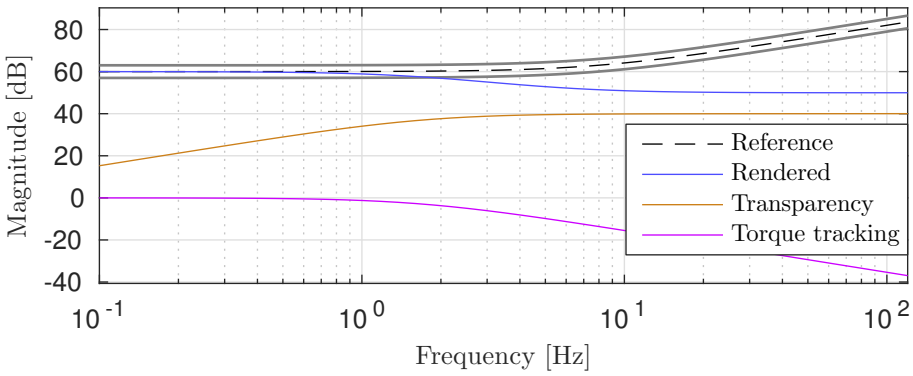

FIGURE 4.6: Impedance rendering for $k_b = 100$ Nm/rad, limited by the torque tracking bandwidth. Here K = 1000 and D = 20.

Setting $K, D = 0$ in (4.9) immediately reveals similarity to (4.1). It can also be seen that for small K, D, (4.9) tends to (4.1) at high frequencies, with an increase of gain resulting from $K_d\,D$ in a of (4.9).

4.2.2 Optimal Stiffness Selection

Following the presented analyses, we can suggest an optimal stiffness selection guideline for SEAs. Choice of rotor, its inertia, torque constant and gear ratio are largely determined by the application torque and speed requirements, and since their choice is the same as for stiff motors, we will not discuss them here. Sec. 4.1 showed that two opposing criteria exist for the choice of stiffness: Lowering k_b increases transparency, and increasing k_b increases torque tracking bandwidth. Using the context of impedance rendering, we can frame these two criteria into a single metric that can be optimised on, as will be demonstrated in the following.

For a robotic system under motion control, three operating parameters can be defined:

1. the minimum/maximum load inertia I_l^{min}, I_l^{max} that will be seen by the actuator, and
2. the motion bandwidth requirement ω_m of the robot.

These parameters define the range of impedance values that have to be replicated by the actuator. Given a frictionless joint with load I_l, the joint impedance that places the poles at a frequency ω_m is given by $Z_{ref}(s) = K + D\,s$, with

$$K = \omega_m^2\, I_l, \qquad D = 2\, I_l\, \omega_m\, \zeta, \tag{4.11}$$

where we set $\zeta = 1$. Both K and D are linear in I_l, so that the required minimally renderable impedance $Z_{min}(s)$ of the actuator is given by (4.11) with $I_l = I_l^{min}$.

By defining a margin of acceptable accuracy ϵ, we can optimise for the maximum frequency ω_b up to which a reference impedance $Z_{ref}(s)$ can be rendered accurately:

$$\max_{k_b}\ \omega_b \quad \text{s.t.} \quad \frac{|Z(j\omega)|}{|Z_{ref}(j\omega)|} \in [-\epsilon, +\epsilon]\ \ \forall\ \ \omega \leq \omega_b, \tag{4.12}$$

where $j = \sqrt{-1}$. Given I_l^{min}, I_l^{max} and ω_m, for the motion requirements to be fulfilled we require

$$\omega_b \geq \omega_m\ \ \forall\ \ I_l \in \left[I_l^{min}, I_l^{max}\right], \tag{4.13}$$

i.e. the impedance can be rendered accurately up to at least the motion bandwidth, for the entire link inertia range.

The optimisation (4.12) and impedance replication requirement (4.13) provide a concrete method for choosing k_b based on the application of the joint. Fig. 4.7 shows an example of the application of (4.12) for a reference impedance of $K = 1000\,\mathrm{Nm/rad}$ and $D = 20\,\mathrm{Nms/rad}$, resulting in an optimal stiffness of $k_b = 752\,\mathrm{Nm/rad}$ and a rendering bandwidth of $\approx 12\,\mathrm{Hz}$. Here $\alpha = 1.2$ and $\epsilon = 3\,\mathrm{dB}$ were chosen. One important thing to note is that if passivity is desired (while rendering pure stiffness, i.e. $D = 0$), the mechanical stiffness should be chosen higher than the rendered stiffness [22], [23].

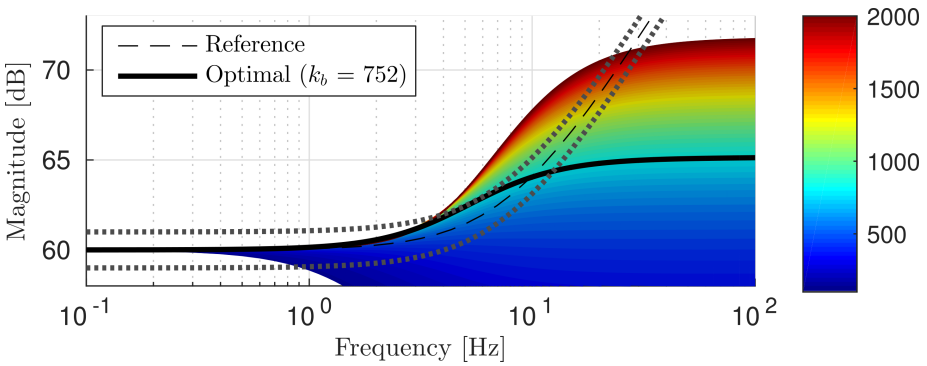

FIGURE 4.7: Impedance rendering optimisation for a reference impedance of $K = 1000$ and $D = 20$. The dotted grey lines show the $\epsilon = \pm 3$ dB acceptable accuracy margin.

Note that the tradeoff between transparency and torque tracking bandwidth extends beyond impedance rendering: most modern full-body and inverse-dynamics based control methods assume actuators to be pure torque sources, unaffected by joint motion, while this assumption does not hold.

4.3 Simulation Results

To validate the analyses presented in Sec. 4.1 and 4.2, this Section provides simulation results on the full model shown in Fig. 3.1, supplemented with nonlinear components, outlined in the next Section. The actuators considered in the simulations and experiments are WALK-MAN high-power actuators [1], [2], capable of torques of 300+ Nm. Besides the stiffness values used before, we add two actuators

with stiffness values of 2700 Nm/rad (B12) and 11400 Nm/rad (B14), which will also be evaluated in experiment.

We first consider the actuators to be in locked-output configuration to investigate their ability to track desired torques without the influence of a moving load. Then, in Sec. 4.3.2 and 4.3.3, we use the same controllers and assess the transparent interaction and impedance rendering performance, respectively.

4.3.1 Torque Tracking in Locked-Output Configuration

Fig. 4.8 shows the closed-loop torque tracking response. As expected, the higher stiffness actuators are able to achieve much higher bandwidth. The controller gains were derived with $\alpha = 2.70, 1.90, 1.50, 1.12, 1.10$ for the 100, 1000, 2700, 10000, 11400 Nm/rad actuators, respectively. Despite using α being a very useful way of choosing gains, selecting a single value of α for very different stiffness values proved impractical due to the involvement of nonlinear dynamics, finite gearbox stiffness, and input saturation. The gains were chosen s.t. input saturation would not occur before -3 dB and no more than +1 dB ripple was observed.

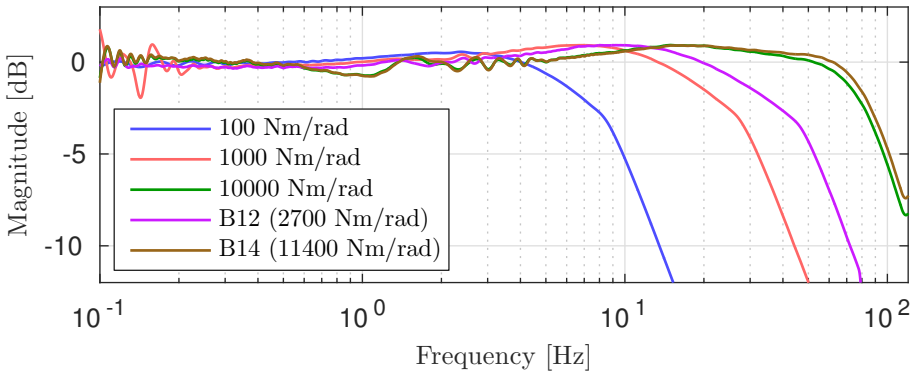

FIGURE 4.8: Simulation: Fixed-output torque tracking.

While the higher stiffness values 10000 and 11400 Nm/rad did not saturate the 40 A input, they see a similar roll-off starting around 60 Hz due to the modelled finite gearbox stiffness. It can be observed that a set of ripples appear at low frequencies. While partly numerical artifacts, they are indeed the result of the nonlinearities outlined in Sec. 3.1.3, and become dominant at lower frequencies and amplitudes.

4.3.2 Transparency

We simulate the actuator's transparency by frequency sweeping the output position. As frequency increases, the amplitude is reduced to keep the velocity amplitude constant, to avoid quickly reaching excessive velocities.

Fig. 4.9 displays the residual torques. As expected based on Sec. 4.1.1, the lower stiffness actuators demonstrate much lower residual torques over the entire frequency range, despite the much lower torque tracking bandwidth. The higher gains for the lower stiffness actuators results in lower residual torques at low frequencies. Furthermore, the residual torques can be seen to converge to k_b (in dB) at high frequencies.

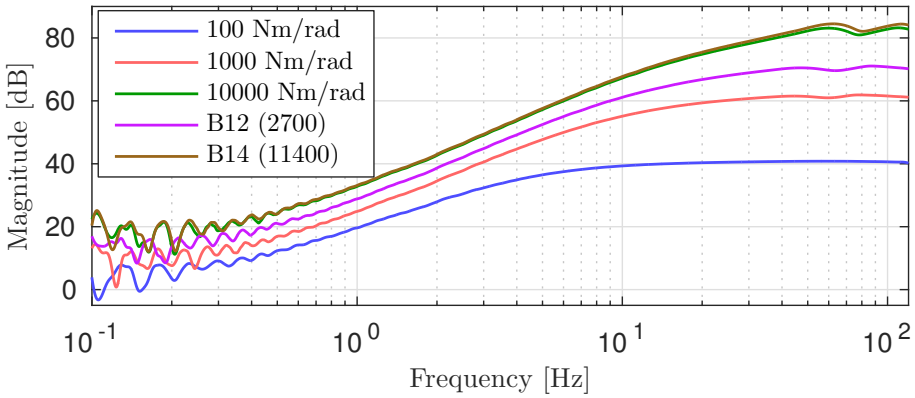

FIGURE 4.9: Transparency ($\tau^* \equiv 0$): Simulated residual torques due to output motion.

4.3.3 Impedance Rendering

We simulate the impedance rendering capability of all five stiffness levels, for a reference impedance of $K = 1000\,\mathrm{Nm/rad}$ and $D = 20\,\mathrm{Nms/rad}$. The results shown in Fig. 4.10 confirm the validity of the theoretical predictions in Sec. 4.2; see e.g. Fig. 4.7. Additional roll-off can be seen at high frequencies, which was confirmed to be attributed to the finite gearbox stiffness.

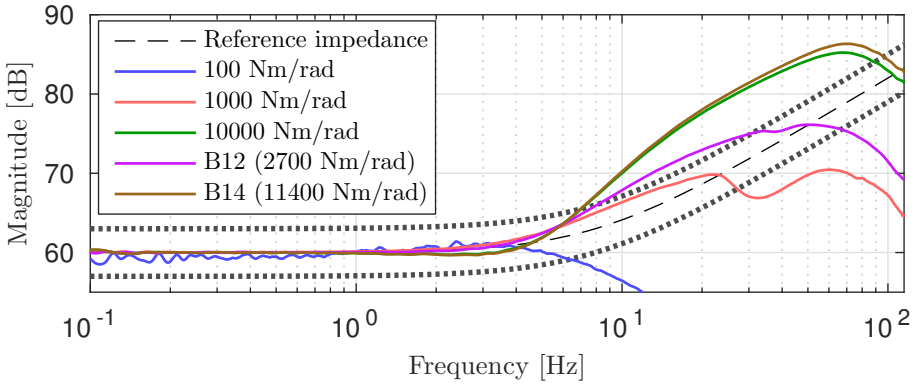

FIGURE 4.10: Simulation: Impedance rendering for a reference impedance of $K = 1000$ and $D = 20$. The dotted grey lines show the $\epsilon = \pm 3$ dB acceptable accuracy margin.

4.4 Experimental Results

4.4.1 Experimental Setup

To investigate the influence of actuator stiffness in practice, the previously mentioned actuators B12 and B14 were used. The controllers received torque references through a 1 kHz real-time EtherCAT connection. As in simulation, the torque controller itself was running on DSPs at 2 kHz, and other controller properties were equally unchanged. We include simulated results in the transparency and impedance rendering experiments for comparison.

4.4.2 Torque Tracking in Locked-Output Configuration

The actuators were first tested in locked-output configuration, by fixing the output flange to ground. A torque reference frequency sweep was performed, the results of which are shown in Fig. 4.11. We found the bandwidth of both actuators to increase slower than expected with increased α. However, we used $\alpha = 2.3$ and 3.3 for both actuators in further experiments: the higher gain results in improved low-frequency accuracy (Sec. 4.1.1). Equal values of α for both actuators ensures a fair comparison. The bandwidth for both actuators is lower than expected; while for B12 the natural frequency appears to lie in roughly the expected location based on α, both actuators

experience more roll-off than suggested by the simulations. We suspect this is due to nonlinear stiffness and lost motion of the gearboxes.

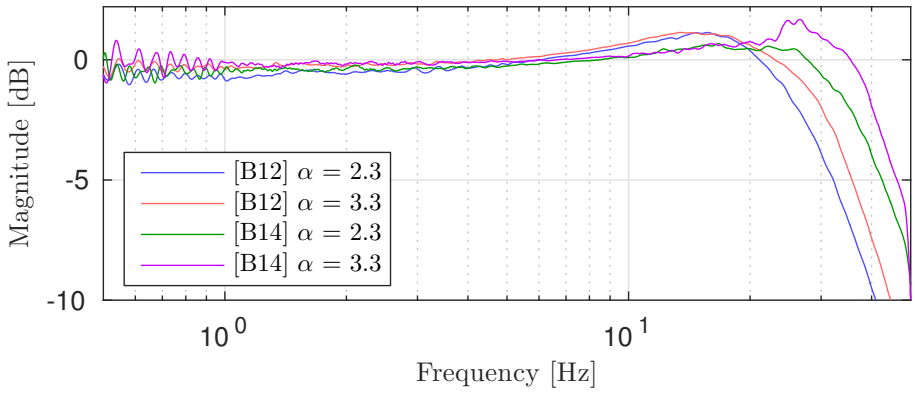

FIGURE 4.11: Experiment: Fixed-output torque tracking.

4.4.3 Transparency

To evaluate the actuator transparency, pendulum drop experiments were performed with a 35 cm, 4.5 kg pendulum with an inertia of 0.35 kg m^2, released from a horizontal position. The results are shown in Fig. 4.12. As expected, transparency increases with increased gains. However, it can be observed the more compliant B12 offers more transparency than B14 at both gain levels, resulting in a more natural, less damped pendulum swing. This is most likely due to larger friction in B14. Conversely, given that the friction parameters were identified on B12, its simulated and experimental responses are in good agreement. The spike in torque for B12 at 0.45 s is due to reaching the speed limit of ≈ 5 rad/s imposed by the back-EMF and the operating voltage of 24 V.

4.4.4 Impedance Rendering

To investigate the impedance replication capability, we set the reference impedance to a pure spring with $K = 100$ Nm/rad and $D = 0$ Nms/rad. The pendulum was moved from a hanging position by 20° and released. As shown in Fig. 4.13, similar to the pendulum drop findings, the lower stiffness actuator shows larger capability of handling the load motion, resulting in a lesser damped response. While this can in part be explained by differences in friction, the difference was observed to increase at

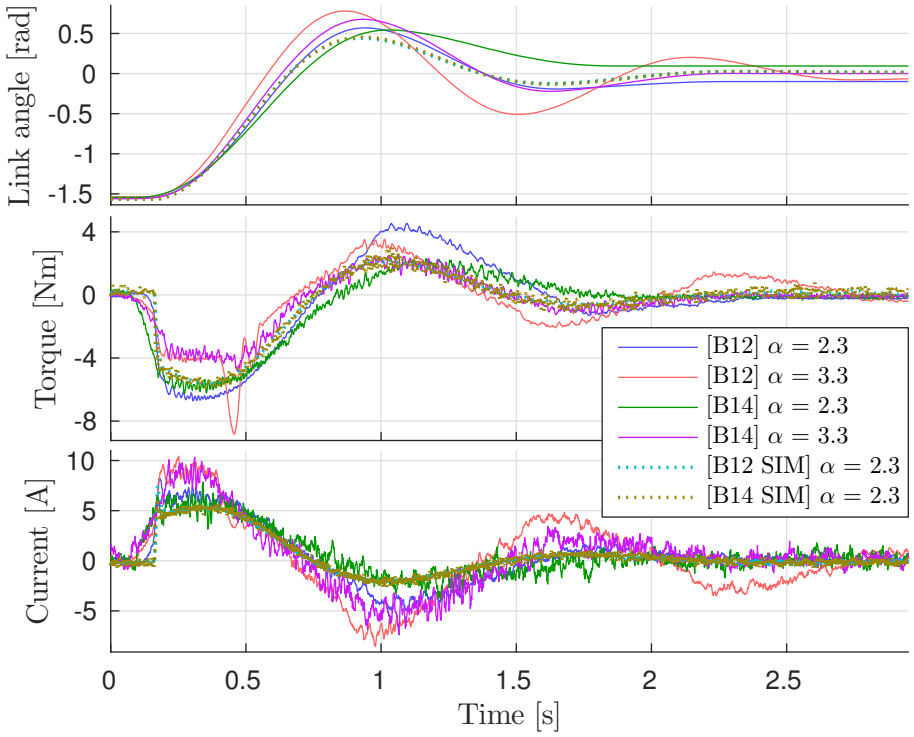

FIGURE 4.12: Transparency ($\tau^* \equiv 0$) experiment: Dropping a 4.5 kg, 0.35 kg m^2 pendulum from a horizontal position.

larger impedance values (not shown for brevity); at $K = 1000$ Nm/rad the resonance frequency with the pendulum is 8.5 Hz, well below the torque control bandwidth for both actuators. Therefore, the transparency function is a limiting factor in the actuator performance.

4.5 Conclusions

This Chapter has presented an extensive analysis of the aspects that influence torque control and impedance rendering performance of SEAs. Particularly, stiffness selection and control parameters were discussed in-depth.

Through analysis of the dichotomy of its dynamics, it was shown that generated the torque is the sum of input responses from torque reference and load motion. Several analyses were consolidated to study the effects of mechanical compliance and control parameters on the performance of SEAs in terms of tracking zero and non-zero torques in the presence of load motion, as well as active impedance rendering. Two opposing criteria exist for the choice of stiffness: lowering stiffness

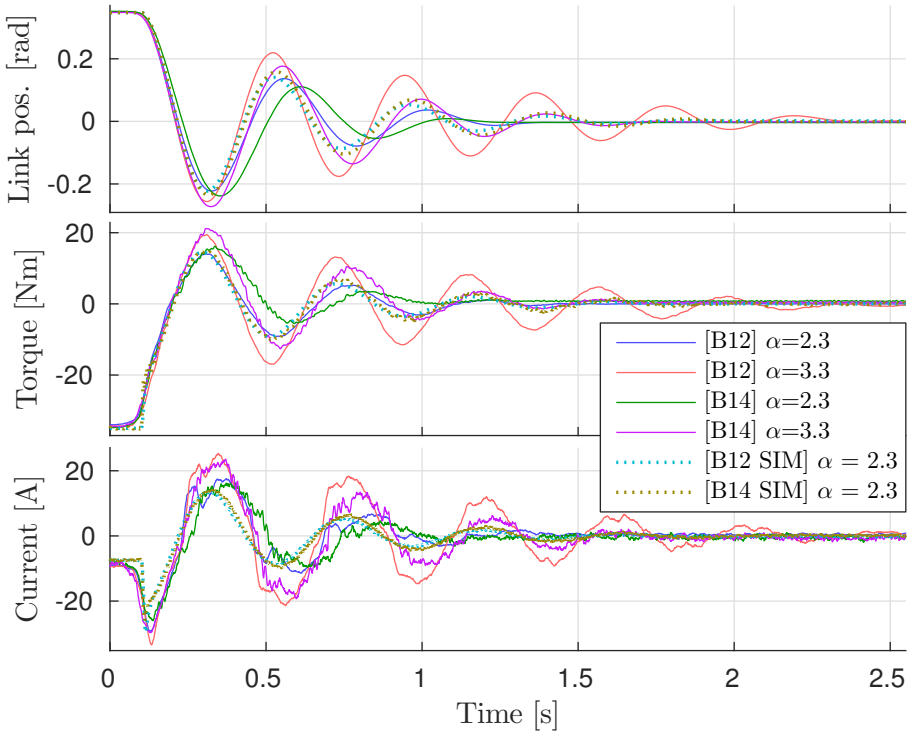

FIGURE 4.13: Experimental impedance rendering for $K = 100\,\mathrm{Nm/rad}$ and $D = 0\,\mathrm{Nms/rad}$.

increases transparency, and increasing stiffness increases achievable torque tracking bandwidth. This fact was used in the context of impedance rendering to propose an optimal stiffness selection criterion, which maximises the frequency up to which an impedance can be rendered accurately. This criterion allows to select the actuator stiffness with respect to force and motion control performance requirements dictated by the targeted robot and field of application. Real-world design is a compromise between many criteria, such as impact resilience, volume, and force/motion control performance.

Results from simulations and experiments were presented to validate the analyses. Particularly, it was shown the stiffness has a significant effect on the renderable impedance values and accurate rendering bandwidth. Experiments showed higher transparency of the more compliant actuator even at very low frequencies, which was unexpected, but may be explained by differences in friction. The analyses and simulations correctly predicted the transparency and impedance rendering dependence on gains. The results from both simulation and experiment confirm our theoretical analyses. Comparing impedance rendering capability in practice proved

difficult; using a secondary motor driving the actuator externally should provide further insight and is left for future study. It is worth noting that while the actuators considered in this Chapter are those with linear stiffness, the results suggest that nonlinear (stiffening) profiles may combine the low stiffness optimal for transparency with the high stiffness optimal for torque tracking.

5

Disturbance Observers for Robust Torque Control

For series-elastic actuators to be an effective core component of high performance robotic systems, they need to be able to provide robust and accurate torque controllability. The previous Chapter presented an extensive linear analysis of the influence of selected physical stiffness and control parameters on their torque properties. Considering that the controlled plant will invariably deviate from the linear model in practice, this Chapter focuses more on the control aspects. Particularly, it focuses on the application of Disturbance Observers (DOBs) to achieve robust, high performance torque control.

This Chapter compares two approaches for applying disturbance observers to the torque control problem of SEAs. It is shown that they are in fact equivalent for linear models in terms of their ability to reject disturbances and enforce nominal model dynamics. The closed loop and error transfer functions for the DOB-based

approaches are compared to a fully linear plant and a nonlinear plant without DOB. Simulations demonstrate that the DOBs are able to increase the bandwidth of the nonlinear plant significantly, up to that of the linear plant. Furthermore, the DOBs significantly increase the tracking accuracy at low frequencies.

The Chapter is structured as follows. First general linear disturbance observers are introduced in Sec. 5.1. Next, Sec. 5.2 formally introduces the two approaches mentioned above, and presents a comparative linear analysis. To compare the approaches in terms of nonlinear behaviours we present a simulation study in Sec. 5.3. Finally, Sec. 5.4 concludes the Chapter.

5.1 Disturbance Observers

In general, linear DOBs produce an estimate $\hat{d}$ of a disturbance d using a linear function of the system input u_d and output y:

$$\hat{d}(s) = -D_1(s)\, u_d + D_2(s)\, \hat{y}. \tag{5.1}$$

where $\hat{y} = y + \eta_o$ denotes the estimate of y, which is affected by measurement noise η_o. The disturbance estimate can be used for observing plant-model deviations or detecting external disturbances such as environmental interaction. Alternatively, it can be added to the input signal for compensation of unmodelled dynamics, which is what we will consider first. In Fig. 5.1, a plant $P(s) := P_n(s) + \Delta(s)$ with nominal dynamics $P_n(s)$ and disturbance dynamics $\Delta(s)$ is augmented with a DOB for compensation. The transfer function from u_c to y then becomes (we omit (s) for brevity):

$$H_{dob}(s) = \frac{P}{1 - D_1 + P\, D_2}. \tag{5.2}$$

The most common linear DOB is based on model inversion. We set:

$$\begin{aligned} D_1(s) &= Q(s), \\ D_2(s) &= P_n^{-1}(s)\, Q(s), \end{aligned} \tag{5.3}$$

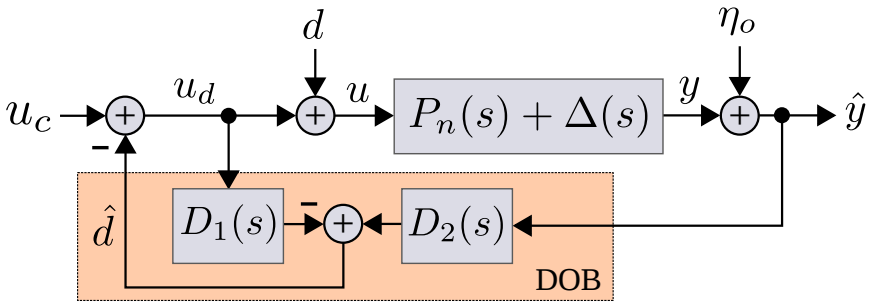

FIGURE 5.1: Generic linear DOB structure.

such that (5.2) becomes:

$$H_{dob}(s) = \frac{P}{1 + Q\left(P\,P_n^{-1} - 1\right)}, \tag{5.4}$$

where P_n is the nominal DOB model and Q is a Butterworth low-pass filter with relative degree greater or equal to that of $P_n(s)$, such that D_2 is proper.

Inspecting (5.4), we find that for low frequencies where $Q(s) \approx 1$, $H_{dob}(s) \approx P_n(s)$, meaning that the composition of plant and DOB together behave like the nominal plant model. Note that due to $Q(s)$ never being exactly unity, this is approximate; the DOB can only attenuate errors. For high frequencies, $Q(s) \approx 0$ and $H_{dob}(s) \approx P(s)$, i.e. the augmented plant behaves like the open-loop plant. Furthermore, if $\Delta \equiv 0$, i.e. the plant is equal to the nominal plant model ($P = P_n$), then $\hat{d} = 0$ and the DOB does not change the plant behaviour. This is known as the transparency property of the DOB.

5.2 Open-loop and closed-loop DOBs

In the previous Section, we have considered an open-loop or plant-only DOB, that is, the DOB was closed around the open-loop plant to enforce its nominal model [10], [38]–[41]. To control this system, a Proportional Derivative (PD) control loop with feed-forward is closed as in Sec. 3.2.2, resulting in the block diagram shown in Fig. 5.2. The transfer function of the closed loop becomes:

$$H_{r\to\hat{y}}(s) = \frac{(\lambda\,P_n + P_n\,C)\,P}{(P - P_n)\,Q + P_n\,C\,P + P_n}. \tag{5.5}$$

As shown in the previous Section, for low frequencies where $Q \approx 1$, the transfer function of plant with DOB P_d (Fig. 5.2) is approximately equal to the nominal model $P_n(s)$:

$$P_d(s) = H_{dob}(s) \approx P_n(s) \tag{5.6}$$

and the closed-loop transfer function (5.5) simplifies to:

$$H_{r\to\hat{y}}(s) \approx \frac{\lambda P_n + P_n C}{1 + P_n C}, \tag{5.7}$$

which is the controlled nominal plant as desired. Conversely, when $Q \approx 0$, we find (5.5) simplifies to the controlled plant.

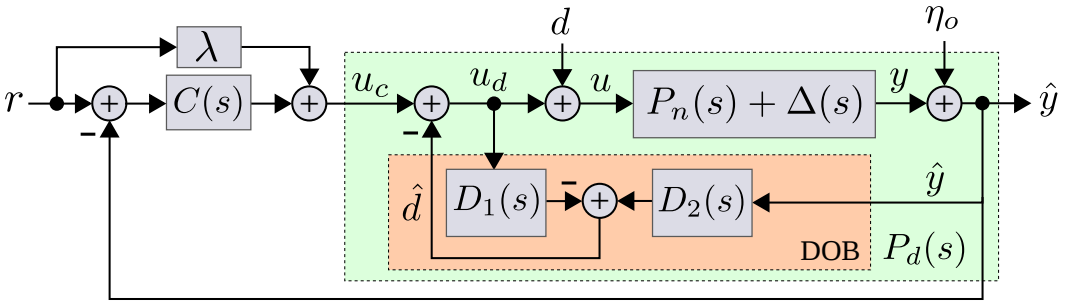

FIGURE 5.2: Open-loop DOB.

Investigating further, we derive the transfer functions from input disturbance d and output disturbance/noise η_o. For the input disturbance d, this results in:

$$H_{d\to\hat{y}}(s) = \frac{(1-Q)\,P\,P_n}{(P-P_n)\,Q + P_n\,C\,P + P_n} \tag{5.8}$$

which for $Q \approx 0$ simplifies to $H_{d\to\hat{y}}(s) \approx \frac{P}{C\,P+1}$ (no rejection of the input disturbance), and for $Q \approx 1$ simplifies to $H_{d\to\hat{y}}(s) \approx 0$ (perfect rejection of the input disturbance). Similarly, for the output disturbance η_o this results in

$$H_{\eta_o\to\hat{y}}(s) = 1 - \frac{(C\,P_n + Q)\,P}{(P-P_n)\,Q + P_n\,C\,P + P_n} \tag{5.9}$$

which for $Q \approx 0$ simplifies to $H_{\eta_o\to\hat{y}}(s) \approx 1 - \frac{C\,P}{C\,P+1}$, and for $Q \approx 1$ simplifies to $H_{\eta_o\to\hat{y}}(s) \approx 0$.

Note that as $\hat{y} = y + \eta_o$, the propogation of output disturbances into y differs from that into $\hat{y}$; for $Q \approx 0$ we have $H_{\eta_o\to y}(s) \approx -\frac{C\,P}{C\,P+1}$, and for $Q \approx 1$ we have

$H_{\eta_o \to y}(s) \approx -1$. Since neither of these is zero, we find the DOB cannot compensate for sensor bias and other measurement disturbances.

In the closed-loop DOB configuration [11]–[13], the DOB is placed around the controlled plant, as in Fig. 5.3. The nominal model utilised by the DOB is then based on the closed-loop dynamics of the controlled nominal plant. The benefit of this configuration is that the entire closed-loop behaviour can be shaped by choosing a desired nominal model, as the DOB is the outer-most loop. However, generally, changing the controller parameters requires the DOB model to be re-identified. Additionally, the DOB model is of higher order: it includes the combined transfer functions of the controller and plant model.

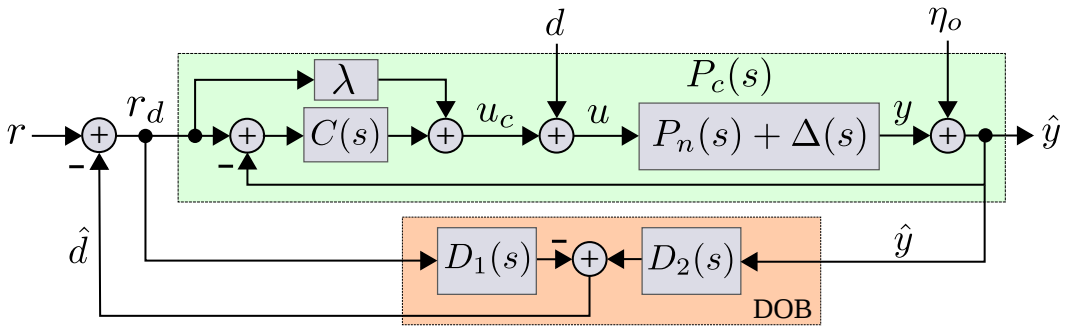

FIGURE 5.3: Closed-loop DOB.

In this closed-loop DOB configuration, the controlled plant $P_c(s)$ seen by the DOB is as follows:

$$P_c(s) = \frac{P\,(\lambda + C)}{1 + P\,C}. \tag{5.10}$$

By now choosing $D_2(s)$ based on the nominal controlled plant:

$$D_2(s) = \left[\frac{P_n\,(\lambda + C)}{1 + P_n\,C}\right]^{-1} Q \tag{5.11}$$

and substituting, we obtain (5.5), which again is equal to (5.7) for frequencies where $Q(s) \approx 1$. Similarly, writing the transfer functions from input disturbance d and output disturbance η_o, we again find (5.8) and (5.9) respectively, which are equal to those for the open-loop DOB case.

Note that in the closed-loop DOB configuration, for D_2 to be proper, the relative degree of Q has to be greater or equal to that of the plant plus controller (unless

choosing to neglect certain higher frequency dynamics in the nominal DOB model, in which case both can be simplified).

From the above analyses we find that for linear models the two approaches are in fact equivalent, in terms of their ability to reject both input and output disturbances, and enforcing nominal model dynamics. For frequencies up to the cut-off of the Q-filter, the nominal plant $P_n(s)$ is enforced in both configurations, given model disturbances $\Delta(s)$. Furthermore, input disturbances are fully rejected at these frequencies. Output disturbances however are not compensated for by either DOB structure. As noted earlier, this enforcement of nominal model dynamics and disturbance rejection is approximate due to Q only approaching unity; i.e. the DOB can only attenuate errors. Additionally, in practice, the nonlinear nature of disturbance dynamics as well as actuator and sensor limitations limit the disturbance rejection and model variation rejection capabilities of DOBs.

Obtaining the nominal plant that is to be inverted by the DOB (in (5.3) and (5.11), respectively) can be done in two ways. In [11], [40], the model was obtained by constructing a transfer function based on a model similar to that derived in Sec. 3.1 in rigid-gearbox, locked-output configuration. In [10], [12], [13], [38], [41], the nominal model was obtained by identification of the real system. In this work, we do the latter; we obtain model parameters from experimental identification. For simulation, we assume these parameters perfectly describe the plant, i.e. the DOB has a perfect model of the linear plant dynamics.

As a measure of disturbance observer robustness, [13] presented the Disturbance observer Region Of Convergence (DROC), which guarantees a bounded tracking error of the DOB resulting from model variation. This proved especially useful to investigate up to what minimum load inertia the assumption of infinite output inertia guarantees a specified bounded tracking error. Below we briefly illustrate that the DROC is identical for the open- and closed-loop DOB cases, and as such cannot be used to compare the relative performance or robustness of the approaches.

5.2.1 Disturbance observer Region Of Convergence (DROC)

We obtain the DROC by setting a desired maximum deviation $H_\delta(s)$ from the nominal closed-loop response, and solve for the plant dynamics P that result in this closed-loop response. This allows us to directly see the effect of plant disturbances onto the closed-loop response. Setting $H_{r\to y}(s) = H_\delta(s)$ and solving for P, we obtain the maximum deviation of the plant dynamics from the nominal model. For both the open-loop DOB (Fig. 5.2) and closed-loop DOB (Fig. 5.3) this results in:

$$P_\delta = \frac{H_\delta\ (Q-1)}{H_\delta\, Q\, P_n^{-1} + (H_\delta - 1)\, C - \lambda}. \tag{5.12}$$

The implication is that for disturbances acting on linear plants, the robustness to plant disturbances is identical for both DOB configurations; i.e. the admitted plant variation is identical whether the DOB is the inner loop or outer loop.

5.3 Simulation Results

In this Section, we perform a simulation study that demonstrates the potential of DOB based approaches as well as where the behaviours of the open- and closed-loop DOB approaches differ. In all cases, we use the identified linear dynamics of the plant to construct our nominal DOB models, and set the Q-filter cut-off frequency to 70 Hz. Each system uses the same PD controller gains, where α was selected such that the considered input saturation of 40 A occurs just after the -3 dB point for the linear model. As is common in literature, we have chosen a sine sweep with 10 Nm amplitude as reference. We compare four systems:

- Fully linear model with symmetric viscous friction only;
- Nonlinear model (asym. Coulomb and viscous);
- Nonlinear model with open-loop DOB;
- Nonlinear model with closed-loop DOB.

Again, we include the input and sensor noise levels as measured from the real system. Furthermore, we found particularly high Coulomb friction in our testing setup, which will be useful to emphasise the effectiveness of DOB-based approaches.

We investigate the performance of the DOB-based approaches in terms of enforcing their nominal model on the highly nonlinear plant. The resulting closed-loop transfer function $H_{r\to y}$ is shown in Fig. 5.4. Both DOB-based approaches perform similarly, reaching a bandwidth of ≈60-65 Hz, similar to the linear model, despite the low controller gains.

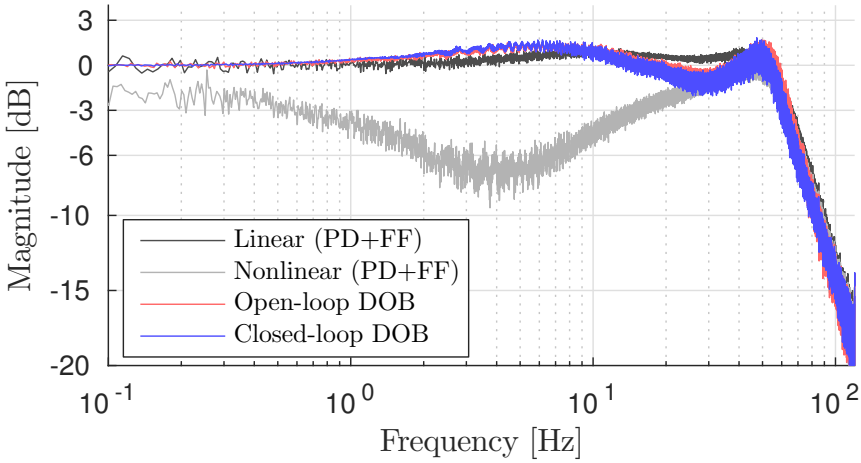

FIGURE 5.4: Closed-loop transfer function $H_{r\to y}$.

Additionally, we calculate the error transfer function $H_{r\to e}(s) = \frac{Y(s)-R(s)}{R(s)}$, which is useful to analyse the attenuation of tracking errors, shown in Fig. 5.5. The DOBs improve the low-frequency error rejection by up to 15 dB compared to the linear model, by rejection of the Coulomb friction torques. This can be explained by integrating action resulting from the DOB.

By comparison, the addition of nonlinear dynamics in the form of significant Coulomb friction results in a bandwidth of <1 Hz of the nonlinear 'no DOB' case. Much higher gains are required to achieve similar performance, which result in abrupt input saturation at higher frequencies.

From these results it is clear that DOB-based approaches can significantly improve tracking accuracy and error rejection, and can be used as an alternative to high controller gains. However, there is no significant difference in performance of the two DOB configurations.

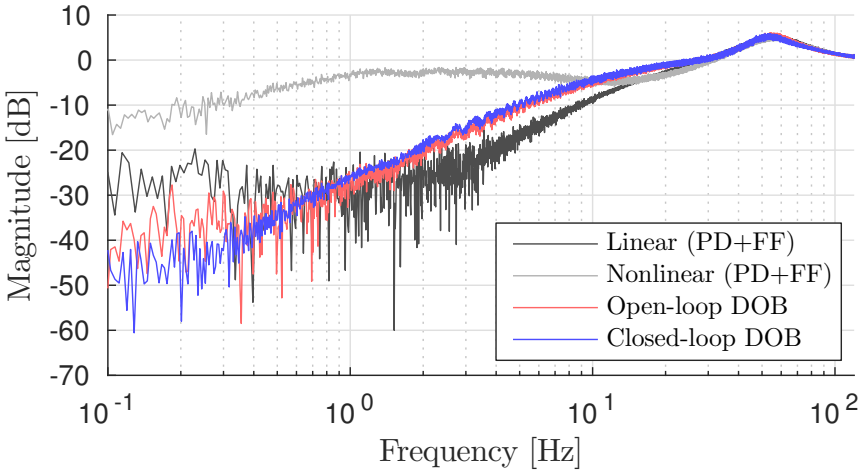

FIGURE 5.5: Error transfer function $H_{r\to e}$.

5.4 Conclusions

Two approaches for applying DOBs to the torque control problem of SEAs were compared. In the first approach, the open-loop DOB (plant-only DOB), the plant is augmented with a DOB to enforce nominal dynamics and the resulting system is controlled. In the second approach, the controlled nonlinear plant is augmented with a DOB that uses a nominal model based on the controlled nominal plant model. We compared the approaches and demonstrated their equivalence for linear models, in terms of their ability to reject disturbances and enforce nominal model dynamics.

To compare the approaches when applied to the nonlinear plant, a simulation study was presented. The closed loop bandwidth and error transfer functions for the DOB-based approaches were compared to a linear plant and a nonlinear plant without DOB. Our simulations report that the DOBs are able to increase the bandwidth of the nonlinear plant up to that of the linear plant. By comparison, the nonlinear plant without DOB results in a bandwidth of $<$1 Hz, requiring much higher gains to achieve similar performance. Furthermore, the DOBs increase the low frequency error rejection by up to 15 dB compared to the linear model, due to integrating action from the DOBs.

However, the results showed no significant difference in performance of the two DOB configurations. This in fact votes for the open-loop DOB; it uses lower-order

models and has the practical benefit of not requiring re-identification of the closed-loop dynamics when changing controller gains.

Part II

Parallel Compliance in Articulated Robots

6

Background, Related Work, and Contributions

Addition of compliant elements in parallel to the main actuation branches, known as Parallel Compliant Actuations (PEAs), has seen less adoption than SEA, which was the focus of Part I of this thesis. However, their benefits have been repeatedly demonstrated, particularly in terms of energy efficiency: in actuator test bench setups [43]–[47], hopping robots [48], and bipedal walkers [49], [50]. Compliant elements can also be used to compensate for gravitational effects on a system, e.g. by placing pretensioned compliant elements in parallel with the primary actuation mechanism [51]. This can result in large benefits in terms of energy efficiency.

Another field of application is that of prostheses, where parallel compliance has been utilised in prosthetic ankles [52]–[54] and knees [55], [56], to reduce the motor torque required to produce the desired deflection-torque profiles.

6.1 Adjustable Parallel Compliance

A common challenge with parallel compliance is that during some stages of the motion the torque generated by the parallel element does not correspond well to the desired torque on the joint. The result of this is that the main actuation drive has to work against the parallel compliance in order to obtain the desired joint torque or motion.

To address this, many works employ unidirectional elements [43], [50], [52]–[54], clutches/switches [44], [46], [48], [55], [57], secondary motors to change the pretension [45], [47], [53], or a combination of these concepts to engage and disengage the parallel elements at desired moments.

The design proposed in [45] used a mixed series–parallel approach; multiple SEA branches were placed in parallel, each engaged as required depending on the torque requirements. The design uses an intermittently driven self-locking mechanism that does not require any motor torque once a branch has been fully engaged. The authors showed a significant reduction in required motor torque, and an increased torque output range compared to traditional stiff or SEA setups.

[46] employed a clutched differential mechanism that allowed to store energy in the internal spring, which could then be released to accelerate the joint in the desired direction by operating the appropriate clutch.

For legged robots, the swing/flight phase has significantly different knee torque requirements than the stance place. To address this, [48] employed a switching mechanism that disengages the parallel knee stiffness based on whether the foot was in ground contact. A similar switching approach based on an electrically operated clutch was proposed in [44]. [49] used unidirectional spring elements in the knees of a bipedal walker and found significant energy efficiency increases. Their design optimisation found that optimalities exist w.r.t. stiffness tuned to walking speed.

The ankle joint also exhibits the same phase-dependent torque behaviour. Particularly, high torques are required at the moment of push-off, while during initial stance and swing the torque requirements on the ankle are generally small. To this end, [52]

and [53] employed unidirectional parallel elements. An interesting cam-based approach is proposed in [54] allows more freedom to shape the deflection–torque profile. Lastly, [57] also proposed a unidirectional parallel spring element in the ankle joint of an exoskeleton.

[58] considered parallel stiffness as a static balancing mechanism in multi-DoF manipulators, which results in complex design however also large energy efficiency benefits as well as safety in the case of catastrophic failures in active actuation.

6.2 Comparing Series- and Parallel-Elastic Actuation

Some works have compared the benefits and drawbacks of SEA and PEA, mainly in torque and power requirements. The role of compliant actuation systems in improving energy efficiency was studied analytically in [16], by considering cyclic hoppers with various combinations of series and parallel compliance. The authors analytically derived the optimal stiffness and pretension of SEA and PEA systems for given desired trajectories of multi-DoF systems. In simulation studies it was shown that the use of compliant actuation can yield very large energy efficiency benefits compared to traditional stiff actuation. Other authors also considered cyclic hoppers [59], and SEA and PEA were compared in the context of exoskeleton actuation in [57]. Another work [60] compared SEA and PEA in terms of power and energy consumption on a single joint, particularly during oscillatory motions.

In [61], it was shown the combination SEA+PEA can yield some further benefits. In general, the varied results suggest that whether SEA or PEA yields the largest benefit depends on the application. Specifically, exploiting the use of motions that coincide with the system's natural frequency appears to be suitable for the energy efficient application of SEA [60], as is also evidenced by the results on hoppers. However, this approach inherently limits the energy efficient operation to those frequencies. On the other hand, PEAs are well suited for potential energy balancing of systems, such as those under gravitational load [58].

6.3 Biarticulation in Biology

Many biological systems have been found to contain biarticulated muscle structures, where a single muscle spans multiple joints. The human body incorporates many biarticular muscles; for example the rectus femoris and hamstrings, which span the hip and knee joints as an antagonistic pair, the biceps that spans the shoulder and elbow, and the gastrocnemius muscles, which spans the knee and ankle joints.

In the field of biomechanics, biarticulated muscles have been identified to transfer mechanical power between joints [62], [63]. The gastrocnemius muscles, for example, allow for power transfer from knee to ankle joint. This allows to use the powerful quadriceps muscles in ankle actuation as the knee approaches full extension, thereby greatly increasing jumping height.

6.4 Biarticulation in Robotics

Considering the benefits reported in biological systems, several authors have sought to employ multi-articulated actuation in articulated robots.

In [64], the transfer of mechanical power between joints was experimentally demonstrated in a leg that models all nine major muscle groups in the human lower limb in the saggital plane. In [65] and [66], biarticulation was used in walking and jumping, respectively. [67] showed how biarticulation can improve the end-effector force ellipsoid. The recently introduced compliant bipedal walker [68] also includes a biarticulated tendon spanning ankle and knee. [69] showed the benefits of a biarticulated compliant tendon spanning the ankle and knee joints in terms of jumping height through optimised motions of – and experiments with – a jumping robot.

These works have effectively demonstrated the utility of biarticulation in robotic systems, in terms of improving force regulation, energy efficiency and peak power properties.

6.5 Contributions

Despite the promising results reported in literature, substantial energy efficiency improvements have not commonly been demonstrated on real-world systems. This is because both the design and control of such actuators is not sufficiently well understood yet. One area that could particularly benefit from high performance, energy efficient, compliant actuation is legged robotics, which require high performance in terms of energy efficiency and power output for tasks such as running, jumping or kicking.

The recently introduced asymmetric compliant joint concept [3], [4] by Tsagarakis et al. employs a highly asymmetric design that combines a high power motion branch with an energy storage and load compensation branch. The high power branch is based on the SEA principle with a relatively stiff torsional transmission. The parallel energy storage branch consists of a small motor with high reduction transmission and a linear elastic element. The linear elastic element has relatively low stiffness and is able to store a large amount of elastic energy. The adjustable properties of the energy storage branch permit the regulation of the equilibrium of the elastic element for the purpose of minimizing the effort required to execute tasks including slowly varying periodic profiles or for gravitational load compensation.

The work presented in the second part of this thesis found its origin in the aforementioned combined series-parallel approach, which we refer to as Asymmetric Compliant Actuation (ACA). Chapter 7 builds on the previous work by Tsagarakis et al., significantly contributing on the tuning and control of this asymmetric compliant joint for energy efficient operation. Specifically, we propose a novel distributed control strategy which is applied to this dual actuation system. This distributed control strategy actively utilises both actuation branches to perform the desired motion. In contrast, in previous works by Tsagarakis et al. the pretension of the energy storage branch was manually set to a constant value. Furthermore, we present a more extensive modelling approach with promising simulation results in terms of electrical energy efficiency as well as reduced torque requirements over a wide reference frequency range. Our experimental results illustrate the potential of the control

method, by a significant reduction in electrical power consumption of up to 65%.

Building on that work, Chapter 8 extends and generalises the concepts to provide the necessary guidelines for future development of more complex systems and, ultimately, integration on humanoids such as WALK-MAN [2]. It significantly contributes by:

- Generalising the design and control concepts of asymmetric compliant actuation to multi-DoF systems;
- Extending the asymmetric compliant actuation principle to biarticulated actuation structures;
- Proposing a novel method for optimizing the parameters of these multi-DoF asymmetric compliant actuation configurations to improve their energy efficiency.

Most existing humanoids and many other robotic systems employ stiff or conventional series-elastic actuation. Thus, we use SEA as the basis for comparison against our methods.

Comparative simulation studies performed on a 2-DoF leg model demonstrate significant energy efficiency benefits in electrical energy efficiency and reduction in peak torque and electrical power requirements. A biarticulated actuation arrangement is shown to further improve energy efficiency.

Indeed, we believe that the ACA concept can improve the energy efficiency and power autonomy of many robotic platforms.

Chapter 9 brings the advancements presented in the previous chapters into practice, and introduces the novel design of a 3-DoF leg with series and parallel compliant actuation using the ACA concept, both with monoarticulated and biarticulated actuation configurations. The leg is designed such that the actuation configurations are rapidly interchangeable, to allow for comparison.

In this work we present the concept and the realised prototype, as well as initial experimental results that show the concept's potential.

In addition, the experimental comparison study on the energetic performance of the SEA, monoarticular and biarticular principles, using the same standard hardware and motion profiles, provide initial indications on how the three actuation configurations affect the energetic economy of the leg.

Lastly, Chapter 10 focuses on the model formulation and control of such compliant actuation arrangements including multiple branches and multi-articulation, and significantly contributes by:

- Proposing an elegant modular formulation that describes the energy exchange between the compliant elements and articulated multi-body robot dynamics using power flows and a single matrix that describes the entire actuation topology, and;
- Uses this formulation to derive a novel gradient descent based control law for compliant actuation structures with adjustable pretension, with proven convexity for arbitrary actuation topologies.

7

Development and Control of a 1-DoF Leg with Parallel Compliance

This Chapter presents the modelling and control of a novel Asymmetric Compliant Actuation (ACA) scheme, a concept originally presented in [3], [4], and characterised by large energy storage capacity that enables efficient execution of motions. The asymmetric design consists of two actuation branches which transfer their power to a single joint through two compliant elements with different stiffness and storage capacity properties. The guideline for selecting the stiffness of both elements is elaborated, given the design parameters and control requirements. We propose a novel control strategy that distributes the effort required to generate the motion between the two actuation branches of this novel hardware, to drive the prototype joint in

an energy efficient manner. As a proof of concept, a single degree of freedom knee-actuated hopping robot is used for experimental validation. The dynamics of the leg and actuators are rigorously modelled and formulated. The data from simulation and experimental studies report a significant improvement in electrical energy efficiency and reduction in torque requirements; Our experimental results demonstrate a reduction in electrical power consumption of up to 65%.

The Chapter is structured as follows. Sec. 7.1 elaborates the asymmetric compliant joint actuation scheme, followed by the mechanics of the 1-DoF leg prototype that is used to illustrate the principle. Furthermore, it discusses the modelling of both actuator and leg. Sec. 7.3 discusses the methods used for selecting the stiffness of both actuation branches. Sec. 7.4 presents our novel control strategy for this hardware. Simulation and experimental studies are presented and data are analysed in Sec. 7.5 and 7.6. We conclude with a discussion of the results in Sec. 7.7.

7.1 Asymmetric Compliant Joint Design

The main components of the asymmetric compliant design are shown in Fig. 7.1. The link is driven by two parallel force controlled actuation branches allocated in an antagonistic configuration of high asymmetry, which is dedicated to enhancing energy efficiency.

The first branch is designated as the PB, and is a rotational drive based on Series-Elastic Actuation that consists of a high power motor M1 in series with a torsional elastic transmission SE, intended for impact absorption. The second branch is designated as the ESB, and consists of a lower power motor M2 combined with a high reduction linear transmission. The motor transfers its power to the joint through a unidirectional elastic element PE. The main characteristic of the elastic element PE is the very large elastic energy storage capacity.

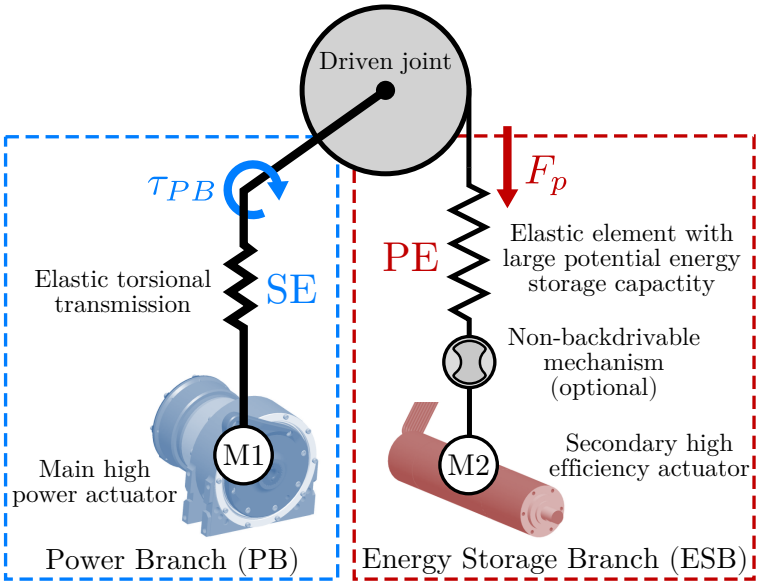

FIGURE 7.1: Concept of the asymmetric compliant joint.

7.1.1 1-DoF Leg Prototype

In this Chapter we focus on a one DoF proof of concept, on which the benefits in terms of electrical power consumption and torque requirements are clearly demonstrated. The work presented in this manuscript serves as an important proof of concept prior to further investigation of more complex systems. To validate the effectiveness of the asymmetric compliant joint, a single DoF knee-actuated leg was developed, shown in Fig. 7.2 and 7.3.

The Power Branch is actuated by a brushless DC motor combined with a Harmonic Drive transmission with reduction of 80:1 (Fig. 7.4a). The series elasticity is implemented by a flexible torsional transmission between the gearbox and the output link. It is augmented with three position sensors: An incremental optical encoder (12-bit) is mounted at the motor side before the gearbox, a second incremental optical encoder (19-bit) is mounted after the gearbox before the flexible torsional transmission element, and a third absolute capacitive encoder (19-bit) is placed after the flexible transmission and measures the PB output angle (link side) after the torsional transmission. By monitoring the deflection of the torsional transmission bar using the last two encoders and knowing its stiffness, the torque provided by motor M1 is estimated. The output transfers its power to the knee joint through a 4-bar linkage with 1:1 velocity ratio.

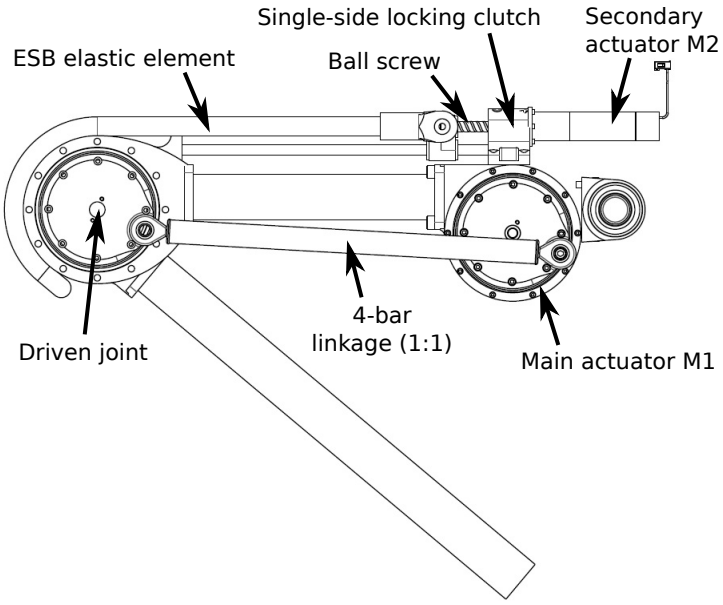

FIGURE 7.2: Schematic of the leg design showing its main components.

The main requirement for the Energy Storage Branch is to store a large amount of potential energy. To achieve this we utilise rubber-type elastic cords. The cords are constructed from a number of elastic strands enclosed inside a woven braided cotton sheath. The cords are pretensioned using a secondary actuator M2 (Fig. 7.2 and 7.4b) that drives a highly efficient ball screw of 10 mm pitch. A load cell is fitted at the connection between the linear drive and elastic elements so that it allows measuring directly the linear force generated by the elastic elements, and thus the joint torque generated by the branch. The secondary actuator itself consists of a brushless DC motor (Maxon EC22, 100 W) with 29:1 planetary reduction gearbox with peak torque of 3 N·m. Due to the combined transmission ratio of the reduction gearbox and ball screw, the torque requirement on the ESB motor is small, which reduces the required current and thus heat dissipation, resulting in a high efficiency drive. To unload the actuator when the pretension position is constant, the actuator is coupled to the ball screw through a two side overrunning clutch, which implements the non-backdrivable mechanism shown in Fig. 7.1. More details on the mechanical design can be found in [3], [4].

Both actuators were positioned close to hip level to reduce the distance to the center of mass of the leg links, and thus to minimise inertia of the leg, enabling lower

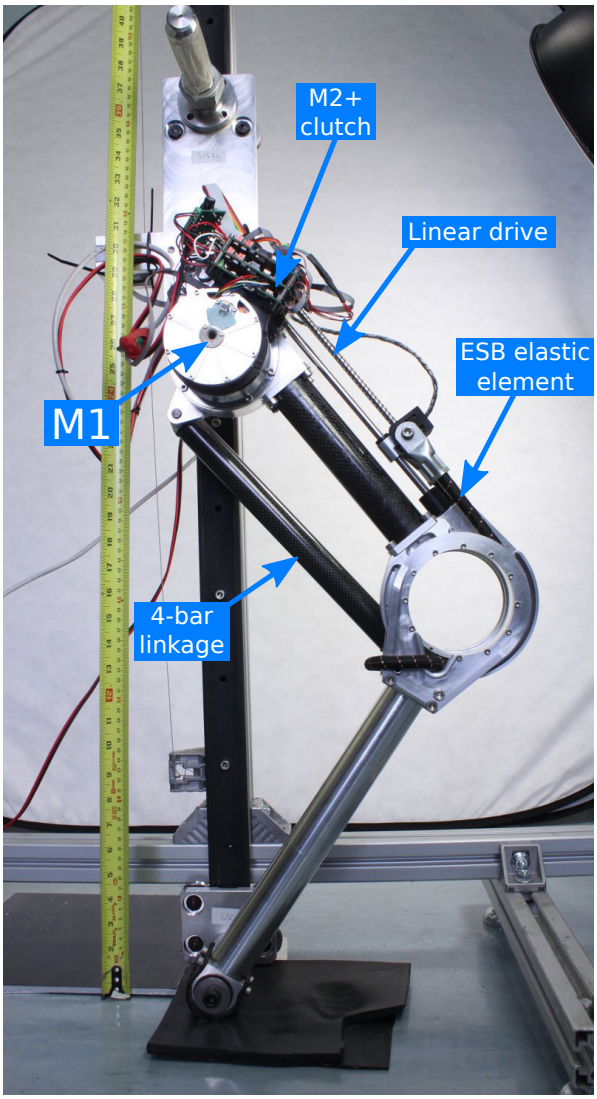

FIGURE 7.3: Prototype of 1-DoF leg setup used in the experimental validation.

power consumption during dynamic motions. Some structural components are constructed of carbon fibre, chosen for its high strength-to-weight ratio, reducing total mass while maintaining structural rigidity. As an exception, the lower leg segment is made from metal, as it has to bear very high impact forces in dropping and jumping experiments, making carbon fibre less suited.

7.2 Modelling of Leg and Actuator Dynamics

In this Section, we present the modelling and analysis of the actuator and 1-DoF leg prototype. In the following formulation, we take a modular approach by modelling

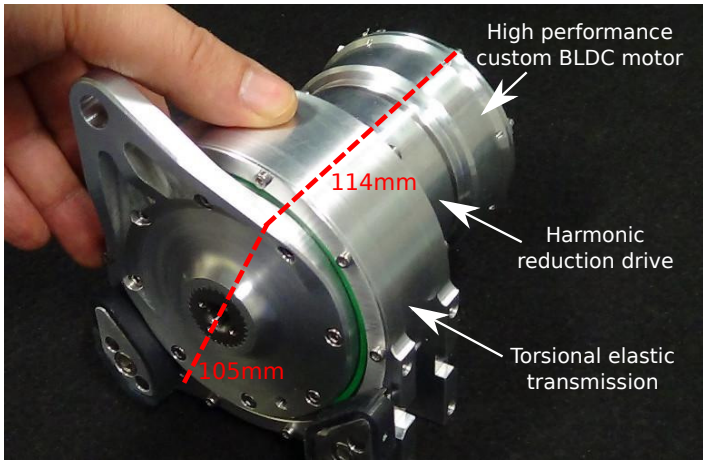

(A) High performance Power Branch (PB) drive.

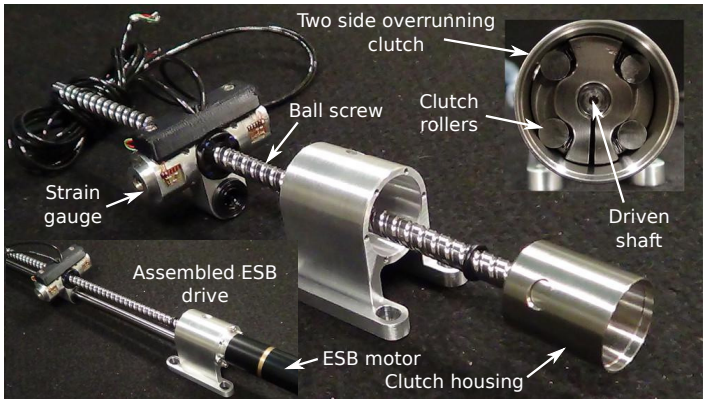

(B) Energy Storage Branch (ESB) drive.

FIGURE 7.4: Actuation drives for both branches.

actuator and leg separately, which allows the actuator model to drive joints in other applications as well. As the goal of both models is the analysis and controller design, and we do not expect friction effects to be the dominant behaviour, we model all frictions as purely viscous for simplicity. This reduces the number of parameters and allows to use linear representations of the models.

7.2.1 Leg Modelling

The leg model (Fig. 7.5) consists of two links of length l connected by an actuated knee joint. The links have masses m_1, m_2 and rotational inertiae J_1, J_2 respectively. On the hip, which is constrained to vertical movement, is an additional mass m_3 which is a lumped mass representing components of the actuator and the load. The

lower link pivots around the ground contact point (i.e. we assume the foot is in contact with the ground without slippage, so that it can be considered fixed), resulting in a 1-DoF system.

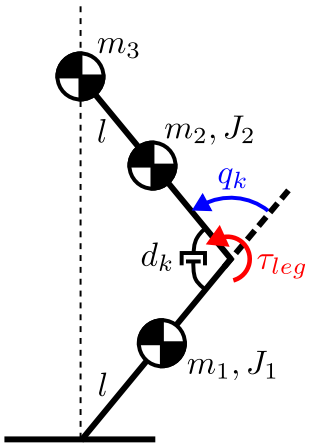

FIGURE 7.5: 1-DoF leg model.

The dynamics of this model are described by

$$\ddot{q}_k = M(q_k)^{-1} \left[\tau_{leg} + G(q_k) - \tau_d\right] \tag{7.1}$$

where q_k denotes the knee angle as in Fig. 7.5, τ_{leg} denotes the actuator torque at the knee, $\tau_d = d_k \dot{q}_k$ denotes joint friction, and $G(q_k)$ denotes the generalised gravitational torque:

$$G(q_k) = J(q_k)^T G_c \tag{7.2}$$

where $J(q_k)$ denotes the system Jacobian:

$$J(q_k) = \begin{bmatrix} \frac{l}{4}\cos(q_k/2) \\ -\frac{l}{4}\sin(q_k/2) \\ -\frac{1}{2} \\ \frac{l}{4}\cos(q_k/2) \\ -\frac{3l}{4}\sin(q_k/2) \\ \frac{1}{2} \\ -l\sin(q_k/2) \end{bmatrix}, \tag{7.3}$$

the gravitation vector G_c is given by

$$G_c = [0, -m_1 g, 0, 0, -m_2 g, 0, -m_3 g]^T \tag{7.4}$$

and $g = 9.81$ m/s^2. Notice that since the hip is constrained to vertical movement we do not need to consider its horizontal movement and rotation. Thus, we can neglect these from the derivation. In all notation, $\dot{[.]}$ denotes the time derivative and $[.]^T$ denotes the matrix transpose. We ignore the centripetal and Coriolis forces, as we only consider low-velocity motions. The generalised inertia matrix $M(q_k)$ is given by

$$M(q_k) = J^T(q_k)\, M_c\, J(q_k) \tag{7.5}$$

with the nominal inertia matrix M_c defined as

$$M_c = \text{diag}\,(m_1, m_1, J_1, m_2, m_2, J_2, m_3)\,. \tag{7.6}$$

7.2.2 Actuator Modelling

The actuator model is shown in Fig. 7.6. We include the electrical dynamics of the motors of both branches, in which I_{E1}, I_{E2}, d_{E1} and d_{E2} denote the winding induction and resistance values of M1 and M2 respectively. The currents in the motors are denoted as i_1 and i_2, and the torque constants are denoted as g_1 and g_2, respectively.

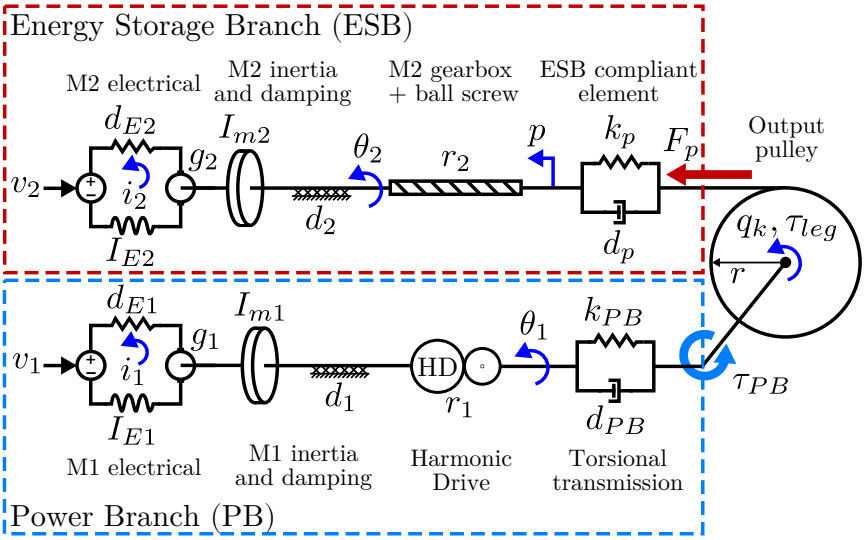

FIGURE 7.6: Dynamics model of the actuator ESB and PB branches.

In the mechanical domain of the Power Branch, the M1 and Harmonic Drive inertia and damping are lumped and denoted as I_{m1} and d_1 respectively. The Harmonic Drive transmission ratio is denoted as r_1. The torsional transmission bar is modelled as a spring-damper with stiffness k_{PB} and damping d_{PB}, such that the resulting torque contribution on the knee joint τ_{PB} is given by

$$\tau_{PB} = k_{PB}\,\Delta_{PB} + d_{PB}\,\dot{\Delta}_{PB}, \tag{7.7}$$

where $\Delta_{PB} = q_1 - q_k$ denotes the deflection of the torsional transmission of the Power Branch.

In modelling the Energy Storage Branch, the ball screw inertia is neglected, due to its low value and transmission ratio of the M2 gearbox. The M2 inertia is denoted as I_{m2} and the lumped reflected damping of M2 and the ball screw at the motor side before the reduction is denoted as d_2. r_2 denotes the combined M2 gearbox and ball screw transmission ratio, and the ESB transfers its power to the joint through the output pulley with radius r_k. Note that the non-backdrivable mechanism is ignored in the model. We do so because it would complicate modelling and the mechanism is not active in our proposed control strategy.

It is evident that the rubber type elastic element in the leg prototype only applies elastic force under extension, i.e. only negative knee torques can be generated. Therefore the ESB energy storage element PE is modelled as a nonlinear spring-damper combination, which is unidirectional:

$$F_p = \begin{cases} k_p\,\Delta_p + d_p\,\dot{\Delta}_p & \Delta_p > 0 \\ 0 & \text{otherwise} \end{cases} \tag{7.8}$$

where k_p denotes the spring constant, d_p denotes the damping and Δ_p denotes the spring extension, given by $\Delta_p = p + r_k\,q_k$, where the pretension position p is set by motor M2 as $p = r_2^{-1}\theta_2$. The torque generated by the ESB on the knee joint is then given by $\tau_p = -r_k\,F_p$, and the net joint torque τ_{leg} is given by the sum of contributions of PB and ESB: $\tau_{leg} = \tau_{PB} + \tau_p$.

The Port-Hamiltonian method was used to derive the actuator dynamics, and written as a set of first-order coupled differential equations:

$$\dot{\mathbf{x}} = \mathbf{f}(\mathbf{x}) + \mathbf{g}(\mathbf{u}) \tag{7.9}$$

where the state $\mathbf{x}$ is defined as

$$\mathbf{x} = \left(i_1, i_2, \dot{\theta}_1, \dot{p}, \Delta_{PB}, \Delta_p, \theta_1, p\right)^T \tag{7.10}$$

where i_1 and i_2 denote the motor currents, $\dot{\theta}_1$ and $\dot{p}$ denote the motor velocities in Fig. 7.6, and θ_1 and p are integrating states to obtain the PB motor and pretension positions. The input vector $\mathbf{u}$ is defined as

$$\mathbf{u} = (v_1, v_2, \dot{q}_k)^T \tag{7.11}$$

where v_1 and v_2 denote the motor input voltages, and $\dot{q}_k$ denotes the output link velocity (coming from the leg model).

7.3 Stiffness Selection Guidelines

Having derived the models of the actuator and leg prototype, this Section introduces the guideline for selection of the stiffness of the compliant elements in the two actuation branches. Based on the gravitational load, stiffness, and inertial properties, the stiffness of the elastic elements can be selected to achieve two goals:

1. Set the anti-resonance of the leg system above a specific frequency that satisfies the trajectory and control bandwidth requirements.
2. Provide a desired load compensation for improved energy efficiency and reduced torque/power requirements.

7.3.1 Energy Storage Branch Stiffness

The capability to adjust the pretension of the large elastic element PE allows to optimise energy efficiency or to generate high peak power output. A way to minimize the energy required from the Power Branch is to use the Energy Storage Branch to provide gravity compensation on a joint by appropriately selecting the ESB stiffness k_p and the pretension p. By choosing these parameters well, the elastic element PE can be used to generate torque on the knee joint to counteract the gravitational load on a wide range of knee joint angles.

By neglecting the damping component, i.e. assuming quasi-static compensation, the torque generated by elastic element PE can be written in the following linear form with respect to knee joint angle q_k:

$$\tau_p = \varphi_1(k_p, p, r_k) + \varphi_2(k_p, r_k)\, q_k \tag{7.12}$$

where φ_1 and φ_2 are functions of the stiffness k_p, pretension p and pulley radius r_k, and given by $\varphi_1(k_p, p, r_k) = r_k\, k_p\, p$ and $\varphi_2(k_p, r_k) = -r_k^2\, k_p$.

The objective is to select the stiffness and pretension of the elastic element to compensate for the gravitational load $G(q_k)$ as close as possible. In other words, we want to determine the values of the optimal linear coefficients φ_1 and φ_2 in (7.12) to closely match the gravity load for the full range of motion of the knee joint. Assuming the knee pulley radius r_k is known, this allows us to derive the optimal parameters k_p and p. Considering now an arbitrary motion that exploits the full range of the leg ($0 < q_k < 2.5$ rad) in Fig. 7.5, the optimal values of coefficients φ_1 and φ_2 can be computed by solving the linear least square problem with the following objective function, that minimizes the residual of the torque τ_p produced by the PE and the gravity term $G(q_k)$:

$$\min \int_0^{2.5} ||\varepsilon||^2 \, \mathrm{d}q_k \tag{7.13}$$

with $\varepsilon = \tau_p(q_k) - G(q_k)$. Fig. 7.7 shows the derived optimal fitted line for $\varphi_{1,opt} = -2.62$ and $\varphi_{2,opt} = -16.96$.

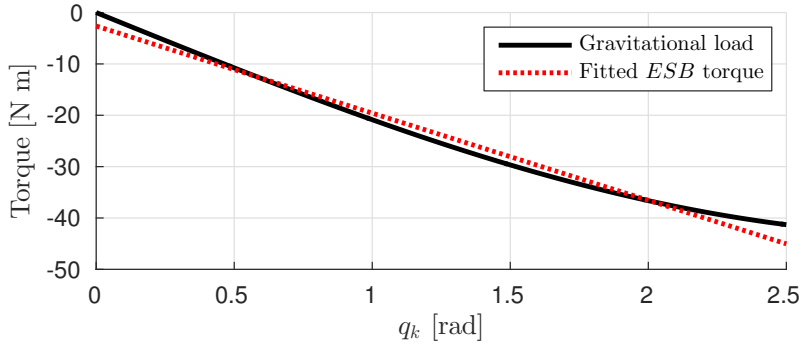

FIGURE 7.7: Fitted linear stiffness as a function of the knee angle q_k and gravitational load curve.

Given $\varphi_{1,opt}$ and $\varphi_{2,opt}$, then k_p and p can be parametrised with respect to the radius of the knee pulley:

$$k_p(r_k) = \frac{1}{r_k^2}\,\varphi_{2,opt} \quad , \quad p(r_k) = r_k\,\frac{\varphi_{1,opt}}{\varphi_{2,opt}}\,. \tag{7.14}$$

Fig. 7.8 shows the values of k_p and p required to optimally match the gravity load as a function of r_k. In the lower graph the maximum required deflection Δ_p of the elastic element is shown, which provides an indication of its total length requirements. Certainly this is a parameter that needs to be considered given the space limitations on the mechanical assembly. Using this as a guideline, the stiffness k_p and pretension p were selected for a radius of $r_k = 0.05$ m, resulting in a stiffness and pretension of (k_p, p) = (6.8 kN/m, 7.7x10^{-3} m). The selected physical element has a stiffness of 8.7 kN/m ($\pm$15% tolerance) in the linear range. The required deflection to cover the full range of motion of the knee joint is $\Delta_p = 0.125$ m which can be satisfied by the available space and mechanical constraints in this case.

7.3.2 Power Branch Stiffness

In tuning the stiffness of the Power Branch, we consider (7.1) and (7.9) and that the leg is in an equilibrium posture $q_k = q_k^e$. We first linearise the leg dynamics (7.1) around q_k^e to obtain

$$\ddot{\phi} = M(q_k^e)^{-1}\left[\tau_{leg} + \nabla G(q_k^e)\,\phi - d_k\,\dot{\phi}\right] \tag{7.15}$$

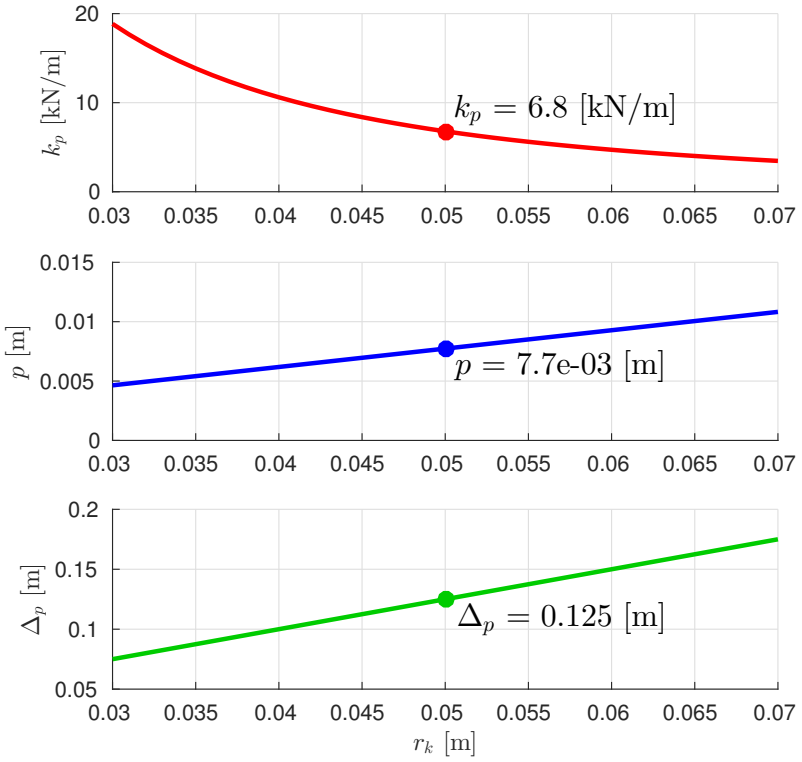

FIGURE 7.8: Optimal stiffness k_p and pretension position p required to compensate the gravity load as a function of the knee pulley radius r_k. The third graph shows the maximal required ESB elongation Δ_p as function of r_k.

where $\phi = q_k - q_k^e$ is the deviation from the equilibrium posture and the linearised gravitational torque $\nabla G(q_k^e) = \frac{\mathrm{d}}{\mathrm{d}q_k} G(q_k)|_{q_k=q_k^e}$. To linearise the actuator model we consider the ESB elastic element force (7.8) to be linear, such that (7.9) becomes a set of linear equations. Assuming that the generalized coordinates are slightly changing around the equilibrium configuration and their time derivatives are all small, then damping forces can be neglected. We then combine equations (7.9) and (7.15) to obtain the linear system, which is linearised at the equilibrium posture and written in state-space representation as:

$$\dot{\mathbf{Q}} = A(q_k^e)\mathbf{Q} + B\mathbf{u} \tag{7.16}$$

where $\mathbf{Q} = (\mathbf{q}, \phi)^T$. At the equilibrium, resonance frequencies of the system can be determined by calculating the eigenvalues of A. It is evident that the Power Branch stiffness has a large influence on the resonance frequencies and the overall dynamic response from the torque delivered by motor M1. Furthermore, the motor torque to

position response exhibits anti-resonant frequencies, which are determined by the transmission zeros of the system. It can be shown that these anti-resonant frequencies become the performance limiting factor in designing the closed-loop control system, since the anti-resonant frequencies are always below the resonant frequencies.

For the system described by (7.16), the transmission zero limiting the M1 performance is given by the roots of

$$M(q_k^e)\, s^2 + \nabla G(q_k^e) + k_p\, r_k^2 + k_{PB} = 0 \tag{7.17}$$

where s denotes the Laplace transform variable. Solving for s, we obtain the anti-resonant frequency f_{ar} as

$$f_{ar} = \frac{1}{2\pi}\sqrt{\frac{\nabla G(q_k^e) + k_p\, r_k^2 + k_{PB}}{M(q_k^e)}}\,. \tag{7.18}$$

From this result we can select the Power Branch stiffness k_{PB} to set the anti-resonant at a desired frequency following our trajectory and control bandwidths, e.g. $f_{ar} > \mu\, f_b$, where f_b is the desired bandwidth and μ is a scaling parameter. Solving (7.18) for k_{PB} results in the required value of the PB stiffness:

$$k_{PB} = (2\pi\, f_{ar})^2\, M(q_k^e) - \nabla G(q_k^e) - k_p\, r_k^2. \tag{7.19}$$

The resulting required PB stiffness for a given value of f_{ar} as a function of equilibrium configuration is shown in Fig 7.9.

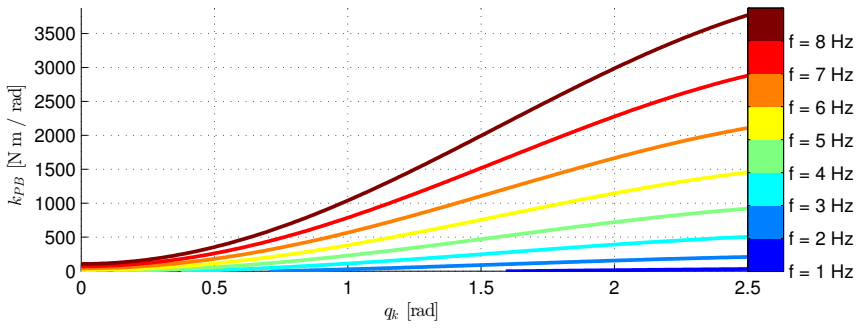

FIGURE 7.9: Required PB stiffness over knee angle for a targeted anti-resonance frequency f_{ar}.

In this work we consider a desired bandwidth of $f_b = 2$ Hz and set the anti-resonant at 4 Hz ($\mu = 2$), resulting in a minimum stiffness k_{PB} of approximately 918 N·m/rad for an additional load of 5 kg at the hip. The stiffness of the fabricated physical element is approximately 950 N·m/rad.

7.4 Control Strategy

The proposed control architecture to control the knee angle is shown in Fig. 7.10. An outer loop closes a position reference on the PB motor position using a PD controller with compensation term based on gravity. We choose to perform feedback in the PB using the motor rotor variable θ_1 instead of the knee angle to ensure that the closed system is asymptotically stable provided that the proportional and derivative gains are strictly positive (collocated control). Alternative feedback schemes using the link side variables would be possible but the selection of the proportional gain would be limited by the stiffness of the torsional transmission element to ensure stability.

The desired net torque τ^* on the knee is given by:

$$\tau^* = -G(q_k) + K_p \left[e_1 + K_d \, \dot{e}_1 \right] \tag{7.20}$$

where $e_1 = \theta_1^* - \theta_1$ and K_p and K_d denote the proportional and derivative gains respectively. The desired knee torque is split into two components, to be delivered by the Energy Storage Branch and Power Branch respectively. The pretension control system adjusts the pretension position to reach the ESB pretension required to achieve the desired ESB torque. Low-level control loops control M1 and M2 to obtain the desired motor torques τ_{PB}^* and τ_{M2}^*.

In the realised experimental setup, the low-level control is implemented on custom-built DSP-based motor controller boards running at 1 kHz: the controller monitors the deflection of the PB torsional transmission using the position encoders to obtain an estimate of the PB torque τ_{PB} using its known stiffness, and then uses PD control to calculate the M1 motor input. The pretension position p is controlled using PD

voltage control directly on the M2 motor position θ_2 to obtain $p \rightarrow p^*$. The remainder of this Section will elaborate on the torque distribution method and pretension control strategies.

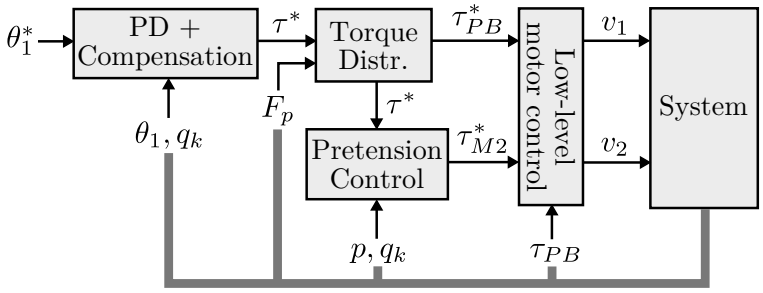

FIGURE 7.10: Control Architecture.

7.4.1 Motivation

Given a known pretension-torque relation for the ESB, it is straightforward to calculate the pretension position p that achieves a desired torque τ^*. However, the resulting pretension position is relative to the output link position q_k, corresponding to a certain elongation of the elastic element to generate the desired torque. Since there is unavoidable high-frequency motion of the output link, this would require high-frequency pretension position control to track a desired ESB torque exactly. However, this is not a desirable control strategy given the relatively low bandwidth and the high transmission ratio of the ESB actuation. We consider therefore a control strategy in which the ESB tracks the low-frequency components of the desired pretension position, and we use the high bandwidth of the PB to ensure the desired total torque τ^* is achieved at the output by the net torque from both ESB and PB contributions.

7.4.2 Torque Distribution

The upper part of Fig. 7.11 shows the distribution of the desired total torque τ^* into the desired PB torque and the desired ESB torque. The desired PB torque is calculated by subtracting the measured ESB torque τ_p from the total desired torque τ^*. We calculate the supplied ESB torque as $\tau_p = r_k\, F_p$, where F_p is the measurement

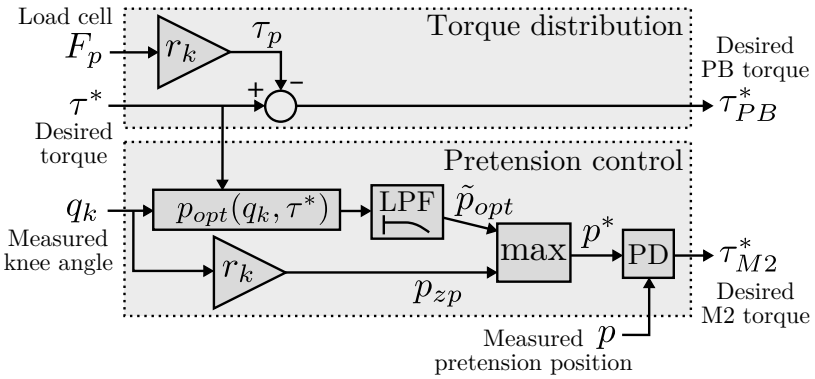

FIGURE 7.11: Reference torque distribution and pretension control.

of the load cell. In this way the high bandwidth of the Power Branch is used to ensure the desired net torque is achieved at the knee joint: $\tau_p + \tau^*_{PB} = \tau^*$.

7.4.3 Pretension Control

Recalling (7.12) and solving for p, we can calculate the optimal pretension position p_{opt} given a desired torque τ^* and output position q_k (lower part of Fig. 7.11):

$$p_{opt}(q_k, \tau^*) = r_k\, q_k + \eta_1\, \tau^* \tag{7.21}$$

where $\eta_1 = (r_k\, k_p)^{-1}$. However, as noted before, we choose to track only the low-frequency components. We write this as $\tilde{p}_{opt}$, where $\tilde{[.]}$ denotes low-pass filtering. The structure ensures that in steady state $\tilde{p}_{opt} \to p_{opt}$, such that $\tau_p \to \tau^*$, meaning the entire desired net torque is delivered by the ESB. The Low-Pass Filter (LPF) (LPF block in Fig. 7.11) is a first-order Butterworth filter with cut-off frequency of 0.03 Hz. Furthermore, to avoid slack in the compliant element PE due to lag resulting from the low-pass filtering, we calculate the zero pretension position (the position where $\Delta_p = 0$) as $p_{zp} = r_k\, q_k$, and define the pretension reference position p^* as

$$p^* = \max\left(\tilde{p}_{opt}, p_{zp}\right). \tag{7.22}$$

We then apply PD control on M2 to obtain $p \to p^*$ by controlling the M2 motor position θ_2.

7.5 Simulation Results

To analyse the effectiveness of the proposed design and control methods, we initially performed several simulation studies prior to experiments. For these simulations, the hip was loaded with an additional 5 kg of weight, simulating the weight of a small biped robot in two-legged squatting.

First we studied the comparative performance of a cyclic squatting motion for two cases: first using only the series-elastic Power Branch (i.e. ESB elastic elements disconnected), and second using both actuation branches. We compared the electrical motor power as a measure of energy efficiency, defined as $P_{Mj} = v_j\, i_j, j \in 1, 2$, where v_j denotes the voltage applied to motor j and i_j denotes the current through motor j as in Fig. 7.6. Finally, we also compared the electrical motor power as a function of squatting reference frequency, to show the energetic benefits for a wide reference frequency range.

Simulations were performed in MathWorks MATLAB R2013b Simulink with the ode45 variable-step solver with absolute and relative tolerances of 1e-8.

7.5.1 Cyclic Squatting Motion

In this simulation, a sinusoidal reference $q_1^*(t) = \alpha + \beta \sin(2\pi\, f\, t)$ with $\alpha = 1.3$ rad, $\beta = 0.5$ rad and $f = 0.5$ Hz is used for M1. The motion covers a relatively large range of the knee. We first consider the case in which the ESB is not used, and secondly the case in which both branches are engaged in the motion.

No ESB

Fig. 7.12a shows the tracking performance when the ESB elastic elements have been disconnected. As discussed in Sec. 7.4, the choice of using the motor-side variable θ_1 for feedback results in high control bandwidth and allows for high gains, such that the motor-side tracking error is smaller than 5e-3 rad. We find that due to this choice there exists a bias in the error between the M1 and knee angles, due to the

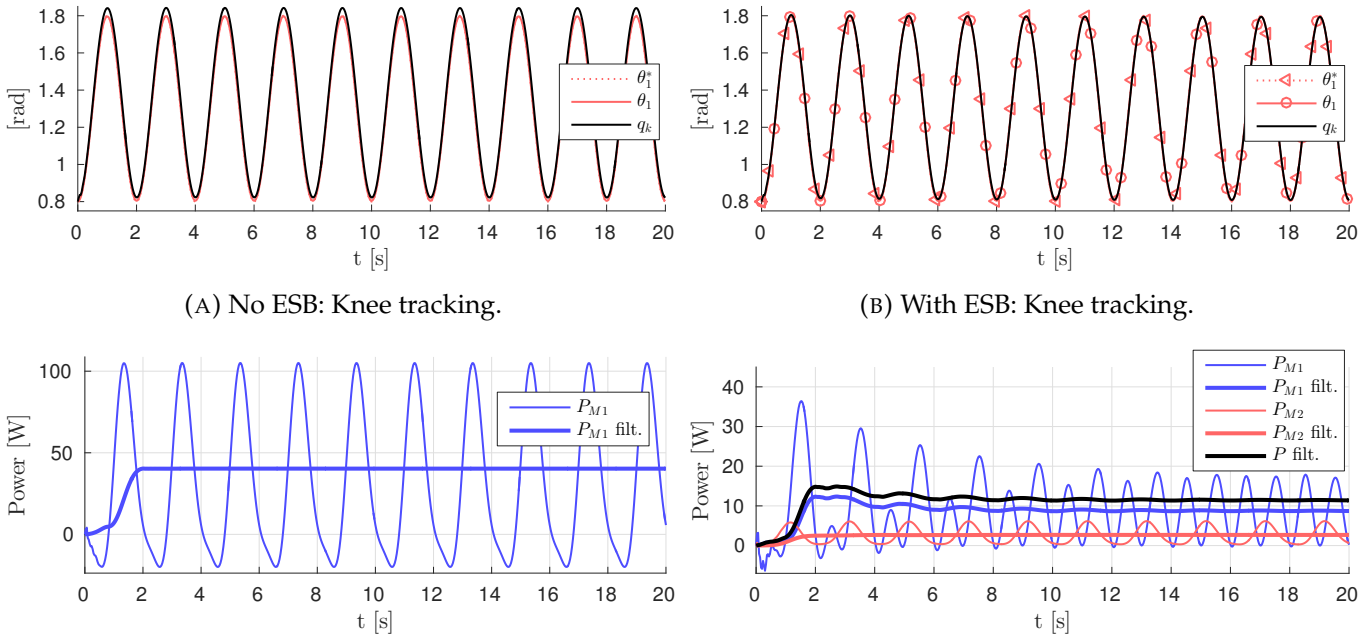

(A) No ESB: Knee tracking.

(B) With ESB: Knee tracking.

(C) No ESB: Motor power.

(D) With ESB: Motor power.

FIGURE 7.12: Simulation results for a cyclic squatting motion. The left column shows the results without ESB, the right with ESB. In all cases, the filtered (*filt.*) variables denote averages over the motion period ($1/0.5$ Hz = 2.0 s).

deflection of the elastic torsional transmission resulting from gravitational torque. However, since the worst-case anti-resonant was set at 4 Hz in Sec. 7.3, the element is sufficiently stiff, and the maximum joint-side error is smaller than 0.05 rad. Fig. 7.12c shows the electrical power consumption during this simulation. The average rectified power consumption over one cycle without ESB is 38.5 W.

With ESB

In this case both branches are engaged in performing the squatting motion. Fig. 7.12b shows the knee tracking performance. As the ESB starts compensating for the DC and low-frequency torque requirements of the motion, the gravitational torque on the torsional transmission element is significantly reduced. As a result, the bias in the error between the M1 angle and knee angle disappears, improving the tracking performance on the joint side with a maximum error smaller than 0.015 rad. With ESB, the average rectified power consumption over one cycle is 11.4 W.

A comparative analysis of the motor power (Fig. 7.12c, 7.12d) demonstrates that the

total power for executing this motion is reduced from 38.5 W (without ESB) to 11.4 W (with ESB), a reduction of ≈70%. With ESB, the total power rises initially, and then drops as the elastic element is pretensioned and starts delivering most of the desired knee torque.

Fig. 7.13 depicts the torque contributions of both branches at the knee joint, and the pretension position p and ESB elastic element elongation over time are shown in Fig. 7.14. We observe in these figures that as the pretension position converges, the ESB starts delivering most of the low-frequency torque requirements to perform the motion. Simultaneously, the mean PB torque τ_{PB} converges to zero. Together these effectively show that most of the DC and low-frequency torque demands are delivered by the ESB.

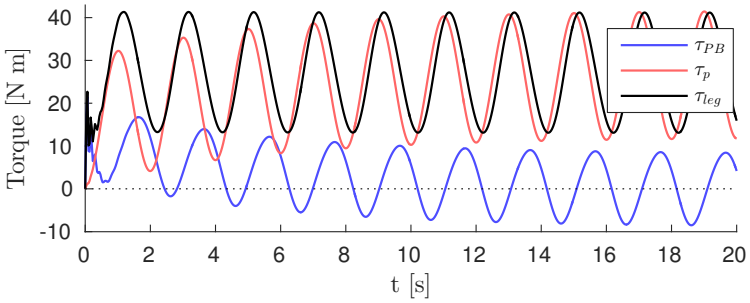

FIGURE 7.13: Torque contributions at the knee joint during cyclic squatting motion. τ_p denotes the ESB torque, τ_{PB} denotes the PB torque, and τ_{leg} denotes the total torque delivered at the knee joint.

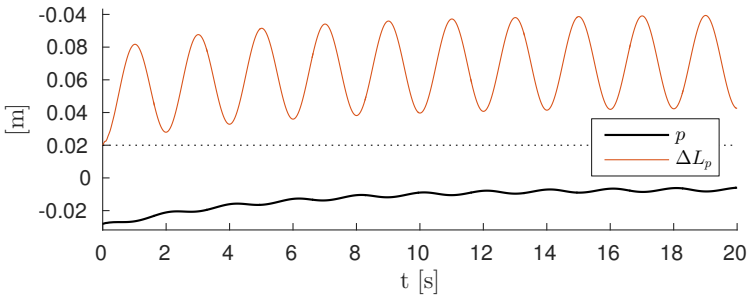

FIGURE 7.14: Pretension position p and ESB elastic element elongation Δ_p over time.

7.5.2 Power Consumption over Reference Frequency

In this simulation we consider the electrical motor power as a function of squatting reference frequency in the range from 0.1 to 1.0 Hz. The results are shown in Fig.

7.15, where again P_{M1} and P_{M2} denote the power of motors M1 and M2 respectively, and $P = P_{M1} + P_{M2}$ denotes the sum. $P_{M1,noESB}$ denotes the case in which the ESB elastic elements are disconnected, which means only M1 is used to generate the motion and deliver the required power.

We observe in Fig. 7.15 that for low frequencies the total motor power converges to very small values when using the ESB. This is due to two reasons: 1. at low frequencies the gravitational torque becomes dominant; 2. there is a close matching between ESB torque and gravitational torque as a function of knee angle. Together this ensures the ESB delivers nearly all required torque in an energy efficient way, as both motors are almost idle. Conversely, in the case where the ESB is not used, the motor power converges to ≈20 W for low frequencies, corresponding to the effort required to compensate for gravitational torque. These results illustrate that as the reference frequency decreases, the relative improvement in electrical energy efficiency due to the ESB becomes progressively larger.

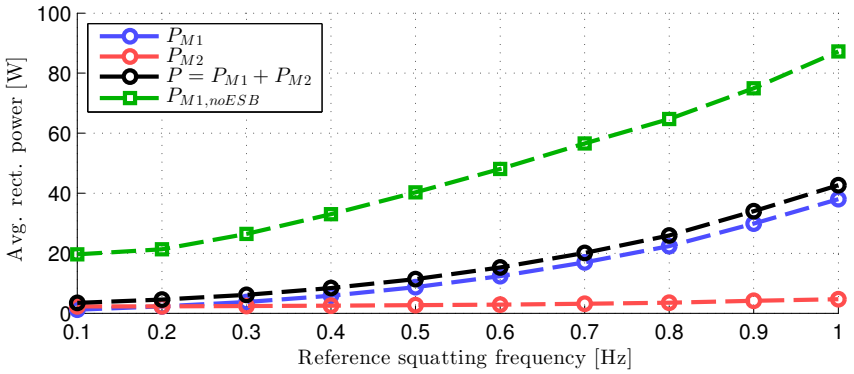

FIGURE 7.15: Simulation of electrical motor power over reference frequency. $P_{M1,noESB}$ denotes the case in which the ESB is not used, that is, only the PB motor M1 is used to perform the motion.

7.6 Experimental Results

Following the promising simulation results, we performed experiments on the leg prototype to validate the performance of the proposed design and control methods in practice. Similar to the simulation, two cases are evaluated in comparison: one is the case where ESB is not used at all by disconnecting the ESB elastic elements, and the other is the case where the ESB is engaged and controlled by the control scheme

presented in Sec. 7.4. We used the same cyclic squatting motion as in the simulation studies.

Note that during this squatting motion, the control strategy produces a smooth and varying reference for motor M2, therefore the unilateral clutch is not active. However, when the system is powered down, the non-backdrivable mechanism self-locks and ensures that the pretension position is fixed.

This Section first elaborates the characterisation of the torque delivered by the ESB elastic elements in the experimental setup, and then presents the experimental results for both cases.

7.6.1 ESB Tension to Torque Characterisation

In our model we assume a linear spring force generated by the elastic elements of the ESB. However, the spring force generated by the physical elastic elements is non-linear in practice. Hence, the tension to torque relationship has to be characterised for optimal performance. We characterised the elements by a mapping from the ESB extension Δ_p to ESB knee torque τ_p. The leg was kept in an equilibrium position $q_k = \alpha = 1.3$ rad (the mean of our reference motion) and we varied the pretension p to obtain measurement sets (Δ_p, τ_p). From our measurements we found no significant hysteresis for the used type of elastic cords. While the presence of hysteresis in the cords would result in the ESB not exactly delivering its desired torque, the use of a load cell for direct measurement of the delivered torque ensures that the net desired torque is always achieved at the joint: The desired PB torque is calculated by subtracting the measured ESB torque from the net desired torque (Sec. 7.4.2).

After obtaining a set of measured (Δ_p, τ_p) over a large range of Δ_p, we inverted the relationship, interpolated the data into evenly spaced data points, and fit a polynomial function ψ to obtain the relationship $\Delta_p^* = \psi(\tau^*)$, which maps a desired ESB torque to a desired elastic element elongation. The optimal pretension position p_{opt} in (7.21) is then instead given by

$$p_{opt}(q_k, \tau^*) = r_k\, q_k + \psi(\tau^*). \tag{7.23}$$

The results are shown in Fig. 7.16. As expected based on material properties, the spring force increases rapidly for small elongations, and then increases more slowly afterwards. This is in line with information provided by the manufacturer.

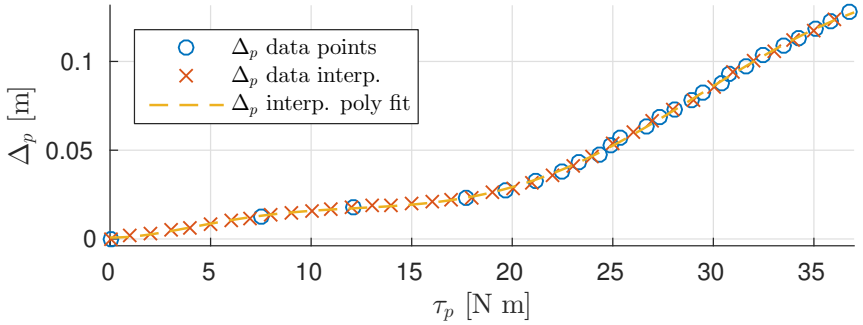

FIGURE 7.16: Characterisation of ESB torque and elastic elongation.

7.6.2 Experimental Results

Snapshots of one motion cycle of the experiment are shown in Fig. 7.17. The experimental results are shown in Fig. 7.18, where results without ESB are located on the left and the corresponding plots with ESB are shown on the right. The thick lines (*filt.*) in Fig. 7.18e–7.18j denote the powers and torques averaged over the motion period of 2.0 s.

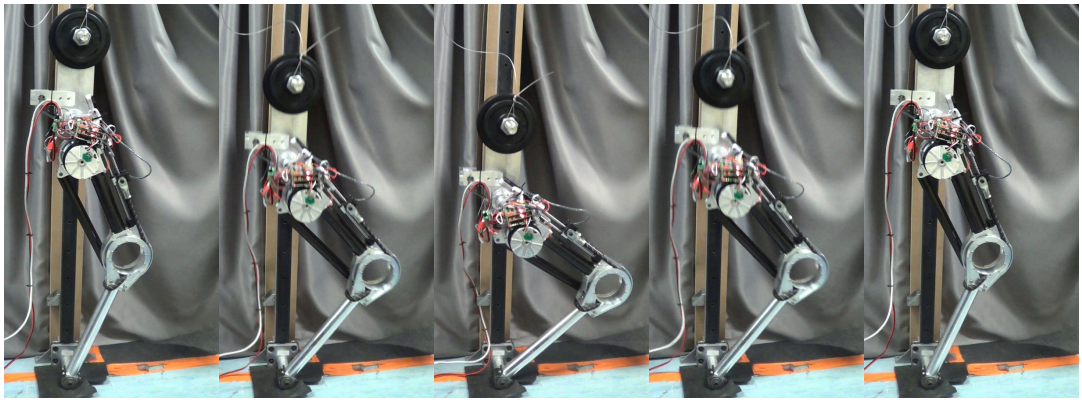

FIGURE 7.17: Experiment snapshots showing one motion cycle.

Comparing Fig. 7.18c to 7.18d, we observe that as the pretension position converges and ESB elastic element is tensioned, the ESB starts delivering most of the required torque. At the same time, the PB torque converges to zero mean, keeping the mean net torque approximately constant. This implies that the ESB is delivering the DC torque requirements. This is confirmed by the cycle average torque of drive M1 (Fig.

7.18j) which gradually approaches zero. Hence, our proposed control strategy is effective, significantly improving electrical energy efficiency.

The efficiency of the drive M1 itself, i.e. the ratio of conversion of electrical to mechanical power, is ≈53% in the first case, and reduces to ≈38% when the ESB is used. This is attributed to the relatively larger contribution of the back-EMF and internal mechanical friction in the drive, as the same motion is executed but smaller torque is delivered. The lower torque requirement also reduces the demand on the power supply: after convergence the peak electrical power generated during the motion is reduced from >170 W to <50 W. Hence, on robotic systems using the proposed mechanical structure, both motors and power supply can be dimensioned differently, reducing system costs and weight while obtaining increased energy efficiency.

Table 7.1 summarizes the power consumption results shown in Fig. 7.18e–7.18h. The electrical power of the complete system without ESB (Fig. 7.18e) is ≈54 W, with all power delivered by the high power PB drive M1. In the case when both actuation branches are used (Fig. 7.18f), the total electrical power is ≈19 W. This results in an electrical power reduction of ≈65%, which is in agreement with the results obtained in simulation.

	No ESB	**With ESB**
M1 electrical power [W]	54.0	14.3
M2 electrical power [W]	–	4.5
Total electrical power [W]	**54.0**	**18.8** ↓
M1 mechanical power [W]	28.5	5.5
M1 efficiency [%]	53	38

TABLE 7.1: Summary of experimental results.

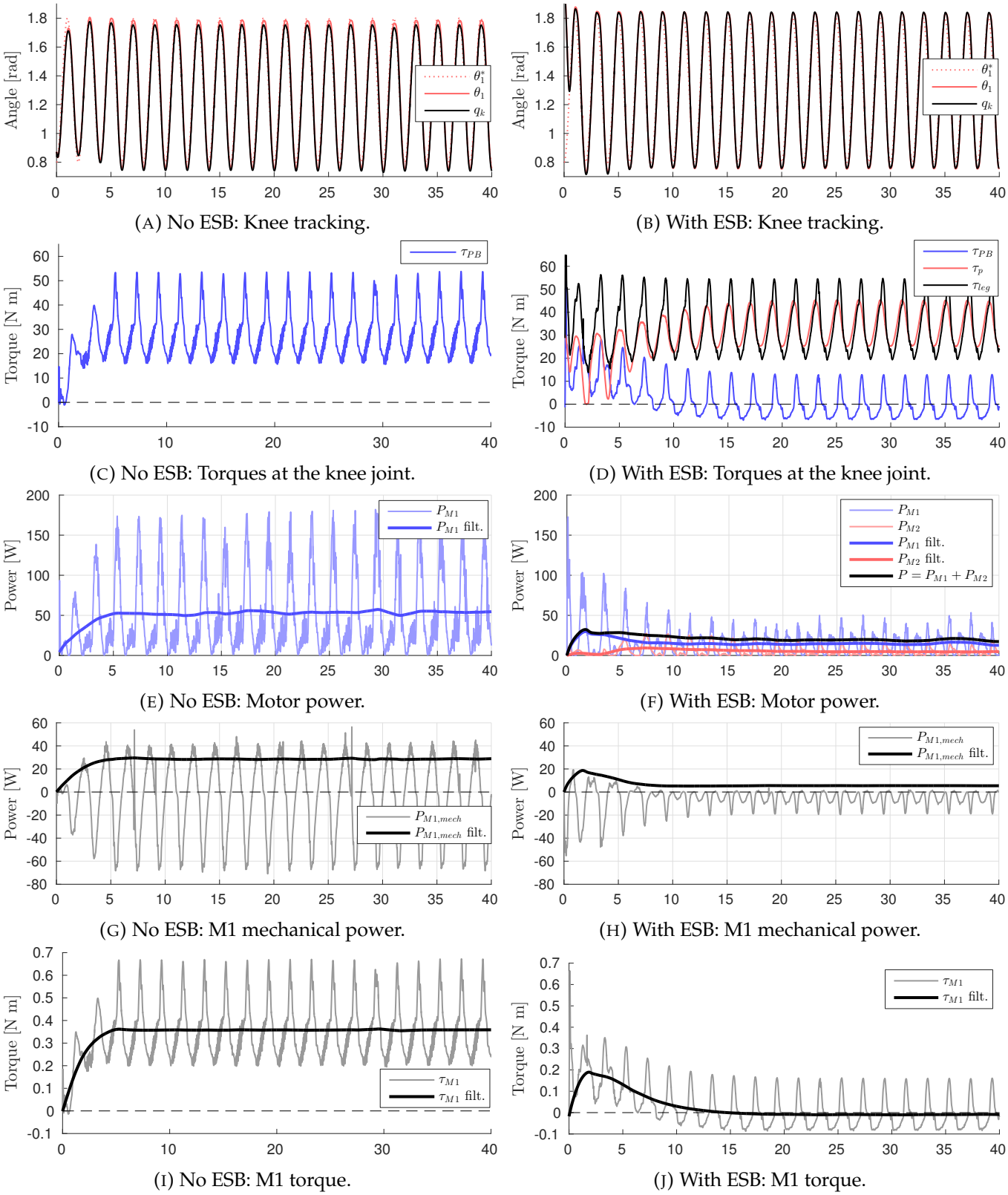

(A) No ESB: Knee tracking.

(B) With ESB: Knee tracking.

(C) No ESB: Torques at the knee joint.

(D) With ESB: Torques at the knee joint.

(E) No ESB: Motor power.

(F) With ESB: Motor power.

(G) No ESB: M1 mechanical power.

(H) With ESB: M1 mechanical power.

(I) No ESB: M1 torque.

(J) With ESB: M1 torque.

FIGURE 7.18: Experimental results. The left column shows results without ESB, the right with ESB. In all cases, the filtered (*filt.*) variables denote averages over the motion period ($1/0.5$ Hz = 2.0 s).

7.7 Conclusions

The modelling and control of a novel compliant joint of asymmetric compliant design for energy efficient motion generation was presented in this Chapter, and its effectiveness is demonstrated in both simulation and experimental studies. The novel asymmetric design consists of two antagonistic branches driving a single joint: a high power branch based on Series-Elastic Actuation designated as the Power Branch, and a highly energy efficient branch with large elastic energy storage capacity, designated as the Energy Storage Branch.

As a proof of concept, a 1-DoF knee-actuated hopping robot was used and the effectiveness was successfully validated. Both leg and actuator were thoroughly modelled, taking into account the electrical dynamics of the motors. The stiffness of both branches was selected using appropriate guidelines based on control bandwidth requirements and gravitational load compensation for improved energy efficiency.

Exploiting the full potential of this unique hardware was challenging and interesting. Our novel control strategy was developed for actively employing both branches of this novel hardware to efficiently drive the joint, by distributing the required effort to perform the motion among both branches. We utilised the Energy Storage Branch to deliver the low-frequency components of the desired torque, and exploited the high bandwidth of the Power Branch to ensure that the desired net torque was achieved at the joint.

The electrical energy efficiency benefits of the concept were proven by simulation and experiment. Noticeably, the experimental results show a significant reduction in electrical power consumption of 65%. Given these very promising results, we believe this interesting actuation concept can contribute to higher performance robotic systems in terms of energy efficiency and peak power output.

8

Generalisations and Biarticulation for Articulated Robots

This Chapter presents the generalisation of the design and control concepts of the asymmetric compliant actuation concept introduced in Chapter 7, as well as its extension to multi-DoF articulated robotic systems. Biarticulated structures are introduced, which enable more design freedom and have the unique ability of transferring mechanical power between joints. The Chapter studies and presents a novel method to select the design parameters of asymmetric compliant actuation schemes, to improve the energy efficiency of multi-DoF articulated robots powered by this type of actuator. An optimisation problem is formulated to optimise the actuation design parameters for energy efficient operation. Simulation studies performed on a 2-DoF leg as proof-of-concept report significant improvements in electrical energy

efficiency and reduction in peak torque and electrical power requirements. Furthermore, the biarticulated actuation arrangement is shown to further enhance the energy efficiency of the robotic leg.

The Chapter is structured as follows. Sec. 8.1 introduces the concept of biarticulated actuation structures. Sec. 8.2 describes the 2-DoF proof-of-concept leg model used to illustrate the effectiveness of our methods, as well as the model formulation of both leg and actuation. Sec. 8.3 discusses the methods used for optimisation of the actuation design parameters for general multi-DoF systems, actuated by an arbitrary combination of mono- and biarticulated actuators. Sec. 8.4 presents the control architecture for multi-DoF systems. A simulation study is presented and data are analysed in Sec. 8.5, followed by conclusions in Sec. 8.6.

8.1 Biarticulated Actuation Structures

In contrast to most existing robots, humans utilise biarticulated muscle structures that actuate multiple joints with a single muscle. Examples include the hamstrings, which span both the hip and knee joints, and the gastrocnemius muscle that spans both the knee and ankle joints. Fig. 8.1 shows the actuation concept in biarticulated configuration. The PB drives the joint directly, but the ESB tendon spans the right joint via a free pulley and then drives the left joint.

As a result, the extension of elastic element PE is dependent on the configuration of both joints, and the tendon produces a torque on both joints. Selection of the pulley radii ratio and stiffness value allows to shape the torque profile as a function of both joint configurations and pretension value.

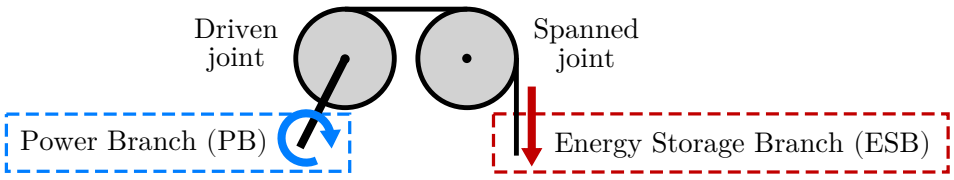

FIGURE 8.1: Actuation concept - Biarticulated configuration.

As a proof-of-concept to demonstrate the effectiveness of our methods, we consider a 2-DoF leg model with properties similar to the 1-DoF prototype considered in

Chapter 7. Both DoFs are actuated and experience viscous friction. We consider the foot to be in good contact, so that it can be considered fixed. We elaborate on this leg model in the next Section.

8.2 Dynamics Modelling

In the following, we opted for a modular modelling approach, for simulation purposes: this allows to quickly test a variety of actuation arrangements.

8.2.1 Leg Modelling

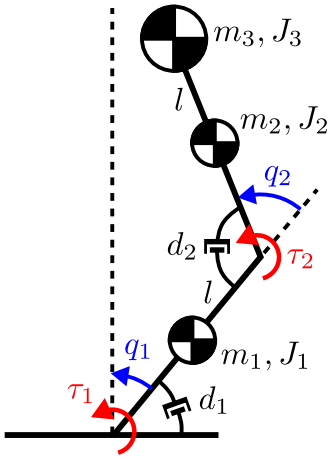

FIGURE 8.2: 2-DoF leg model.

The leg model (Fig. 8.2) consists of two links of length l, mass m_1, m_2, and rotational inertiae J_1, J_2, connected by an actuated knee joint. On the hip there is a load mass m_3 with rotational inertia J_3. The lower link pivots around the ground contact through the actuated ankle joint, resulting in a 2-DoF system with 2 inputs. Both joints are damped by viscous friction with coefficients d_1, d_2. The dynamics of this model are described by

$$\ddot{\mathbf{q}} = M(\mathbf{q})^{-1} \left[\boldsymbol{\tau} + \mathbf{G}(\mathbf{q}) - D\dot{\mathbf{q}} \right] \tag{8.1}$$

where $[q_1, q_2]^T =: \mathbf{q} \in \mathcal{Q} \subseteq \Re^2$ denotes the configuration variables as in Fig. 8.2, $\boldsymbol{\tau} \in \Re^2$ denotes the actuator torques, the damping matrix $D = \mathrm{diag}(d_1, d_2)$ denotes

joint friction, and $\mathbf{G}(\mathbf{q}) \in \Re^2$ denotes the generalised gravitational torque:

$$\mathbf{G}(\mathbf{q}) = J(\mathbf{q})^T \mathbf{G}_c \tag{8.2}$$

where $J(\mathbf{q})$ denotes the system Jacobian and the gravitation vector $\mathbf{G}_c$ is given by

$$\mathbf{G}_c = [0, -m_1 g, 0, 0, -m_2 g, 0, 0, -m_3 g, 0]^T \tag{8.3}$$

and $g = 9.81$ m/s^2. In all notation, $\dot{[.]}$ denotes the time derivative and $[.]^T$ denotes the transpose. We ignore the centripetal and Coriolis forces. The generalised inertia matrix $M(\mathbf{q}) \in \Re^{N \times N}$ is given by

$$M(\mathbf{q}) = J^T(\mathbf{q}) M_c J(\mathbf{q}) \tag{8.4}$$

with the nominal inertia matrix M_c defined as

$$M_c = \text{diag}\left(m_1, m_1, J_1, m_2, m_2, J_2, m_3, m_3, J_3\right). \tag{8.5}$$

8.2.2 Biarticulated Configurations

In Chapter 7, the actuator modelling for monoarticulated configurations was presented for the 1-DoF prototype considered there. In this section, we extend the modelling to biarticulated configurations, for which the abbreviated actuator model is shown in Fig. 8.3. Here joint i is driven and the ESB tendon spans joint j. In this case, the elongation of the ESB elastic element is given by both joints:

$$\Delta L_p = p - r_{b,i} q_i - r_{b,j} q_j \tag{8.6}$$

and the tendon generates torque on both joints. Compared to the monoarticulated formulation in Chapter 7, the input vector (7.11) now becomes $\mathbf{u} = [v_1, v_2, \dot{\mathbf{q}}_b]^T$, where $\dot{\mathbf{q}}_b = [\dot{q}_i, \dot{q}_j]^T$ denotes the vector of joint velocities. The net joint torques in

biarticulated configuration are given by:

$$\tau_i = \tau_{b,i} + \tau_{PB,i}$$
$$\tau_j = \tau_{b,j} \tag{8.7}$$

where the ESB torques are $\tau_{b,i} = r_{b,i}F_p$ and $\tau_{b,j} = r_{b,j}F_p$, and $\tau_{PB,i}$ denotes the PB torque on the driven joint i.

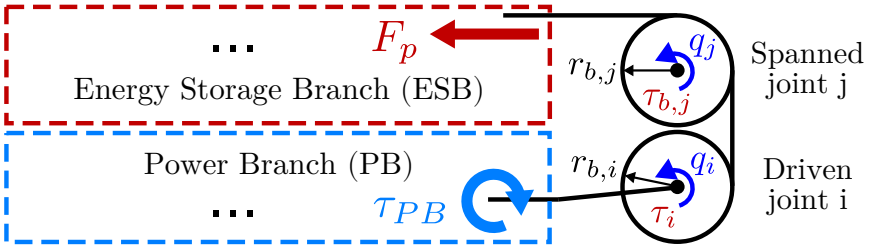

FIGURE 8.3: Actuator model - Biarticulated configuration driving joint i with the ESB tendon spanning joint j.

8.3 Optimisation of Design Parameters

This section introduces an optimisation method to select the design parameters of the Energy Storage Branches. Based on the gravitational load, stiffness, and inertial properties, the actuation parameters can be chosen such that the ESBs provide maximum load compensation for higher energy efficiency and reduction of peak torque/power requirements.

By considering pulley radii, elastic element stiffnesses and pretension positions, we introduce an optimisation procedure that maximises compensation torque provided by the ESBs over the N-DoF workspace. We first describe a reduction of the number of parameters for the mono- and biarticulated actuation cases. Next we elaborate on the actuation configurations and introduce optimisation problem. This section concludes with results for the leg actuation configurations.

8.3.1 Monoarticulated Joints

Assuming low velocity movements of the leg, the damping of the elastic element PE can be neglected and its torque written in the following linear form for the monoarticulated case:

$$\tau_m = \varphi_1 + \varphi_2 q \tag{8.8}$$

where τ_m denotes monoarticulated ESB torque and $\varphi_1 = -rk_p p$ and $\varphi_2 = -r^2 k_p$. Given optimal values $\varphi_{1,opt}$ and $\varphi_{2,opt}$, then k_p and p can be parametrised with respect to a chosen pulley radius r:

$$k_p(r) = \frac{\varphi_{2,opt}}{r^2}, \qquad p(r) = r\frac{\varphi_{1,opt}}{\varphi_{2,opt}}. \tag{8.9}$$

Hence, the number of parameters for this monoarticulated ESB is reduced from 3 to 2.

8.3.2 Biarticulated Joints

Similarly to the monoarticulated case, the biarticulated ESB torque $\tau_{b,i}, \tau_{b,j}$ generated on joints i and j (Fig. 8.3) can be written as

$$\begin{aligned} \tau_{b,i} &= \varphi_3\varphi_5 - \varphi_3^2 q_i - \varphi_3\varphi_4 q_j, \\ \tau_{b,j} &= \varphi_4\varphi_5 - \varphi_3\varphi_4 q_i - \varphi_4^2 q_j, \end{aligned} \tag{8.10}$$

where $\varphi_3 = \sqrt{k_p} r_{b,i}$, $\varphi_4 = \sqrt{k_p} r_{b,j}$, and $\varphi_5 = \sqrt{k_p} p$. Given optimal values $\varphi_{1,opt}$, $\varphi_{2,opt}$ and $\varphi_{3,opt}$, then $r_{b,j}$, k_p and p can be parametrised with respect to a chosen value of the driven joint pulley radius $r_{b,i}$:

$$\begin{aligned} k_p(r_{b,i}) &= \left(\frac{\varphi_{3,opt}}{r_{b,i}}\right)^2, \qquad r_{b,j}(r_{b,i}) = \frac{\varphi_{4,opt}}{\sqrt{k_p}}, \\ p(r_{b,i}) &= \frac{\varphi_{5,opt}}{\sqrt{k_p}}. \end{aligned} \tag{8.11}$$

Similarly, the number of parameters of the biarticulated ESB is reduced from 4 to 3.

8.3.3 2-DoF Leg Actuation Configurations

We consider three actuator configurations for the 2-DoF leg, shown in Fig. 8.4. In Fig. 8.4a, we consider both joints to be actuated by only the Power Branch, i.e. with the ESB removed, resulting in a conventional SEA system.

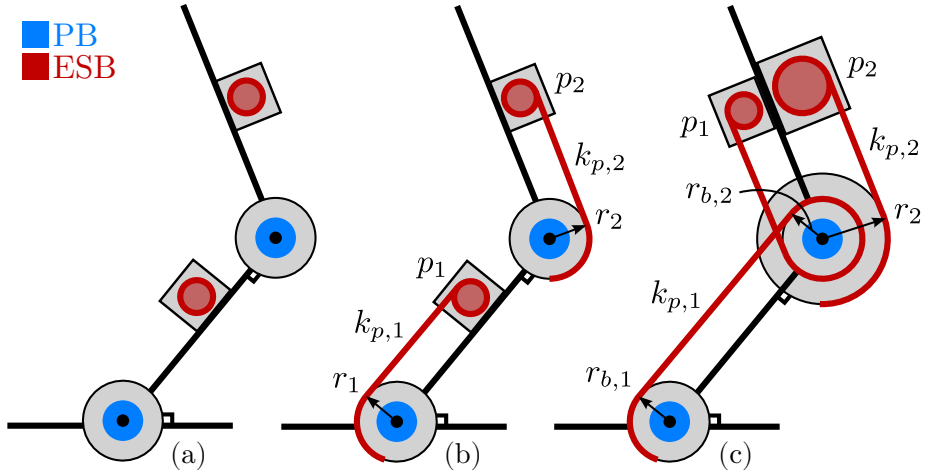

FIGURE 8.4: Leg actuation configurations: SEA (a), mono- (b) and biarticulated (c). In (b), ankle and knee are monoarticulated. In (c), the biarticulated ESB spans the knee and ankle joints.

Shown in Fig. 8.4b is the second configuration, in which both joints are driven by a PB and a monoarticulated ESB. The ESB torques $\boldsymbol{\tau}_p = [\tau_{p,1}, \tau_{p,2}]^T$ on the joints are given by

$$\begin{bmatrix} \tau_{p,1} \\ \tau_{p,2} \end{bmatrix} = \begin{bmatrix} \tau_{m,1} \\ \tau_{m,2} \end{bmatrix}. \tag{8.12}$$

For this configuration, there are 6 parameters for the ESB branches: the pulley radii r_1, r_2, stiffnesses $k_{p,1}, k_{p,2}$, and pretension positions p_1, p_2. Following Sec. 8.3.1, these can be rewritten into 4 parameters as $\boldsymbol{\varphi} = [\varphi_1, \varphi_2, \varphi_3, \varphi_4]$ where φ_1, φ_2 describe the ankle ESB and φ_3, φ_4 describe the knee ESB.

Shown in Fig. 8.4c is the third configuration, in which the knee joint is actuated by a PB and a monoarticulated ESB, and the ankle is actuated by a PB and a biarticulated ESB which spans both the knee and ankle joint, as in Fig. 8.3. This configuration is equal to the gastrocnemius muscle in humans, which connects the hip bone to the heel bone, spanning both the knee and ankle joints. This configuration was chosen because it allows a power transfer from knee extension to foot push-off, thus aiding

in squatting motions and providing increased foot push-off power during walking, running and jumping. The ESB torques are given by

$$\begin{bmatrix} \tau_{p,1} \\ \tau_{p,2} \end{bmatrix} = \begin{bmatrix} \tau_{b,1} \\ \tau_{b,2} \end{bmatrix} + \begin{bmatrix} 0 \\ \tau_m \end{bmatrix}. \tag{8.13}$$

Due to the additional free pulley required for spanning the knee joint, there are 7 ESB parameters in this configuration: the pulley radii $r_{b,1}, r_{b,2}, r_2$, stiffnesses $k_{p,1}, k_{p,2}$ and pretension positions p_1, p_2. Using Sec. 8.3.1 and 8.3.2, these can be rewritten into 5 parameters as $\boldsymbol{\varphi} = [\varphi_1, \varphi_2, \varphi_3, \varphi_4, \varphi_5]$ where $\varphi_1, \varphi_2, \varphi_3$ describe the biarticulated ESB and φ_4, φ_5 describe the monoarticulated ESB.

The conventional SEA configuration does not require any ESB parameters. In the other two cases, we would like to find the value of $\boldsymbol{\varphi}$ that minimises the error between the ESB torques and some desired torque functions over a subset of the workspace of the leg. In the next section, we proceed to formulate this optimisation problem.

8.3.4 Optimisation Problem

To optimise the ESB parameter vector $\boldsymbol{\varphi}$, we first define the error vector $\mathbf{e}(\mathbf{q}) \in \Re^N$ for N joints as

$$\mathbf{e} = \boldsymbol{\zeta}(\mathbf{q}) + \boldsymbol{\tau}_p(\mathbf{q}) \tag{8.14}$$

where $\boldsymbol{\tau}_p(\mathbf{q})$ denotes the ESB torques on the joints, which can be composed of an arbitrary mono- or biarticulated configuration. For simplicity, we consider the system to be fully actuated. The function $\boldsymbol{\zeta}(\mathbf{q})$ denotes the vector of desired torques. Here we shall consider static gravitational joint torque compensation: $\boldsymbol{\zeta}(\mathbf{q}) = \mathbf{G}(\mathbf{q})$. For highly dynamic behaviour known at design time, $\boldsymbol{\zeta}$ may include inertial and damping components for efficient execution of those motions. Some authors have performed design optimisation to increase energy efficiency for systems with pre-planned trajectories (e.g. [43]). However, we consider general-purpose systems for which the desired motions are not known at design time.

The total error $E(\boldsymbol{\varphi}) \in \Re$ is defined as the integrated l^2-norm over a subset of the workspace:

$$E(\boldsymbol{\varphi}) = \int_{\mathbf{q} \in \mathcal{Q}_d} \|\lambda\, \mathbf{e}(\mathbf{q}, \boldsymbol{\varphi})\|_2 \, \mathrm{d}\mathbf{q}, \tag{8.15}$$

where $\lambda \in \Re^{N \times N}$ is a diagonal matrix that allows to weigh some joints more than others (here $\lambda = I$), and $\mathcal{Q}_d \subset \mathcal{Q}$ is a subset of the joint workspace on which to optimise and depends on the specific robot. Using the l^2-norm approximates minimising the electrical power consumption directly, as the electrical power of a Brush-Less Direct Current (BLDC) motor can be approximated (neglecting electrical dynamics) by its squared torque. An optimal solution $\boldsymbol{\varphi}_{opt}$ minimises E:

$$\begin{aligned} \boldsymbol{\varphi}_{opt} &= \min_{\boldsymbol{\varphi}} \; E(\boldsymbol{\varphi}) \\ \text{s.t.} \quad & \underline{\boldsymbol{\varphi}} \leq \boldsymbol{\varphi} \leq \overline{\boldsymbol{\varphi}} \end{aligned} \tag{8.16}$$

where $\underline{\boldsymbol{\varphi}}$ and $\overline{\boldsymbol{\varphi}}$ denote the lower and upper bounds of $\boldsymbol{\varphi}$ respectively. Note that due to the redundancy in the original parameters, the choice of the free parameters should be such that the bounds on the original parameters are not violated.

For the cases in Sec. 8.3.3, the globally optimal value can be easily found by choosing realistic initial values and standard optimisation algorithms. However, due to the two (monoarticulated) or three (biarticulated) parameters corresponding to each actuated joint, we have $\dim(\boldsymbol{\varphi}) \geq 2N$ for N joints. Thus, when N becomes large, solving for $\boldsymbol{\varphi}_{opt}$ by minimising (8.15) becomes infeasible. However, realising that each parameter affects only one or two (in the biarticulated case) joints, the problem can be partitioned into multiple smaller optimisation problems which are solved for a partition of the complete parameter vector. In the following section we shall discuss the partitioned case.

8.3.5 Partitioning

Let $\mathbf{e}^c \subset \mathbf{e}$ denote the subset of errors and $\boldsymbol{\varphi}^c \subset \boldsymbol{\varphi}$ the corresponding parameters of the joints belonging to the partition, where the superscript $[.]^c$ denotes the partitioning. We then define the error for the partition similarly to (8.15):

$$E^c(\boldsymbol{\varphi}^c) = \int_{\mathbf{q} \in \mathcal{Q}_d} \|\lambda^c \, \mathbf{e}^c(\mathbf{q}, \boldsymbol{\varphi}^c)\|_2 \, \mathrm{d}\mathbf{q}. \tag{8.17}$$

Note we are still required to integrate over $\forall \mathbf{q} \in \mathcal{Q}_d$, as even though the actuation is decoupled, the joint load still depends on the configuration of all joints. The parameters in the partition can then be optimised by minimising E^c:

$$\begin{aligned} \boldsymbol{\varphi}^c_{opt} &= \min_{\boldsymbol{\varphi}^c} \; E^c(\boldsymbol{\varphi}^c) \\ \text{s.t.} \quad & \underline{\boldsymbol{\varphi}}^c \leq \boldsymbol{\varphi}^c \leq \overline{\boldsymbol{\varphi}}^c \end{aligned} \tag{8.18}$$

where $\underline{\boldsymbol{\varphi}}^c$ and $\overline{\boldsymbol{\varphi}}^c$ denote the lower and upper bounds of the partitioned parameters $\boldsymbol{\varphi}^c$ respectively.

For the monoarticulated case (shown in Fig. 8.4b) the problem can be partitioned as $\boldsymbol{\varphi}^c_1 = [\varphi_1, \varphi_2]$ and $\boldsymbol{\varphi}^c_2 = [\varphi_3, \varphi_4]$, i.e. the parameters of each joint can be optimised separately, reducing the problem to two independent one-dimensional line fitting problems. Hence, using appropriate partitioning, the parameters for structures with many joints can be optimised.

8.3.6 2-DoF Leg Parameters

To select the actuation parameters, we consider that the hip is loaded with an additional 40 kg of weight, simulating the weight of a humanoid robot standing on both legs. To obtain the optimisation workspace $\mathcal{Q}_d$, we define a mapping from polar coordinates of the hip to the joint variables as $\Gamma : (\beta, r) \rightarrow \mathbf{q}$, where β, r denote the polar angle and radius, chosen $-0.4 \leq \beta \leq 0.2$ and $l \leq r \leq 2l$ (Fig. 8.5), thereby covering the entire feasible workspace of the hip above the stance foot. The optimal parameters are listed in Table 8.1.

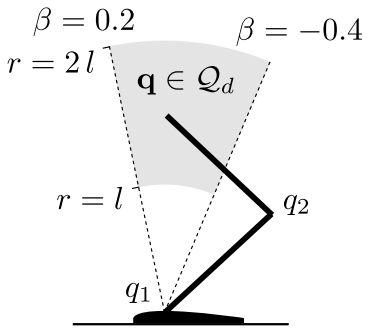

FIGURE 8.5: The workspace subset $\mathcal{Q}_d$ on which the ESB actuation parameters are optimised.

Monoart.	**Value**	**Biart.**	**Value**
r_1, r_2	0.060 m (chosen)	$r_{b,1}, r_2$	0.060 m (chosen)
		$r_{b,2}$	0.035 m
$k_{p,1}$	7.69 kN/m	$k_{p,1}$	69.4 kN/m
$k_{p,2}$	16.4 kN/m	$k_{p,2}$	14.7 kN/m

TABLE 8.1: Optimal ESB parameters for 2-DoF leg.

8.4 Control Strategy

The proposed architecture to control the joint variables is shown in Fig. 8.6. An outer loop tracks position references on the joint variables $\mathbf{q}$ using a PD controller with gravity compensation. The resulting desired joint torques $\boldsymbol{\tau}^*$ are given by:

$$\boldsymbol{\tau}^* = -\mathbf{G}(\mathbf{q}) + K_q \left[\mathbf{e}_q + D_q \dot{\mathbf{e}}_q\right] \tag{8.19}$$

where $\mathbf{e}_q = \mathbf{q}^* - \mathbf{q} \in \Re^N$ denotes the joint variable errors, $\mathbf{G}$ again denotes the gravitational torques and $K_q, D_q \in \Re^{N \times N}$ denote diagonal control gain matrices. The actuator control, presented next, is designed to be agnostic with respect to the outer control loop. For example, the desired joint torques can also result from advanced whole-body control schemes. Indeed, the actuator control simply tracks the desired joint torques in an energy efficient manner.

In the actuator control strategy, the desired joint torques $\boldsymbol{\tau}^*$ are distributed among the PB and ESB controllers, as shown top left in green in Fig. 8.7:

- The desired PB torques are calculated by subtracting the measured ESB torques from the desired joint torques: $\boldsymbol{\tau}^*_{PB} = \boldsymbol{\tau}^* - \boldsymbol{\tau}_p$.
- The desired ESB torques are calculated in terms of torque generated on the

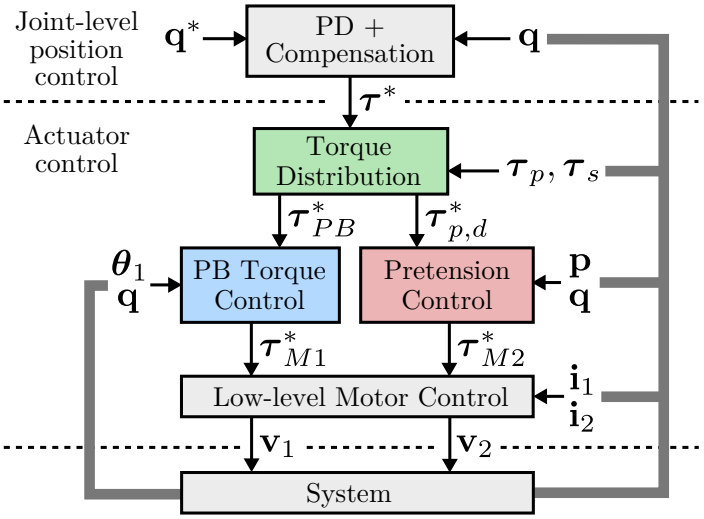

FIGURE 8.6: Control Architecture.

driven joints as $\boldsymbol{\tau}^*_{p,d}$. We first define $\boldsymbol{\tau}_s$, consisting of the measured torques on spanned joints from biarticulated ESBs (e.g. the torque on the knee by the biarticulated ESB in Fig. 8.4c, where $\boldsymbol{\tau}_s = [0, \tau_{b,2}]^T$). We then obtain the desired ESB torques as $\boldsymbol{\tau}^*_{p,d} = \boldsymbol{\tau}^* - \boldsymbol{\tau}_s$.

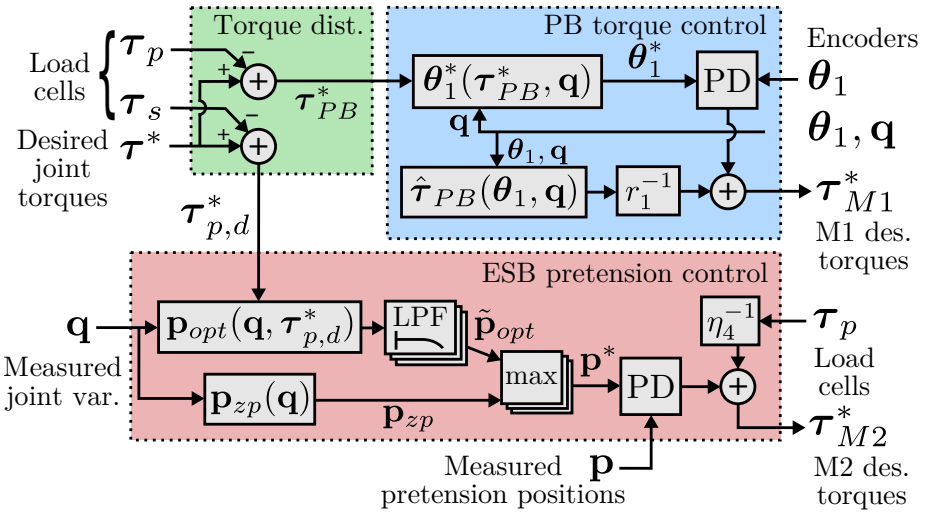

FIGURE 8.7: Reference torque distribution (green), PB torque control (blue) and ESB pretension control (red).

Given the pretension-torque relations for the ESBs, it is straightforward to calculate pretension positions $\mathbf{p}$ that achieve desired joint ESB torques. However, the resulting pretension positions depend linearly on the joint positions $\mathbf{q}$, corresponding to a certain elongation of the elastic elements. Since there is unavoidable high-frequency behaviour in the joint variables, this would require high-frequency pretension position control to track the desired torques exactly. This is not desirable behaviour given

the relatively low bandwidth and the high transmission ratio of the ESB actuation. Hence, we consider a control strategy in which the low-frequency components are tracked, and use the high bandwidth of the PBs to ensure the desired joint torques $\boldsymbol{\tau}^*$ are achieved by the net torque from both contributions: $\boldsymbol{\tau}_p + \boldsymbol{\tau}_{PB} \approx \boldsymbol{\tau}^*$.

This section will detail the PB torque control and ESB pretension control strategies. The architecture requires only motor and joint encoders and ESB load cell measurements. The resulting desired motor torques $\boldsymbol{\tau}^*_{M1}$ and $\boldsymbol{\tau}^*_{M2}$ are used as references by low-level motor current controllers.

8.4.1 PB torque control

To achieve desired joint PB torques, we exploit the flexible torsional transmission as both a force regulating and measuring element. By controlling the motor-side variables and using a model of the torsional transmission, we achieve link-side torque control. Neglecting the damping, desired PB torques $\boldsymbol{\tau}_{PB}$ are achieved by motor positions given by:

$$\boldsymbol{\theta}^*_1 = K^{-1}_{PB}\boldsymbol{\tau}^*_{PB} + \mathbf{q} \tag{8.20}$$

where $K_{PB} \in \Re^{N\times N}$ denotes the diagonal matrix of PB stiffnesses. We then control the $M1$ torques using a position control with compensation scheme (blue block in Fig. 8.7):

$$\boldsymbol{\tau}^*_{M1} = r_1^{-1}\hat{\boldsymbol{\tau}}_{PB} + K_m\left[\mathbf{e}_m + D_m\dot{\mathbf{e}}_m\right] \tag{8.21}$$

where $\mathbf{e}_m = \boldsymbol{\theta}^*_1 - \boldsymbol{\theta}_1 \in \Re^N$ denotes the motor position errors, and $K_m, D_m \in \Re^{N\times N}$ denote diagonal control gain matrices. The compensation term $\hat{\boldsymbol{\tau}}_{PB} \in \Re^N$, which is scaled by the Harmonic Drive transmission ratio, consists of the PB torques, estimated from the measured deflections: $\hat{\boldsymbol{\tau}}_{PB} = K_{PB}\left(\boldsymbol{\theta}_1 - \mathbf{q}\right)$ where $\hat{[.]}$ denotes the estimated variables, since we neglect the damping components.

8.4.2 Pretension Control

Recalling (8.8) and solving for p, we can calculate the pretension position p_{opt} that achieves a desired monoarticulated ESB torque τ^*_m given the joint position q. This

results in

$$p_{opt} = rq + \eta_2 \tau_m^* \tag{8.22}$$

where $\eta_2 = (rk_p)^{-1}$. In the biarticulated case (8.10) with a driven joint i, spanned joint j, and desired driven joint torque $\tau_{b,i}^*$ this results in

$$p_{opt,i} = r_{b,i} q_i + r_{b,j} q_j + \eta_{3,i} \tau_{b,i}^* \tag{8.23}$$

where $r_{b,i}$ and $r_{b,j}$ denote the pulley radii at joints i and j, and $\eta_{3,i} = (r_{b,i} k_{p,i})^{-1}$ denotes the pulley radius and ESB stiffness parameters for the driven joint. Using (8.22) and (8.23), we construct the vector function $\mathbf{p}_{opt}(\mathbf{q}, \boldsymbol{\tau}_{p,d}^*) \in \Re^N$ that calculates the vector of pretension positions that produce desired ESB torques for our chosen actuator configuration.

As noted before, we choose to track the low-frequency components of each element of $\mathbf{p}_{opt}$. We write this as $\tilde{\mathbf{p}}_{opt}$, where $\tilde{[.]}$ denotes low-pass filtering. This structure ensures that in steady state $\tilde{\mathbf{p}}_{opt} \to \mathbf{p}_{opt}$, such that $\boldsymbol{\tau}_p \to \boldsymbol{\tau}^*$ which means all torque is generated by the ESBs, resulting in the most energy efficient steady-state operation. The Low-Pass Filters (LPFs) (LPF blocks in Fig. 8.7) have a cut-off frequency of 0.03 Hz. To avoid slack in the compliant elements due to lag resulting from filtering, we calculate zero pretension positions (positions where $\Delta L_p = 0$ for all ESBs) as $\mathbf{p}_{zp}(\mathbf{q}) = \mathbf{p}_{opt}(\mathbf{0}, \mathbf{q})$, and define the vector of pretension reference positions $\mathbf{p}^* = [p_1^*, \ldots, p_N^*]^T \in \Re^N$ as

$$p_i^* = \max\left(\tilde{p}_{opt,i}, p_{zp,i}\right) \ , \ i = 1 \ldots N. \tag{8.24}$$

The pretension positions are then controlled by applying position control with compensation (red block in Fig. 8.7):

$$\boldsymbol{\tau}_{M2}^* = \eta_4^{-1} \boldsymbol{\tau}_p + K_p \left[\mathbf{e}_p + D_p \dot{\mathbf{e}}_p\right] \tag{8.25}$$

where $\mathbf{e}_p = \mathbf{p}^* - \mathbf{p} \in \Re^N$ denotes the pretension position errors, and $K_p, D_p \in \Re^{N \times N}$ denote diagonal control gain matrices. The compensation term $\eta_4^{-1} \boldsymbol{\tau}_p$ consists of the measured ESB torques reflected to the motors, where the diagonal matrix $\eta_4 \in \Re^{N \times N}$

denotes the transmission ratios from ESB torque to $M2$ motor torque.

8.5 Results

We performed simulation studies to systematically analyse the effectiveness of the proposed design and control methods in Sec. 8.3–8.4. We compare the three actuation configurations discussed in Sec. 8.3.3, by performing an ellipsoid motion (Fig. 8.8) with the hip above the foot, to effectively utilise the range of motion of this 2-DoF system.

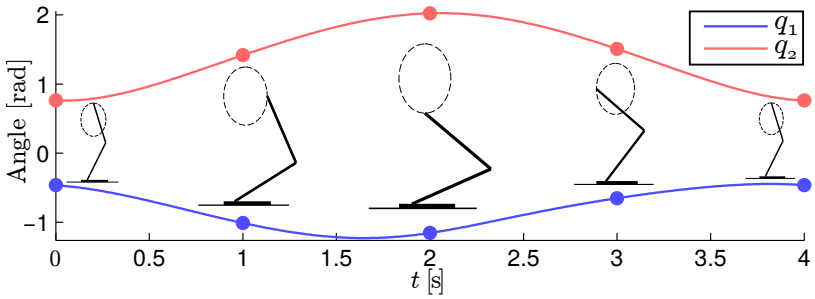

FIGURE 8.8: One period of the joint references.

The hip reference position is given by

$$\begin{bmatrix} x_{hip}(t) \\ y_{hip}(t) \end{bmatrix} = \begin{bmatrix} \alpha_x \sin(\omega t) + \beta_x \\ \alpha_y \sin(\omega t + \pi/2) + \beta_y \end{bmatrix}, \tag{8.26}$$

where $\alpha_x = 0.3l$ m, $\alpha_y = 0.4l$ m, $\omega = \pi/2$ rad/s, $\beta_x = 0.15l$ m, and $\beta_y = 1.45l$ m. We use electrical energy consumption as our energy efficiency metric, since this is often the factor that limits the autonomous operation of mobile robotic systems due to battery constraints. We do so by calculating the total (PB+ESB) actuator power of ankle (P_{A1}) and knee (P_{A2}), as well as their sum P. Simulations were performed in MathWorks MATLAB R2013b Simulink with the ode45 variable-step solver with absolute and relative tolerances of 1e-8.

No ESB

In the conventional SEA configuration we observe a total electrical power consumption of 385.8 W, most of which is used by the knee actuator (Fig. 8.9g), due to very

large gravitational load containing a large DC component of ≈100 Nm, as observed in Fig. 8.9m.

Monoarticulated Configuration

In the monoarticulated configuration, the gravitational loading is largely compensated by the ESBs (Fig. 8.9k, 8.9n). The torque generated by the PBs converges to a zero mean, demonstrating the DC component is completely generated by the ESBs. This results in improved tracking performance and an electrical power consumption of 91.0 W (Fig. 8.9h), approximately 4 times smaller than without ESB.

Biarticulated Configuration

The biarticulated actuation utilises the ESBs to generate the desired torques to an even larger extent. The biarticulated ESB extends by both knee extension and dorsiflexion. Thus, moving the hip forward and extending the leg naturally generates torque on the ankle, as observed in Fig. 8.9l, where the ankle torque is generated to a greater extent by the biarticulated ESB compared to the monoarticulated case. Due to the unidirectionality of ESBs, the negative joint torques are generated by the PB. Furthermore, the contribution of the combined ESB torques on the knee is also increased compared to the monoarticulated case, as observed in Fig. 8.9o.

This human-inspired configuration shows further reduced electrical power consumption of 24.7 W (Fig. 8.9i), over 15x smaller than without ESB and 3.7x smaller than the monoarticulated configuration. In both cases, the peak power requirements are also significantly reduced.

As additional verification, we studied randomly generated motions. Compared to SEA, the monoarticulated and biarticulated cases were 4–10x and 10–25x more energy efficient, respectively.

8.6 Conclusions

In this Chapter, the design concepts and control structure of our Asymmetric Compliant Actuation (ACA) concept were generalised and extended to multi-DoF robotic systems. Furthermore, the concept of biarticulated actuation structures was explored as an alternative to purely monoarticulated configurations.

Extensive simulation studies of our methods on a 2-DoF leg as proof of concept effectively demonstrated significant improvements in energy efficiency and tracking accuracy, compared against conventional Series-Elastic Actuation found on many robotics systems. Notably, compared to SEA, the monoarticulated case required 4-10x less energy and the biarticulated case required over 10-25x less energy. Furthermore, peak electrical power requirements were greatly reduced. Systems that use these concepts can therefore be designed with smaller, lighter, more efficient main actuators, further increasing their performance.

The addition of a secondary actuation branch requires additional components; however, these secondary components can be implemented in a small and lightweight manner due to the high transmission ratio. As in Chapter 7, the elastic elements can be implemented using lightweight natural rubber to achieve very large energy storage to weight ratio. The increase in energy efficiency greatly offsets the small increase in weight and complexity. Given these very promising results we believe the ACA concept can contribute to improved energy efficiency of many systems in the robotics field.

The work presented in this Chapter provides the necessary guidelines to build new hardware that utilises these concepts. The developed methods are applied to the design of a 3-DoF prototype leg in the next Chapter.

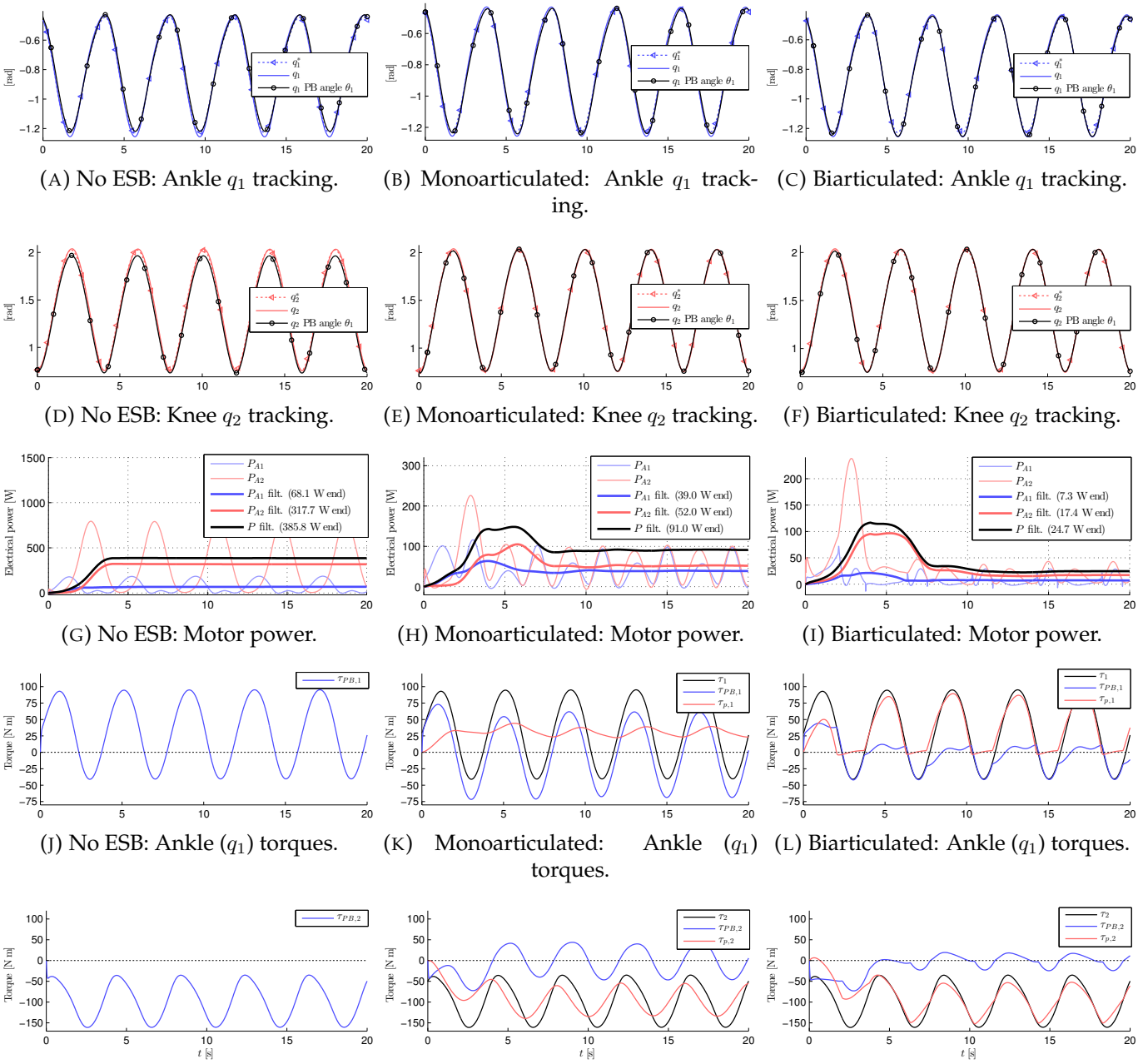

(A) No ESB: Ankle q_1 tracking. (B) Monoarticulated: Ankle q_1 tracking. (C) Biarticulated: Ankle q_1 tracking.

(D) No ESB: Knee q_2 tracking. (E) Monoarticulated: Knee q_2 tracking. (F) Biarticulated: Knee q_2 tracking.

(G) No ESB: Motor power. (H) Monoarticulated: Motor power. (I) Biarticulated: Motor power.

(J) No ESB: Ankle (q_1) torques. (K) Monoarticulated: Ankle (q_1) torques. (L) Biarticulated: Ankle (q_1) torques.

(M) No ESB: Knee (q_2) torques. (N) Monoarticulated: Knee (q_2) torques. (O) Biarticulated: Knee (q_2) torques.

FIGURE 8.9: Simulation results. Left column: without ESB (conventional SEA), middle column: monoarticulated configuration, right column: biarticulated configuration. The *filt.* variables denote averages over the period ($2\pi/\omega$ = 4.0 s).

9

Design of a 3-DoF Leg with Series & Parallel Compliant Actuation

This Chapter presents the development of a 3-DoF leg with series and parallel compliant actuation, building on the methods for design optimisation of multi-articulated compliant actuation structures for articulated robots developed in Chapter 8. As in the previous Chapter, series-elastic main actuators are combined with parallel high efficiency energy storage branches, to substantially improve energy efficiency. The leg design is semi-anthropomorphic, with similar mass and mass distribution to the human limb, and includes a biarticulated actuation configuration. The parallel branches driven by secondary motors for adjustable pretension, and their design parameters are optimised. The mechanical design of the prototype leg is presented,

introducing details of the actuation configuration principles employed. Preliminary experimental data are presented, in which a baseline series-elastic-only configuration is compared with configurations with mono- and biarticulated parallel branches, respectively. The results effectively demonstrate the concept's potential, showing improvements of 53% and 60% in electrical power consumption while the leg is executing loaded cyclic motion profiles.

This Chapter is structured as follows. Sec. 9.1 describes the chosen actuation configurations and realised 3-DoF leg design, followed by design parameters optimisation in Sec. 9.2. Initial experimental studies are presented and data are analysed in Sec. 9.3. Lastly, Sec. 9.4 concludes with a discussion of the results.

9.1 Semi-anthropomorphic Leg Design

9.1.1 Concept & Actuation Configurations

For the design of the 3-DoF leg presented in this work inspiration was taken from the human lower limb. To achieve this, the dimensions and mass distribution of the human limb were investigated, and compared with those of existing humanoid designs such as WALK-MAN [2]. Based on these values, target specifications for dimensions and segment weight were set for the design, as given in Table 9.1. We opted for a leg size slightly under average human size, and aimed for mass not exceeding the human limb, and with similar mass distribution. This results in a semi-anthropomorphic design corresponding to a $\approx$1.50 m humanoid.

The initial design sketches are shown in Fig. 9.1. The design features three actuated degrees of freedom: ankle, knee and hip. The joints are driven by series-elastic actuators, which for the knee and ankle are mounted above the joints and transmit their forces through four bar linkages. This decreases the leg's moment of inertia with respect to the hip joint. The trunk is loaded with a weight representative of a full humanoid robot.

		Length [m]	Mass [kg]
Human male (1.75 m, 75 kg, [70])	Thigh	0.406	7.88
	Shank	0.432	3.38
	Foot	0.026	1.13
WALK-MAN [2]	Thigh	0.356	5.1
	Shank	0.400	5.7
	Foot	0.143	3.3
Our robot	Thigh	0.350	2.79, 3.60, 4.24 (goal: <7.50)
	Shank	0.350	3.08, 3.91, 3.20 (goal: <3.50)
	Foot	0.063	1.70

TABLE 9.1: Dimensions and mass distribution of the human lower limb [70], the humanoid WALK-MAN [2] (excluding yaw/roll joints) and design parameters for the robot presented in this Chapter. Note the foot dimension is height, not length. Mass values for our robot given as SEA only, monoarticulated, and biarticulated configurations, respectively.

Three actuation configurations were considered, to show both the potential of our proposed actuation concept as well as investigate the effectiveness of biarticulated actuation configurations. Shown in Fig. 9.1, the three concepts are as follows:

1. **SEA only**: In the first configuration all joints are driven exclusively by SEAs, to serve as a baseline actuation arrangement which is common in most state-of-the-art articulated robot designs.

2. **Monoarticulated**: In the second configuration the ankle and knee joints are augmented with a secondary parallel actuation branch.

3. **Biarticulated**: The third configuration again features two joints with parallel actuation branches, however in this case one of the Energy Storage Branches is biarticulated: The ESB for the ankle spans the knee joint and is driven by a motor on the back of the thigh. This tendon spanning both the knee and ankle joints is functionally similar to the gastrocnemius muscle in humans, which allows power transfer from the knee to the ankle joint upon extension.

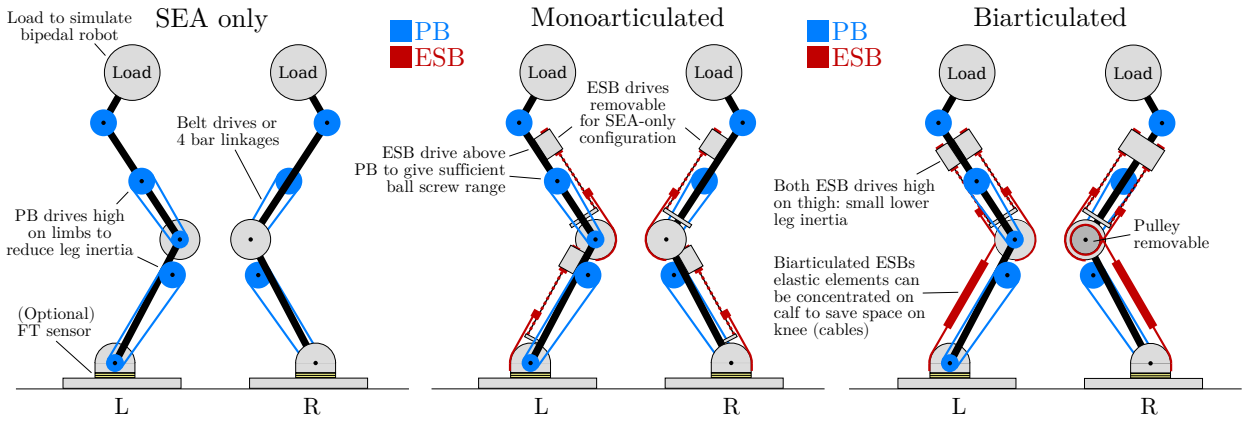

FIGURE 9.1: Concept drawings of the 3-DoF leg in SEA-only, monoarticulated, and biarticulated actuation configurations. Series-elastic Power Branch (PB) actuation is shown in blue, and the parallel Energy Storage Branches (ESBs) are shown in red.

9.1.2 Realised Design

Based on the goal design parameters and simulation studies, a hardware realisation was developed. Fig. 9.2 shows the design in CAD in all three actuation configurations. Note that the trunk link is 43 cm in length to provide ample space for loading the leg. Fig. 9.3 shows the realised prototype, with important components highlighted.

The ESB drive units can be quickly mounted and dismounted from the leg, to allow for fair comparison between the different configurations. From Table 9.1 it can be observed that despite the relatively low mass of the ESB units, the different configurations result in significantly different mass distributions between thigh and shank segments. The desired < 3.50 kg mass for the shank is not achieved in the monoarticulated configuration. The biarticulated configuration has a mass distribution which is closer to the human limb. The foot has slightly more mass than the human equivalent; we have initially opted for a somewhat wide foot, as the robot is planar but not constrained to the sagittal plane. Furthermore, the foot is instrumented with a 6-DoF force-torque sensor.

Three identical medium-sized SEAs [14] are used, consisting of Kollmorgen TBMS-6025 motors and 80:1 CPL-20 Harmonic Drive gearboxes, in series with custom planar flexure elements with stiffness of approx. 5800 Nm/rad. The units can provide

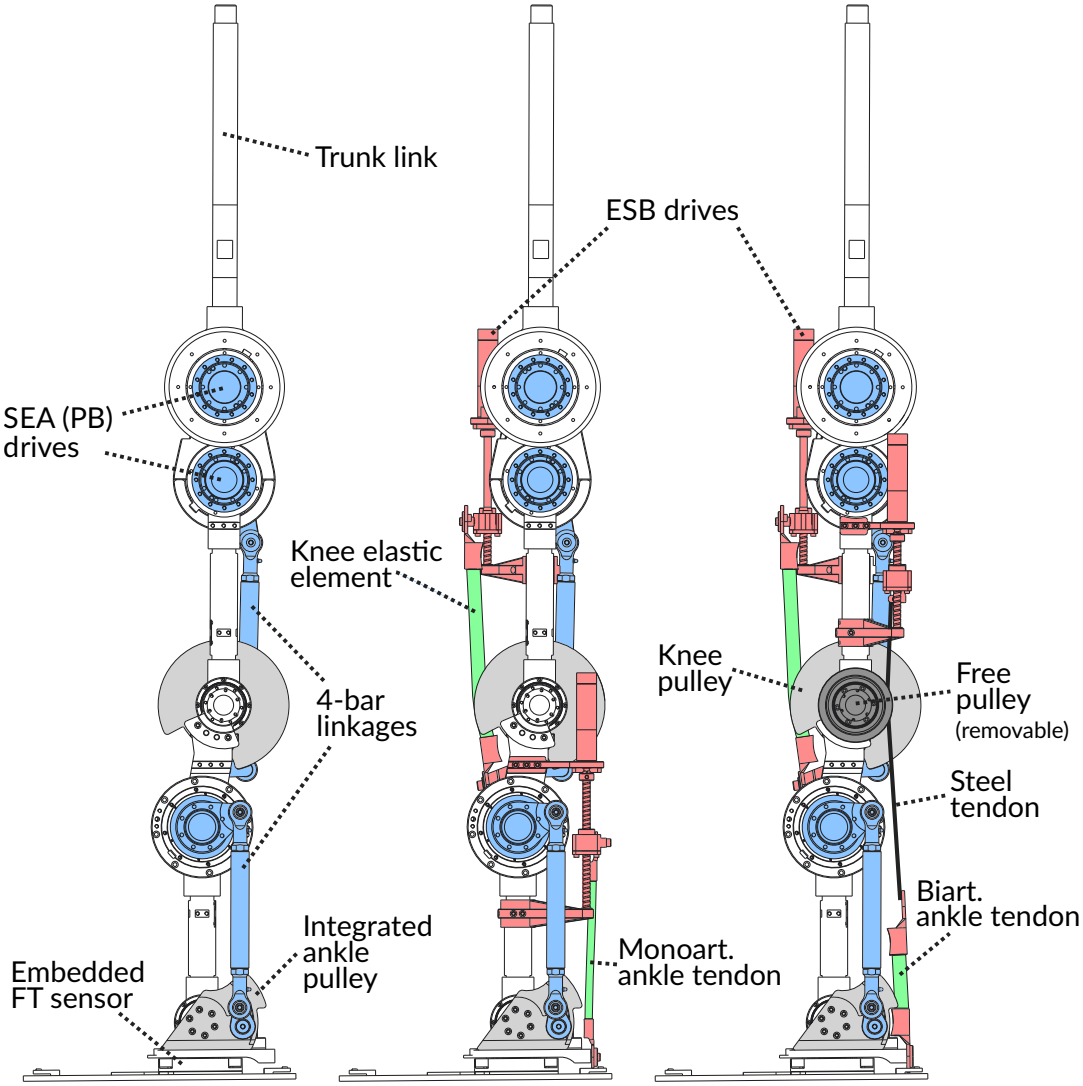

FIGURE 9.2: CAD: SEA-only, mono- and biarticulated configurations.

peak torque up to 127 Nm and provide torque sensing through deflection measurements of the elastic elements. They feature an integrated design with power and EtherCAT communication electronics mounted directly on the actuator.

The ESBs are driven by Maxon EC22 motors with 53:1 gearboxes, in series with ball screws with 5 mm pitch. The ball screw nuts are instrumented with strain gauges for direct linear force measurement. Due to the combined transmission ratio of the reduction gearbox and ball screw, the torque requirement on the ESB motor is small, resulting in a high efficiency drive. The main requirement for the ESBs is to store a large amount of potential energy. To achieve this we utilise rubber-type elastic cords. The cords are constructed from a number of elastic strands enclosed inside a woven braided cotton sheath. The high required stiffness of the biarticulated ESB tendon

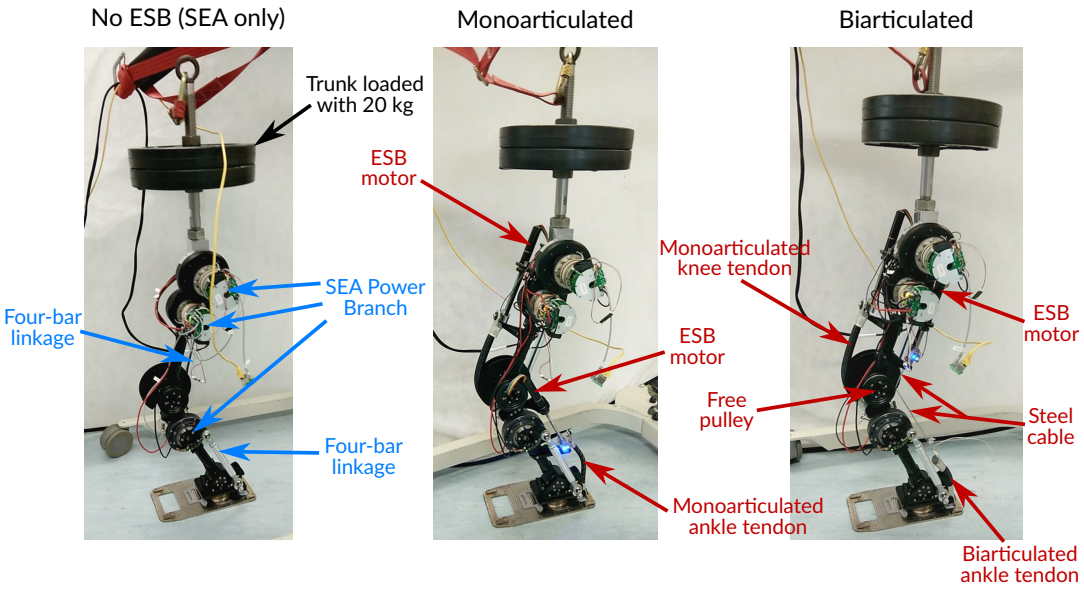

FIGURE 9.3: Realised prototype.

warrants the use of a short elastic element; therefore, a steel tendon is used in series with the element.

9.2 Optimisation of Design Parameters

We optimise the actuation parameters of the leg prototype using the method proposed in Chapter 8. The relevant ESB parameters for both configurations are shown in Fig. 9.4. The optimisation procedure considers pulley radii $r^{\circ}_{p,\circ}$, elastic element stiffness values $k^{\circ}_{p,\circ}$, and pretension positions $p^{\circ}_{\circ}$ as optimisation variables. The optimisation workspace is chosen as the subset of the joint workspace that keeps the center of pressure within the foot support polygon, i.e. all statically stable standing configurations on flat ground, and respecting joint limits. We set the hip joint q_3 such that the trunk is in a vertical configuration for each pose: $q_3 = -(q_1 + q_2)$. The resulting joint space configurations are shown in Fig. 9.5.

The optimal ESB design parameters resulting from this procedure are listed in Table 9.2. A significantly higher optimal stiffness of the ankle tendon can be observed in the biarticulated configuration. This originates from the fact that as the leg squats down and the ankle flexes, the knee also flexes, which reduces the net elongation

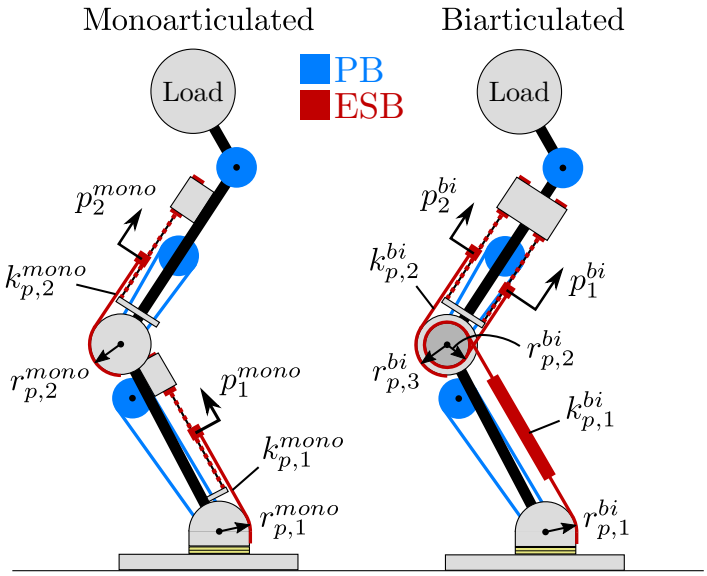

FIGURE 9.4: ESB parameters for mono- and biarticulated configurations.

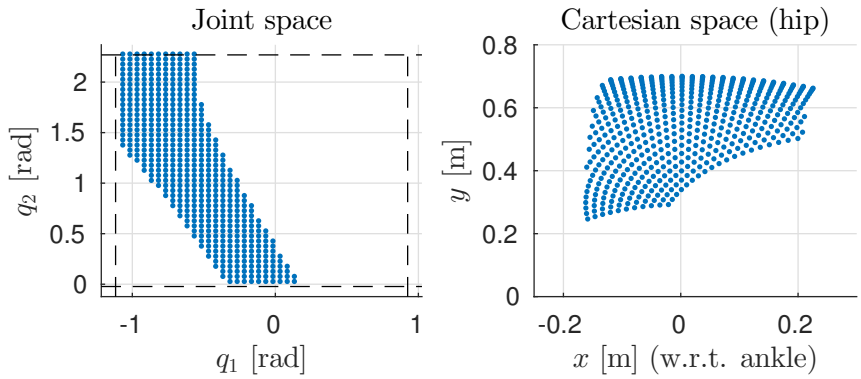

FIGURE 9.5: Optimisation joint workspace for (q_1, q_2). On the left plot, the dashed black lines denote the joint limits. The right plot shows the Cartesian coordinates of the hip w.r.t. the ankle joint.

of the tendon. The smaller elongation warrants a higher stiffness to produce the desired ankle torque.

9.2.1 Choosing Rubber-type Elastic Cords

From the optimised ESB stiffness values in Table 9.2, rubber elastic cords were selected. As their stiffness is defined in percentage elongation from rest length, this posed an interesting challenge: selecting the cords such that they simultaneously:

1. fit the space constraints;

2. do not exceed a maximum 80% elongation;

Monoart.	Value	Biart.	Value
$r_{p,1}^{mono}$	0.07 m (chosen)	$r_{p,1}^{bi}$	0.07 m (chosen)
$r_{p,2}^{mono}$	0.06 m (chosen)	$r_{p,2}^{bi}$	0.035 m
		$r_{p,3}^{bi}$	0.06 m (chosen)
$k_{p,1}^{mono}$	5.9 kN/m	$k_{p,1}^{bi}$	32 kN/m
$k_{p,2}^{mono}$	8.6 kN/m	$k_{p,2}^{bi}$	8.6 kN/m
p_1^{mono}	0.00 m	p_1^{bi}	0.00 m
p_2^{mono}	0.00 m	p_2^{bi}	0.02 m

TABLE 9.2: Optimised ESB Design Parameters.

3. provide the desired stiffness.

Rubber-type material typically has an S-shaped stiffness profile, in which the force initially increases rapidly, and then increases more slowly up to roughly 70-80% elongation, at which point it rises quickly again. Manufacturer data was linearised in the 0-80% elongation range, and diameters and rest length were chosen such that less than 10% error from the optimal values in Table 9.2 was achieved. The S-shaped profile will result in some overcompensation at small ESB elongation, but this may be compensated for by control.

9.3 Experimental Results

This Section presents initial experimental results, that effectively illustrate the potential of the prototype and actuation principles. An elliptical squatting motion was performed on all three actuation configurations, consisting of an elliptical Cartesian trajectory of the hip, defined w.r.t. the position of the ankle joint. The joint references were calculated from inverse kinematics, with the trunk link kept vertical. In these preliminary experiments, the main actuators were used in position control mode, with the ESB pretension positions held constant. The hip reference and experimental trajectories are shown in Fig. 9.6, and tracking errors, torque contributions and linear tendons forces are shown in Fig. 9.7. In the latter Figure, the left, middle and right columns contain data for the conventional SEA, monoarticulated, and biarticulated configurations, respectively. Dashed lines denote RMS SEA torques, over the 5.0 s motion period.

As can be observed from Fig. 9.7a–9.7f, bias in the joint tracking errors due to gravitational loading is significantly reduced in the monoarticulated and biarticulated cases, indicating that the actuators spend less power cancelling gravitational torques, and improving tracking accuracy for this simple position control. The differences in tracking accuracy result in slightly different pose of the leg over time, as indicated by the Cartesian trajectory of the hip, shown in Fig. 9.6. This in turn changes the loading of each joint and the elongation of the elastic elements, as can be observed in Fig. 9.7g–9.7l. Furthermore, the current required by the ESB motors to hold the pretension positions of the parallel elements was verified negligible compared to the reduction in power requirements from the SEAs.

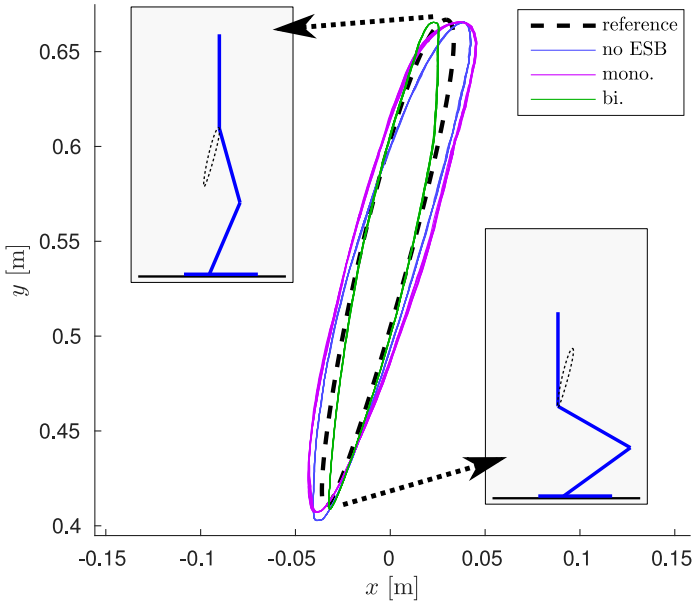

FIGURE 9.6: Cartesian hip reference (w.r.t. ankle joint) and resulting trajectories for all three configurations, following from the joint tracking performance shown in Fig. 9.7a–9.7f.

The torque measurement results demonstrate a number of key advantages of the parallel actuation design:

1. In both cases with ESBs, the ESBs significantly reduce the RMS SEA (PB) torques for both the ankle and knee joints, shown as dashed lines in Fig. 9.7g–9.7o. This results in significantly lower power consumption. These results are presented in Table 9.3, together with the electrical power consumption, calculated using actuator models. We consider only positive (i.e. delivered) electrical power, as

	No ESB	Mono.	Bi.
Ankle [Nm RMS]	24.0	24.8	13.7 ↓
Knee [Nm RMS]	55.3	25.8 ↓	25.4 ↓
Hip [Nm RMS]	4.9	7.7	6.8
Ankle [Nm peak]	36	48	27 ↓
Knee [Nm peak]	89	45 ↓	40 ↓
Hip [Nm peak]	8	14	12
Ankle [W]	2.7	1.1	2.6
Knee [W]	30.0	14.2 ↓	9.5 ↓
Hip [W]	0.4	0.1	1.1
Total electrical power [W]	33.1	15.4 ↓	13.2 ↓
Improvement	–	53%	60%

TABLE 9.3: RMS and peak SEA torques and electrical power consumption over the motion period of 5.0 s. Note we consider only positive (i.e. delivered) electrical power, as there is no recuperation mechanism.

negative power is lost as there is no recuperation mechanism. The monoarticulated configuration obtains a 53% improvement in power consumption, and the biarticulated configuration obtains a 60% improvement.

2. The biarticulated tendon excerts torque on the ankle joint (Fig. 9.7i) at more appropriate timing than the monoarticulated ankle tendon (Fig. 9.7h), resulting in a decrease in torque required by the SEA, whereas in the monoarticulated configuration it effectively has to 'work against' the ESB elastic element for part of the motion. This is due to the extension of the biarticulated element being a function of both ankle and knee angles, in the same way their configuration changes the ankle loading.

3. In this instance, the biarticulated tendon has a counterproductive effect on the required knee SEA torques (Fig. 9.7l), as the pretension of the monoarticulated knee tendon was not increased sufficiently to counteract the biarticulated tendon torque, which flexes the leg. This highlights the need for an appropriate control strategy that adjusts the pretension of the parallel tendons.

These results are in line with expectations based on the simulation study of a 2-DoF leg presented in Chapter 8.

9.4 Conclusions

This Chapter has presented the concept, design, and actuation parameters optimisation of an original 3-DoF compliant leg prototype that utilises both series and parallel compliant actuation, with the aim of increasing energy efficiency. Furthermore, the realised hardware prototype was presented together with preliminary experimental results. The results show impressive improvements in terms of torque requirements of the main actuators, resulting in significant improvements in power consumption. As suggested in Chapter 8, these reduced torque requirements also allow to choose smaller, lighter, more efficient SEAs, further improving their overall performance.

The development and realisation of the presented prototype was challenging. While these first results are very promising, some mechanical revisions are still in progress. Furthermore, only position control was used, together with fixed pretension positions of the parallel branches. Implementation of an integrated control strategy such as was used in Chapters 7 and 8, actively utilising both parallel actuation branches together in a torque-controlled manner, is currently underway. The next Chapter presents a more advanced type of control for the parallel branches, which will also be applied to this novel hardware.

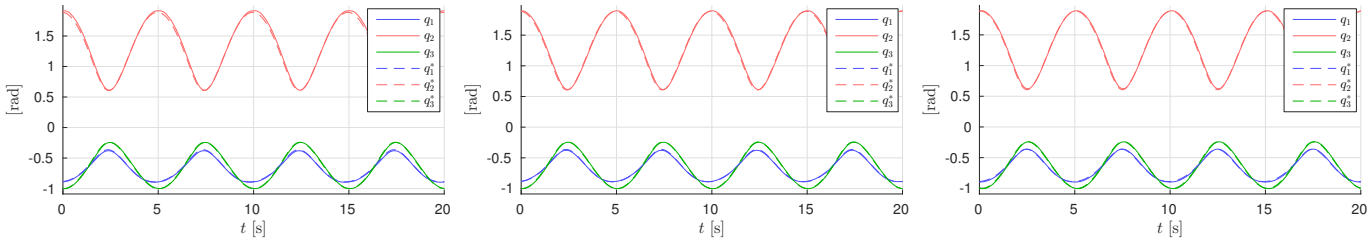

(A) No ESB: Joint tracking. (B) Monoarticulated: Joint tracking. (C) Biarticulated: Joint tracking.

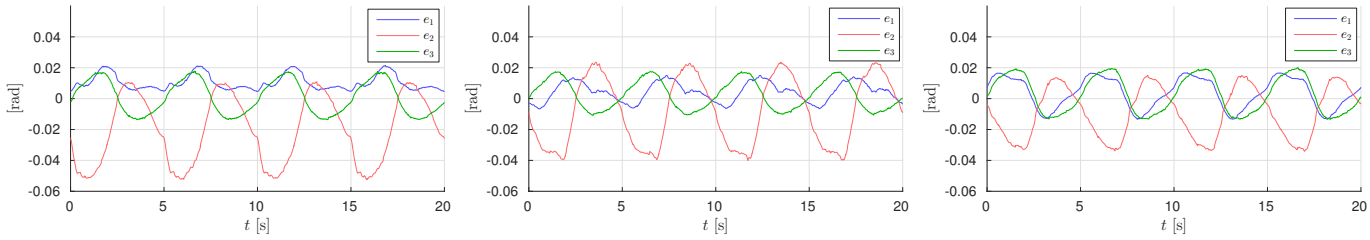

(D) No ESB: Tracking errors. (E) Monoarticulated: Tracking errors. (F) Biarticulated: Tracking errors.

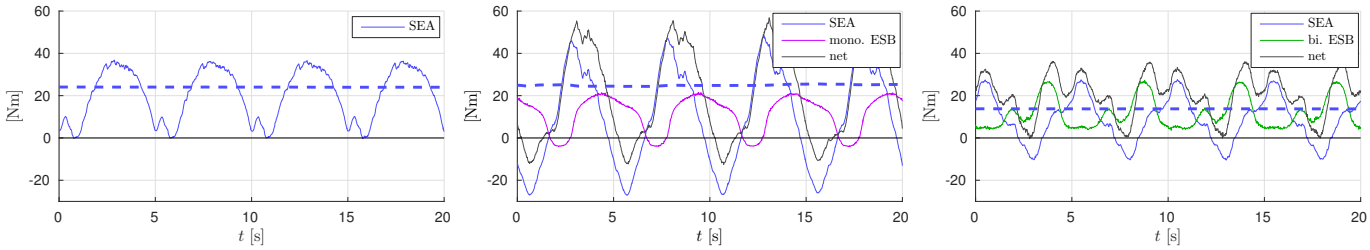

(G) No ESB: Ankle (q_1) torques. (H) Monoart.: Ankle (q_1) torques. (I) Biarticulated: Ankle (q_1) torques.

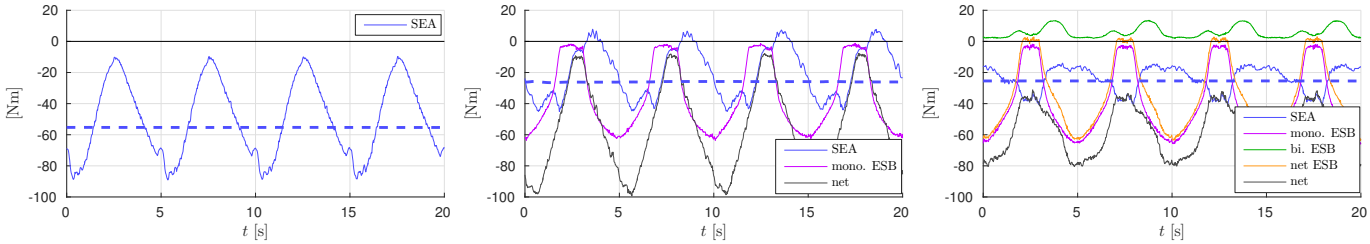

(J) No ESB: Knee (q_2) torques. (K) Monoart.: Knee (q_2) torques. (L) Biarticulated: Knee (q_2) torques.

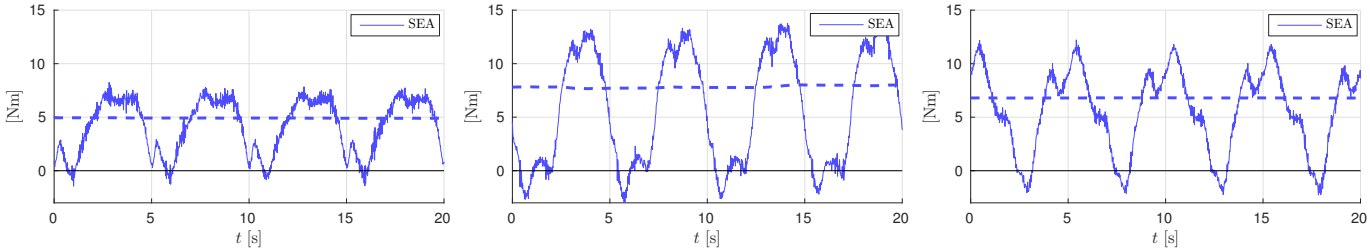

(M) No ESB: Hip (q_3) torques. (N) Monoart.: Hip (q_3) torques. (O) Biarticulated: Hip (q_3) torques.

No ESB tendons.

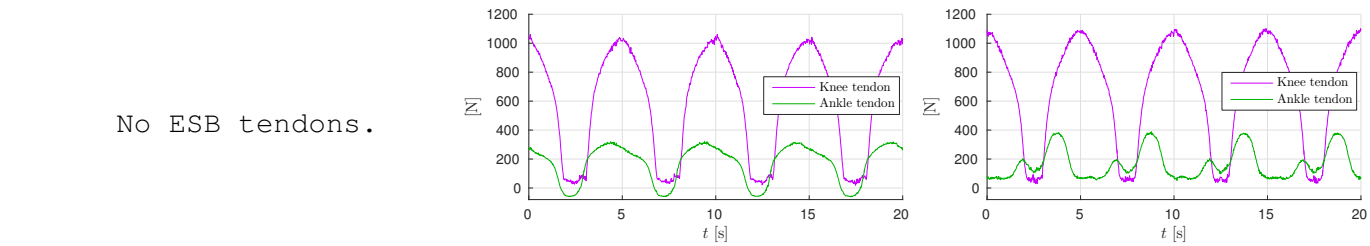

(P) Monoart.: Linear tendon forces. (Q) Biart.: Linear tendon forces.

FIGURE 9.7: Experimental results on the 3-DoF prototype.

10

Advanced Control Methods

This Chapter focuses on the model formulation and control of compliant actuation structures including multiple branches and multi-articulation for articulated robots, such as the Energy Storage Branchs (ESBs) used throughout Chapters 7, 8, and 9. It significantly contributes by proposing an elegant modular formulation that describes the energy exchange between the compliant elements and articulated multi-body robot dynamics using the concept of power flows and a single matrix that describes the entire actuation topology. Using this formulation, a novel gradient descent based control law is derived for torque control of compliant actuation structures with adjustable pretension, with proven convexity for arbitrary actuation topologies. Extensions towards handling unidirectionality of elastic elements and joint motion compensation are also presented.

A simulation study is performed on the model of the 3-DoF prototype leg presented in Chapter 9, by considering the pretension control of the ESB parallel compliance in

the mono- and biarticulated configurations. The data demonstrate the effectiveness of the proposed modelling and control methods. Furthermore, it is shown the biarticulated topology provides significant benefits over the monoarticulated arrangement.

This Chapter is structured as follows. Sec. 10.1 builds up the proposed model formulation, starting at single-joint, single-branch systems and expanding into multi-DoF, multi-actuator systems with multi-articulation. The proposed control strategies and an illustrative example in are elaborated on in Sec. 10.2. The simulation study to validate the proposed methods is presented in Sec. 10.3, followed by concluding remarks in Sec. 10.4.

10.1 Compliant Actuation

In general, the torque τ generated on a single joint with configuration q by a single compliant tendon can be written as

$$\tau(q) = -k\,n\,(p + n\,q), \tag{10.1}$$

where k denotes the linear tendon stiffness, n denotes the transmission ratio, and p denotes the pretension position, or the position where element is at rest length. The sign of n indicates the direction of q that increases the elongation of the tendon. The elongation Δ of the element is thus given by

$$\Delta = p + n\,q. \tag{10.2}$$

In implementations of elastic elements with high energy storage, unidirectional elements are often used, such as those constructed of natural rubber, usable in elongation and not in compression. For those, the torque is thus dependent on the sign of Δ:

$$\tau(q) = \begin{cases} -k\,n\,\Delta & \Delta > 0 \\ 0 & \text{Otherwise.} \end{cases} \tag{10.3}$$

We will explicitly take this property into account in the synthesis of our control strategies in Sec. 10.2.

10.1.1 Adjustable Parallel Compliance

While parallel compliance can provide many benefits, the parallel branches may not be continuously required, nor may their static properties be suitable for every task or configuration required of the robot. In these cases, adjustability is a desirable property of the parallel branches, that may be exploited to further increase the effectiveness of the system. In general, for the compliant arrangements considered here, three parameters may be considered for adjustment: pretension, transmission ratio(s), and engageability. Generally, stiffness of mechanical elastic elements cannot be adjusted directly; instead, adjustable transmission ratio is commonly utilised. Fig. 10.1 gives a graphical overview of the three types of adjustability. Adjustable pretension can in some sense be considered series-elastic actuation; however in contexts where the stiffness value is relatively small and the compliance augments some main drive, this is commonly referred to as parallel compliance with adjustable pretension.

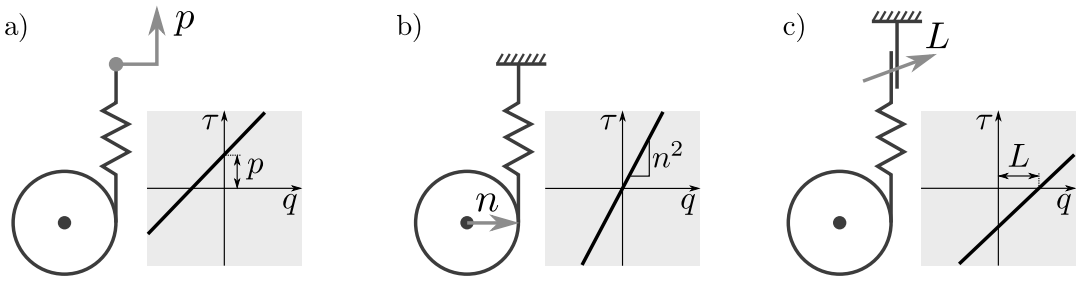

FIGURE 10.1: Types of adjustability: **a)** Pretension, **b)** Transmission ratio, and **c)** Engagement mechanism.

Each method has its respective benefits and drawbacks:

- Pretension and transmission ratio can be continuously adjusted, which is beneficial for many control strategies;
- Adjustment of the transmission ratio allows to completely disengage the branch, assuming the ratio can reach zero. However, as this method changes slope and

not offset, it cannot provide nonzero torques at the joint configuration corresponding to the elastic element's equilibrium position. Furthermore, mechanical implementation of variable transmission ratio is often cumbersome;

- Clutch mechanisms are simple to realise, however their disengagement can be problematic due to release of stored energy, when one side contains an elastic element under tension (as in this case).

Due to the binary nature of clutch mechanisms, we shall focus on the other two, namely adjustable pretension and adjustable transmission ratio. We consider the impact of these methods of adjusting compliance properties on generated torque, by returning to (10.1). For adjustable pretension, we take the derivative w.r.t. p:

$$\frac{\delta\tau}{\delta p} = -k\,n, \tag{10.4}$$

which does not depend on p, showing the adjustment is linear, and is independent of q, i.e. changing p results in a constant offset of τ. For adjustable transmission ratio, we take the derivative w.r.t. the transmission ratio n:

$$\frac{\delta\tau}{\delta n} = -k\,p - 2\,k\,n\,q, \tag{10.5}$$

which is a function of n, hence the adjustment is not linear. It can be observed the first term results in a change in offset of τ for $p \neq 0$, and the second term shows that the change of slope of $\tau(q)$ scales with $2\,n$. As noted before, for $n = 0 \rightarrow \tau = 0$, allowing to effectively disengage the compliant element.

10.1.2 Multi-articulation

In this section we formulate multi-articulated compliant branches, that span any number of joints. Assuming an articulated robot with N joints, and a configuration vector given by $\mathbf{q} = [q_1, q_2, \ldots, q_N]^T \in \mathcal{Q}$ where the joint space $\mathcal{Q} \subset \Re^N$, the deflection $\Delta \in \Re$ of a single multi-articulated branch is given by

$$\Delta = p + n_1\,q_1 + n_2\,q_2 + \cdots + n_N\,q_N, \tag{10.6}$$

where $n_1 \dots n_N \in \Re$ denote the transmission ratios for each of the N joints, shown also in Fig. 10.2. Again, the sign of each n_i indicates the direction of the corresponding joint q_i that increases the elongation of the tendon.

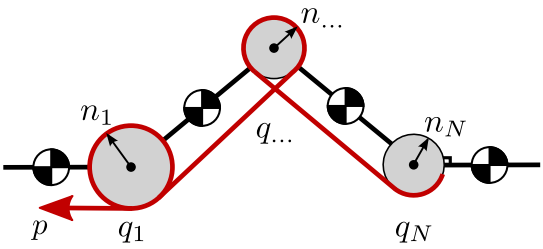

FIGURE 10.2: Multi-articulation of a single tendon for an N-joint kinematic chain. The elastic tendon with pretension position p and stiffness k is shown in red.

The torque $\tau_i \in \Re$ applied to the i^{th} joint can then be written as

$$\tau_i = -k\, n_i \left(p + n_1\, q_1 + n_2\, q_2 + \cdots + n_N\, q_N\right), \qquad i = 1 \dots N, \tag{10.7}$$

where k denotes the stiffness of the branch. Contracting the transmission ratios into vector form, we can write the torque $\boldsymbol{\tau} \in \Re^N$ applied to all N joints as

$$\boldsymbol{\tau} = -\mathbf{t}^T\, k\, (p + \mathbf{t}\, \mathbf{q}) \in \Re^N, \tag{10.8}$$

where the row vector $\mathbf{t} = [n_1, n_2, \dots, n_N] \in \Re^N$ both maps the joint configurations to elastic element elongation, and maps the produced linear tendon force back to joint torques. The deflection is written using $\mathbf{t}$ as $\Delta = p + \mathbf{t}\, \mathbf{q}$, and the linear tendon force $f \in \Re$ is equal to $f = k\, (p + \mathbf{t}\, \mathbf{q})$.

In terms of adjustability of multi-articulated configurations, adjusting p affects the torque on all joints linearly:

$$\nabla_p\, \boldsymbol{\tau} = -\mathbf{t}^T\, k \in \Re^N, \tag{10.9}$$

whereas adjusting the transmission ratios $\mathbf{t}$ affects joints nonlinearly and is also dependent on $\mathbf{q}$:

$$\nabla_{\mathbf{t}}\, \boldsymbol{\tau} = -k\, (\mathbf{q}\, \mathbf{t})^T - k\, I\, (p + \mathbf{t}\, \mathbf{q}) \in \Re^{N \times N}, \tag{10.10}$$

where I denotes the N×N identity matrix. It can be observed the first term arises

from the change in elongation of the element due to the changed transmission ratio, and the second diagonal term arises from the change in conversion ratio from linear tendon force to torque on the joints.

10.1.3 Multiple Branches

In this section we expand the previous section to a unified formulation for multiple, possibly multi-articulated branches. Supposing we have M parallel elastic branches, we gather all their respective $\mathbf{t}$ vectors in an *actuation topology* matrix $T \in \Re^{M \times N}$, that fully describes the actuation topology:

$$T = \begin{bmatrix} \mathbf{t}_1 \\ \dots \\ \mathbf{t}_M \end{bmatrix}, \tag{10.11}$$

which gives rise to the vector of deflections: $\mathbf{\Delta} = \mathbf{p} + T\,\mathbf{q} \in \Re^M$, and correspondingly the total torque $\boldsymbol{\tau} \in \Re^N$ on the robot exerted by the branches:

$$\boldsymbol{\tau} = -T^T K\,(\mathbf{p} + T\,\mathbf{q}), \tag{10.12}$$

where $K \in \Re^{M \times M}$ is the diagonal matrix of stiffness values. Note that throughout this Chapter superscript $[\cdot]^T$ denotes transpose, whereas T denotes the matrix. The vector of linear tendon forces $\mathbf{f} \in \Re^M$ follows as $\mathbf{f} = K\,(\mathbf{p} + T\,\mathbf{q})$. Similarly to the single branch case, adjusting the pretensions $\mathbf{p}$ for M actuators yields:

$$\nabla_{\mathbf{p}} \boldsymbol{\tau} = -T^T K \in \Re^{N \times M}. \tag{10.13}$$

For adjustable transmission ratios, calculating $\nabla_T \boldsymbol{\tau}$ yields a 3D tensor, of which the components for the m^{th} actuator are given by

$$\nabla_{\mathbf{t}_m} \boldsymbol{\tau} = -k_m\,(\mathbf{q}\,\mathbf{t}_m)^T - k_m\,I\,(p_m + \mathbf{t}_m\,\mathbf{q}) \in \Re^{N \times M}. \tag{10.14}$$

Considering each $\mathbf{t}_m$ is of dimension N, this means that up to $N\,M$ variables are involved. Of course, usually T can be considered quite sparse since all tendons are not

driving all joints. In both cases the gradient with respect to the joint configurations is:

$$\nabla_{\mathbf{q}}\boldsymbol{\tau} = -T^T K T \in \Re^{N\times N}. \tag{10.15}$$

Stopping for a moment to consider the different dynamics of adjustable pretension and adjustable transmission of multi-articulated compliance, we find the latter arguably provides more freedom in shaping the provided torque than the former, due to changing the slope and the larger number of degrees of freedom (in multi-articulation). As aforementioned, this also adds the potential benefit of disengaging elements entirely from desired joints. However, significant drawbacks exist due to the nonlinear behaviour on a potentially much larger configuration space, combined with increased complexity in realising such structures. Therefore, at this point, we choose to focus on adjustable pretension in our modelling and control formulation.

We now proceed with a modular model formulation using energy exchange through the concept of power ports. Taking the time derivative of the deflections $\boldsymbol{\Delta}$, we find the rate of change of the deflection of the elastic elements is given by

$$\dot{\boldsymbol{\Delta}} = \dot{\mathbf{p}} + T\,\dot{\mathbf{q}}. \tag{10.16}$$

Given that the power flow into an elastic element is given by the force multiplied by rate of displacement (i.e. $P = f\,\dot{\Delta}$), we find from port-Hamiltonian theory that $\left(\mathbf{f}, \dot{\boldsymbol{\Delta}}\right) \in \Re^N$ and $(\boldsymbol{\tau}, \dot{\mathbf{q}}) \in \Re^N$ describe an N-dimensional power port that exchanges energy between the rigid body robot and compliant actuation branches driving it. This power flow is the sum of each of the power flows in/out of the individual elastic elements; indeed, power may flow between the elastic elements as well.

This concept is depicted graphically in Fig. 10.3, using Bond graph notation. The first diagram shows the notation using $\mathbf{t}$ vectors, and the bottom diagram shows how the T matrix completely describes the power flow between actuators and robot. This formulation has several advantages for rapidly evaluating different actuation topologies; by simply modifying T the transmission ratios and actuation configuration of tendons can be quickly modified. It also enables modularity of the modelling and simulation procedures by separating actuator dynamics from the articulated

multi-body dynamics of the robot.

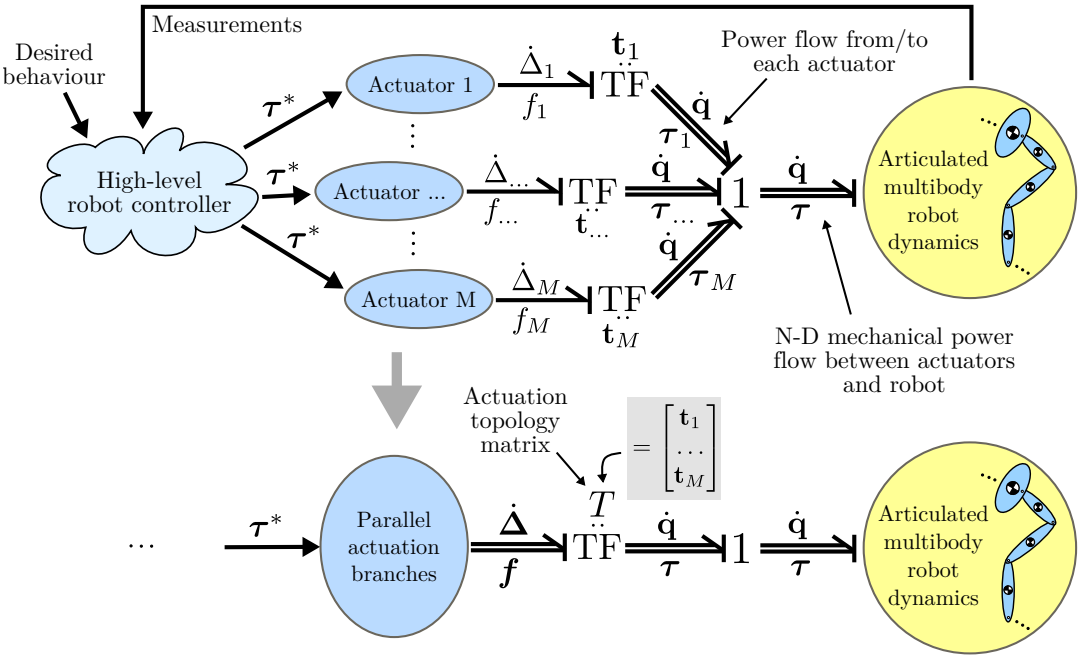

FIGURE 10.3: Model formulation using N-dimensional power ports, shown in Bond graph notation. The bottom diagram shows how the actuation topology matrix T describes the power flow between actuators and robot.

10.2 Control Strategies

Various control stategies can be employed to effectively utilise adjustability of (parallel) compliance. In Chapters 7 and 8, inversion of the per-actuator pretension-torque relations was utilised to obtain the pretension position references that lead to the desired torques. To handle coupling resulting from multiarticulation, the equations were solved in a cascaded manner. However, this method generalises poorly for arbitrarily complex structures and requires a degree of designer intuition.

In the following sections, we propose two alternative methods to solve the torque control problem through adjustable pretension, employing the multi-DoF, multi-actuator formulation of Sec. 10.1.3. The first relies on the (pseudo)inverse of the topology matrix T, which is a generalisation of the previous method. We show this method suffers from limitations in certain situations, with regards to coupling and unidirectionality of elastic elements. The second relies on gradient descent, which

allows to simultaneously take coupling and unidirectionality of the elastic elements as well as achievable pretension adjustment speeds into account.

10.2.1 (Pseudo)inverse

Returning to the multi-DoF, multi-actuator torque equation (10.12), we observe that it can be solved for $\mathbf{p}$:

$$\mathbf{p}^* = -\left(T^T K\right)^{-1} \boldsymbol{\tau}^* - T\,\mathbf{q}, \tag{10.17}$$

where $\boldsymbol{\tau}^*$ denotes the desired torque, and $\mathbf{p}^*$ denotes the resulting desired pretension positions, respectively. If T is not full rank, the pseudoinverse may be used in (10.17). This method is suitable for position controlled pretension as in Chapter 8, and is a multi-DoF generalisation of the method presented in that work. However, using the (pseudo)inverse, it is not possible to take unidirectionality of elastic elements into account. Suitable preprocessing of the desired torque vector can resolve this issue in certain cases, however this is not a general solution, hence this method is feasible only if the resulting $\boldsymbol{\Delta} \geq \mathbf{0}$ or if bidirectional elastic elements are used.

10.2.2 Gradient Descent

To obtain a gradient descent based torque control law, we start with the torque control error $\mathbf{e}$, defined as $\mathbf{e} = \boldsymbol{\tau}^* - \boldsymbol{\tau} \in \Re^N$. Taking the gradients with respect to $\mathbf{p}$ and $\mathbf{q}$, we obtain the rate of change of $\mathbf{e}$ as

$$\dot{\mathbf{e}} = \left(\nabla_{\mathbf{p}}\mathbf{e}\right)\dot{\mathbf{p}} + \left(\nabla_{\mathbf{q}}\mathbf{e}\right)\dot{\mathbf{q}}, \tag{10.18}$$

where for now we have assumed the use of bidirectional elastic elements, or equivalently, $\boldsymbol{\Delta} \geq \mathbf{0}$, i.e. no branches are in slack. Sec. 10.2.2 introduces an extension for when this assumption does not hold. Since we can assume that the desired joint torques do not depend on $\mathbf{p}$, we have $\nabla_{\mathbf{p}}\,\boldsymbol{\tau}^* = \mathbf{0}$, and the above equation can be rewritten using the definition of $\mathbf{e}$ as

$$\dot{\mathbf{e}} = -\left(\nabla_{\mathbf{p}}\boldsymbol{\tau}\right)\dot{\mathbf{p}} + \left(\nabla_{\mathbf{q}}\,\boldsymbol{\tau}^* - \nabla_{\mathbf{q}}\boldsymbol{\tau}\right)\dot{\mathbf{q}}, \tag{10.19}$$

where $\nabla_{\mathbf{q}}\,\boldsymbol{\tau}^*$ depends on high-level controller and robot dynamics, and from Sec. 10.1.3 we recall:

$$\begin{aligned}\nabla_{\mathbf{p}}\boldsymbol{\tau} &= -T^T\,K,\\ \nabla_{\mathbf{q}}\boldsymbol{\tau} &= -T^T\,K\,T.\end{aligned} \tag{10.20}$$

At this point we introduce the squared l_2-norm of $\mathbf{e}$ as our error measure. Using the results above, the chain rule, and $\nabla\|\mathbf{e}\|_2^2 = 2\,\mathbf{e}$, we compute the gradient with respect to $\mathbf{p}$:

$$\begin{aligned}\nabla_{\mathbf{p}}\|\mathbf{e}\|_2^2 &= (\nabla_{\mathbf{p}}\mathbf{e})\;\nabla\|\mathbf{e}\|_2^2\\ &= 2\,\left(T^T\,K\right)^T\,(\boldsymbol{\tau}^* - \boldsymbol{\tau})\,.\end{aligned} \tag{10.21}$$

Setting rate of change of $\mathbf{p}$ as $\dot{\mathbf{p}} = -\gamma_e\,\nabla_{\mathbf{p}}\|\mathbf{e}\|_2^2$, where $0 < \gamma_e \leq 1$ is a suitable scaling constant, ensures asymptotic convergence of $\mathbf{e}$ given $\dot{\mathbf{q}} = \mathbf{0}$; Sec. 10.2.2 discusses the extension to $\dot{\mathbf{q}} \neq \mathbf{0}$. Furthermore, note that (10.21) does not depend on $\nabla_{\mathbf{q}}\,\boldsymbol{\tau}^*$, i.e. the controller is independent of the specific robot dynamics or its high-level controllers.

By taking the second order gradient of the squared l_2-norm of $\mathbf{e}$, we show that it is globally convex, and thus $\mathbf{e}$ converges to the global minimum:

$$\begin{aligned}\nabla_{\mathbf{p}}^2\|\mathbf{e}\|_2^2 &= \nabla_{\mathbf{p}}\left[2\,\left(T^T\,K\right)^T\,(\boldsymbol{\tau}^* - \boldsymbol{\tau})\right]\\ &= 2\,\left(T^T\,K\right)^T\,\left(T^T\,K\right),\end{aligned} \tag{10.22}$$

which is positive definite as the quadratic form is always positive definite. This proves global asymptotic convergence of the error.

Constraint

The previous section assumed that either bidirectional elastic elements were used, or equivalently, unidirectional elements for which the elongation $\boldsymbol{\Delta} \geq \mathbf{0}$. This Section adds a dynamic potential function of which we take the gradient, so that the control

algorithm will never attempt to descend in directions that run the tendons into slack, and, conversely, avoids that tendons are run into slack due to joint motion.

To enforce unidirectionality constraints while maintaining continuity and global convexity, we add a quadratic constraint potential term $c(\mathbf{p})$, given by:

$$c(\mathbf{p}) = -\gamma_{const} \, \|\boldsymbol{\Delta}^{-}(\mathbf{p}))\|_2^2, \tag{10.23}$$

where $\boldsymbol{\Delta}^{-}(\mathbf{p}) = \min(\boldsymbol{\Delta}(\mathbf{p}), \mathbf{0})$ is the element-wise minimum, i.e. the constraint is only active for branches that are currently in slack. $\gamma_{const} \in \Re$ is a large scaling constant. By adding the constraint potential gradient, $\dot{\mathbf{p}}$ is given by

$$\dot{\mathbf{p}} = -\gamma_e \, \nabla_{\mathbf{p}} \|\mathbf{e}\|_2^2 + \nabla_{\mathbf{p}} \, c(\mathbf{p}), \tag{10.24}$$

where $\nabla_{\mathbf{p}} \|\mathbf{e}\|_2^2$ is given by (10.21) and $\nabla_{\mathbf{p}} \, c(\mathbf{p}) = -2 \, \gamma_{const} \, \boldsymbol{\Delta}^{-}(\mathbf{p})$. Similarly to (10.22), the second order gradient of $c(\mathbf{p})$ results in a quadratic form which is globally convex. This constraint replaces the slack control component of the control strategy described in Chapter 8. Achievable values of $\mathbf{p}$ due to mechanical constraints can be similarly imposed in a convex manner.

Compensating for $\dot{\mathbf{q}} \neq \mathbf{0}$

To ensure the convergence of the error under non-zero joint motion, we extend the above gradient descent based control law with an additional term taking this motion into account. Given $\dot{\mathbf{q}}$, we solve $\dot{\mathbf{e}} = \mathbf{0}$ for $\dot{\mathbf{p}}$ in (10.19):

$$\begin{aligned}
\mathbf{0} &= -\left(\nabla_{\mathbf{p}} \boldsymbol{\tau}\right) \dot{\mathbf{p}} + \left(\nabla_{\mathbf{q}} \, \boldsymbol{\tau}^* - \nabla_{\mathbf{q}} \boldsymbol{\tau}\right) \dot{\mathbf{q}} \\
\left(\nabla_{\mathbf{p}} \boldsymbol{\tau}\right) \dot{\mathbf{p}} &= \left(\nabla_{\mathbf{q}} \, \boldsymbol{\tau}^* - \nabla_{\mathbf{q}} \boldsymbol{\tau}\right) \dot{\mathbf{q}} \\
\dot{\mathbf{p}} &= \left(\nabla_{\mathbf{p}} \boldsymbol{\tau}\right)^{-1} \left(\nabla_{\mathbf{q}} \, \boldsymbol{\tau}^* - \nabla_{\mathbf{q}} \boldsymbol{\tau}\right) \dot{\mathbf{q}} \\
&= -\left(T^T \, K\right)^{-1} \left(T^T \, K \, T + \nabla_{\mathbf{q}} \, \boldsymbol{\tau}^*\right) \dot{\mathbf{q}},
\end{aligned} \tag{10.25}$$

which we will refer to as $\dot{\mathbf{p}}_{dq}$. This yields the rate of change of $\mathbf{p}$ needed to compensate for the change in $\mathbf{q}$, and thus keep the error constant. The first term is equal to

$-T\,\dot{\mathbf{q}}$, and simply ensures that $\mathbf{p} + T\,\mathbf{q}$, i.e. the elongation $\boldsymbol{\Delta}$, remains constant. The second term is equal to $-\left(T^T\,K\right)^{-1}\left(\nabla_{\mathbf{q}}\,\boldsymbol{\tau}^*\right)\dot{\mathbf{q}}$ and compensates the change in desired torque due to $\nabla_{\mathbf{q}}\,\boldsymbol{\tau}^* \neq \mathbf{0}$. Of course, this last term requires knowledge of how the desired torques will change as the joint configurations change, and is generally not trivial to implement. Combining (10.25) with (10.24):

$$\dot{\mathbf{p}} = -\gamma_e\,\nabla_{\mathbf{p}}\|\mathbf{e}\|_2^2 + \nabla_{\mathbf{p}}\,c(\mathbf{p}) + \gamma_{dq}\,\dot{\mathbf{p}}_{dq}, \tag{10.26}$$

we obtain the rate of change of $\mathbf{p}$ that results in global asymptotic convergence of $\mathbf{e}$. The scaling constant $0 \leq \gamma_{dq} \leq 1$ avoids excessive adjustment of the pretension to compensate the joint motion, which for high gear ratios may reduce energy efficiency, and is dependent on the mechanical implementation of the actuators.

Computing the Adjustment Velocities

The rate of change of $\mathbf{p}$ given by (10.26) may not be achievable in practice due to speed limitations following from the mechanical implementation. Hence, $\dot{\mathbf{p}}$ is scaled as follows to obtain the reference adjustment velocity $\dot{\mathbf{p}}^*$:

$$\dot{\mathbf{p}}^* = \alpha\,\dot{\mathbf{p}}, \tag{10.27}$$

where

$$\alpha = \begin{cases} \frac{p_{vmax}}{\max(|\dot{\mathbf{p}}|)} & \max(|\dot{\mathbf{p}}|) > p_{vmax} \\ 1 & \text{Otherwise} \end{cases}, \tag{10.28}$$

and p_{vmax} denotes the maximum achievable adjustment velocity. This ensures none of the branches are commanded beyond their speed limit, which would result in not descending the gradient of the error norm in the correct direction.

10.2.3 Rankedness of T

The case of T not being full rank has one important consequence; the solution is redundant. An intuitive interpretation of this is the example of two antagonistic branches driving a single joint, in which increasing the tension of both in a certain

proportion (given by their relative transmission ratio and stiffness values) does not result in a change of net torque. This is an example of a single rank deficiency of T, resulting in a line in the $\mathbf{p}$ configuration space providing identical joint torques. For more complex systems, T may be multiple rank deficient.

Since optimal energy efficiency is obtained by minimising the tension throughout the system that loads the pretension mechanisms, a unique solution may be obtained in the null space of the obtained solution. In the following we suggest two extensions towards this end.

Pseudoinverse

When using the pseudoinverse based pretension control of Sec. 10.2.1, the following extension may be used, minimising the squared l_2-norm of the deflections $\mathbf{\Delta}$ in the null space of the solution of (10.17):

$$\begin{aligned} \min_{\mathbf{x}} \|\mathbf{\Delta}\|_2^2 &= \|\mathbf{p}_{psdo} + Z\,\mathbf{x} + T\,\mathbf{q}\|_2^2 \\ \text{s.t.} \quad \mathbf{\Delta} &\geq \mathbf{0} \quad \text{and} \quad \underline{\mathbf{p}} \leq \mathbf{p}_{psdo} + Z\,\mathbf{x} \leq \overline{\mathbf{p}}\,, \end{aligned} \tag{10.29}$$

where $Z = \ker\left(-T^T\,K\right)$, $\mathbf{p}_{psdo}$ denotes the pseudoinverse solution for $\mathbf{p}^*$ given by (10.17), and $\underline{\mathbf{p}}$, $\overline{\mathbf{p}}$ denote the lower- and upper-bounds on $\mathbf{p}$, respectively. Given a solution $\mathbf{x}_{opt}$ of (10.29), the new value for the desired pretension positions $\mathbf{p}^*$ is given by $\mathbf{p}_{psdo} + Z\,\mathbf{x}_{opt}$.

Gradient Descent

For the gradient descent based solution of Sec. 10.2.2, one may add a gradient term $c_{tens}(\mathbf{p})$:

$$c_{tens}(\mathbf{p}) = -\gamma_{tens}\,\|\mathbf{\Delta}(\mathbf{p}))\|_2^2, \tag{10.30}$$

for which the gradient w.r.t. $\mathbf{p}$ is given by $\nabla_{\mathbf{p}}\,c_{tens}(\mathbf{p}) = -2\,\gamma_{tens}\,\mathbf{\Delta}(\mathbf{p})$. This gradient is then added to (10.26). For simplicity and illustration of the core ideas of this work however, we shall focus on systems with full rank T for the remaining Sections.

10.2.4 An Illustrative Example

To illustrate the core ideas behind the gradient descent based control law, we start with a simple example of a biarticulated robot with two joints and two adjustable compliant tendons in a static configuration ($\dot{\mathbf{q}} = 0$). The actuation topology is described by

$$T = \begin{bmatrix} \mathbf{t}_1 \\ \mathbf{t}_2 \end{bmatrix} = \begin{bmatrix} -0.1 & -0.2 \\ 0 & 0.3 \end{bmatrix}, \tag{10.31}$$

i.e. the first tendon is biarticulated, and the second is monoarticulated. The first joint is driven only by the first tendon, and the second joint is driven by both tendons in an antagonistic manner. We assume the tendons to be unidirectional. The stiffness matrix K is given by $K = \mathrm{diag}\,(1000, 1000)$, and the joint configuration $\mathbf{q} = [0, 0]^T$. The reference torques are set to $\boldsymbol{\tau}^* = [10, -30]^T$ Nm in this example. Furthermore, we set the constraint parameter $\gamma_{const} = 10^8$ and gradient descent parameter $\gamma_e = 5{*}10^{-6}$. Lastly, we assume a maximum adjustment velocity of $p_{vmax} = 0.05\,\mathrm{m/s}$. The landscape of the squared l_2-norm is shown in Fig. 10.4, together with six example evolutions with varying initial conditions for $\mathbf{p}$. They can be seen to all converge to the global minimum, indicated by the vertical dashed line.

The time evolutions of $\|\mathbf{e}\|_2^2$, $\boldsymbol{\tau}$, and $\mathbf{p}$ are shown in Fig. 10.5. As the desired torques can be achieved with $\boldsymbol{\Delta} \geq \mathbf{0}$ and T is full rank, the error norm converges to zero for all evolutions. One can observe that while $\mathbf{p}$ takes relatively long to converge (bottom figures), this is beneficial: the error norm is very small after 5 seconds (top-left figure), and further adjustment of the pretension yields only small reduction of the error. Out of these six example evolutions, numbers 1–4 have initial conditions where at least one of the two branches is in slack. It can be seen that the constraint described in Sec. 10.2.2 is effective, driving the branches out of slack at the maximum velocity. From the time evolutions of p_1 and p_2 (bottom figures), one may be tempted to think there is undesired overshoot in the pretension positions (e.g. evolution 1). However, this "overshoot" is desired, as due to the biarticular coupling between the joints, this reduces the torque error norm while the other pretension position converges.

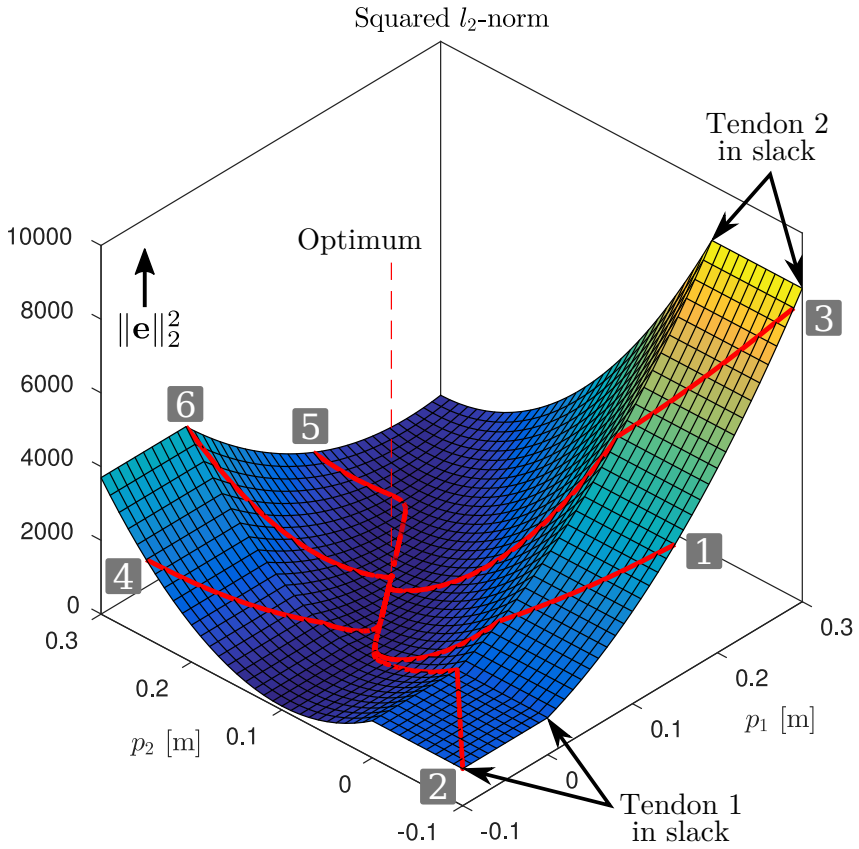

FIGURE 10.4: Gradient descent: Squared l_2-norm of $\mathbf{e}$. The superimposed red lines show example evolutions (see also time evolutions in Fig. 10.5) of $\mathbf{p}$ and the corresponding squared l_2-norm of the error. They can be seen to converge to the global minimum, indicated by the vertical dashed line.

10.3 Simulation Study

In this Section we present a simulation study on a model of the planar 3-DoF leg prototype presented in Chapter 9. The model includes viscous friction components at the joints, actuator dynamics with friction in the motor drives and drive trains, and elastic element internal damping. Furthermore, low-level torque control is implemented for the SEAs, velocity control is implemented for the parallel pretension motors, and voltage and current limits are imposed. For brevity we skip its dynamics modelling; it is analogous to that of the 2-DoF leg in Chapter 8. A diagram of the model and its parameters are shown in Fig. 10.6. In this simulation study we consider two actuation topologies; the monoarticulated and biarticulated configurations which were described in Chapter 9. The actuation topology matrices are given

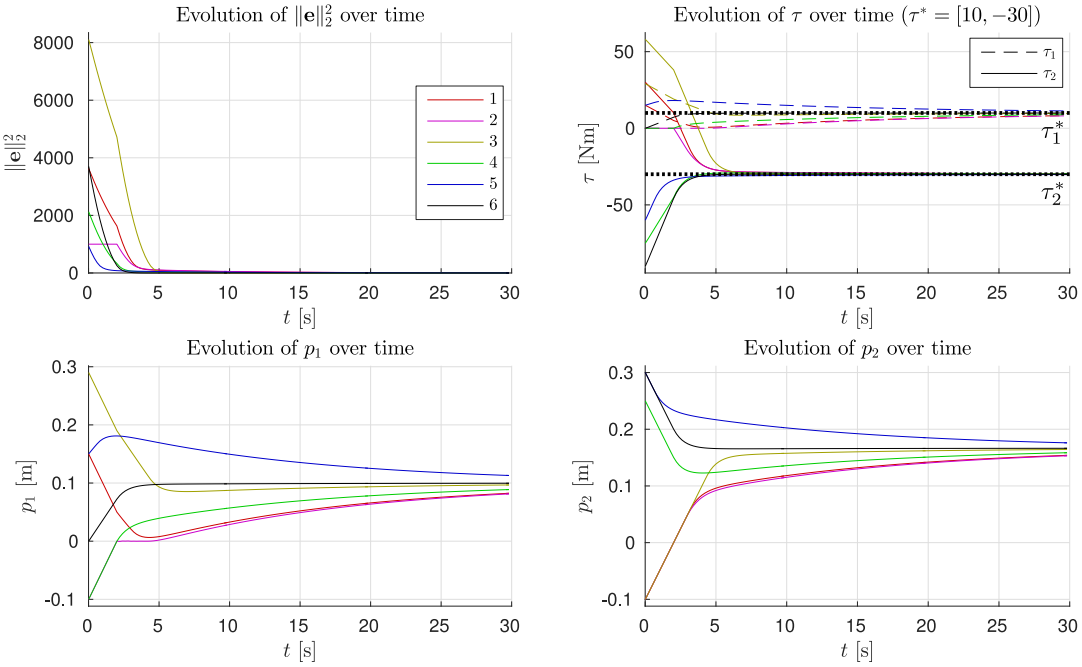

FIGURE 10.5: Time evolution of the six evolutions shown in Fig. 10.4.

by

$$T_{mono} = \begin{bmatrix} -0.07 & 0 & 0 \\ 0 & 0.06 & 0 \\ 0 & 0 & 0 \end{bmatrix},$$
$$T_{bi} = \begin{bmatrix} -0.07 & -0.0352 & 0 \\ 0 & 0.06 & 0 \\ 0 & 0 & 0 \end{bmatrix}, \tag{10.32}$$

and the stiffness matrices are given by $K_{mono} = \text{diag}(5900, 8600, 0)$ and $K_{bi} = \text{diag}(32000, 8600, 0)$, respectively. As evidenced by the zero columns in (10.32), the hip joint is not augmented with a parallel branch.

In this study, we first perform a number of point-to-point motions in Cartesian space with the hip of the robot, keeping the torso upright. Each pose is maintained for ten seconds to clearly illustrate the transient behaviour of the proposed control strategy given the system's parameters. Fig. 10.7 shows the joint configuration references and tracking for the biarticulated configuration; the monoarticulated configuration is not shown for brevity, however tracking is almost identical. The figure is augmented to show the leg poses at various time instances, showing the wide range of executed

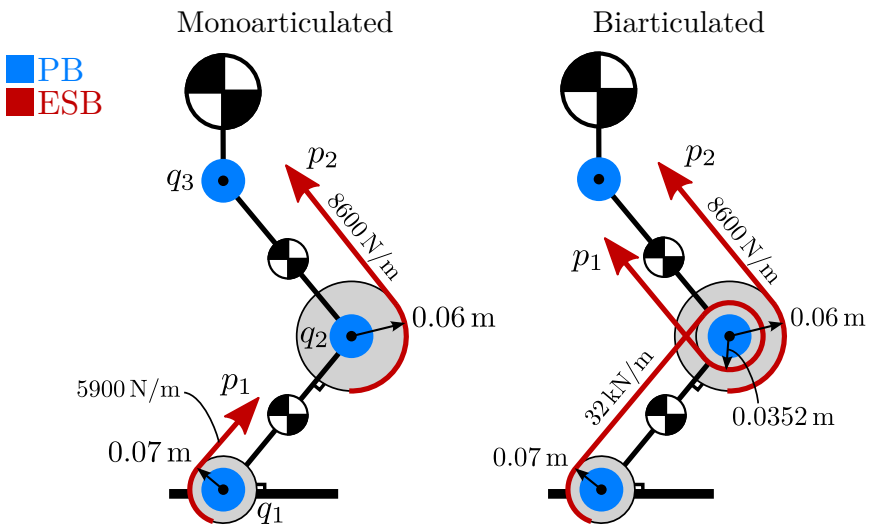

FIGURE 10.6: 3-DoF leg model used in simulation, shown in both mono- and biarticulated actuation configurations.

motions. Phases A–D and F denote the aforementioned static poses. The second part of the reference motion involves a cyclic Cartesian trajectory of the hip in an elliptical squatting motion, to demonstrate its behaviour under highly dynamic motion. This part is denoted as phase E in Fig. 10.7.

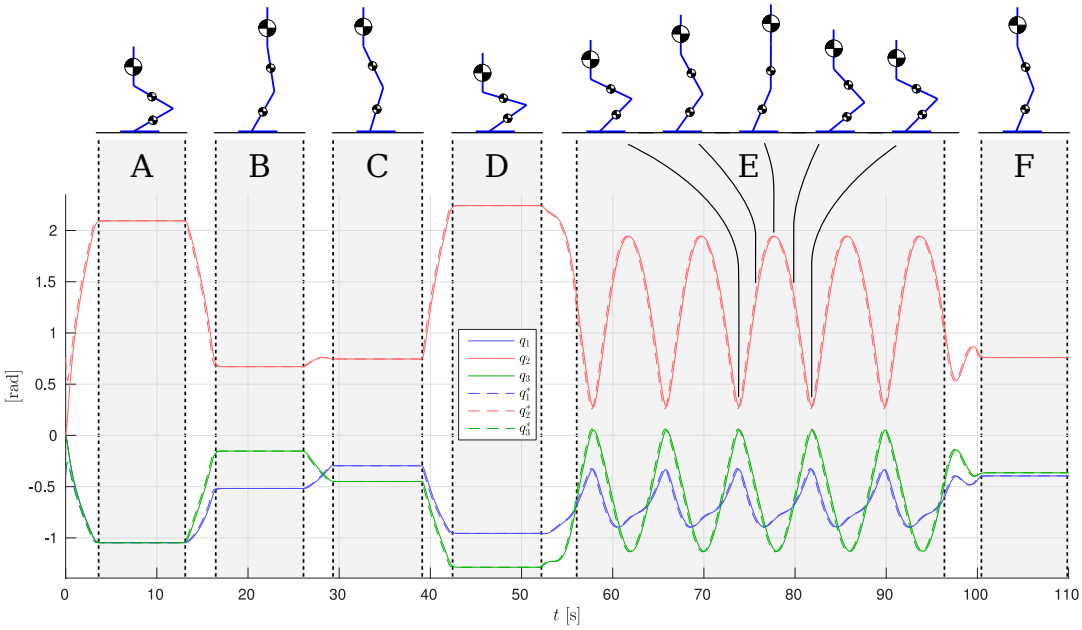

FIGURE 10.7: Joint references and tracking.

The robot is controlled with simple joint-level impedance controllers as high-level control strategy, providing the torque references for the gradient descent based controller of Sec. 10.2.2. As in Chapters 7 and 8, the SEAs are torque controlled to ensure the desired net torques are always achieved at the joints. We set the gradient descent

parameter $\gamma_e = 1 * 10^{-6}$, the constraint parameter $\gamma_{const} = 10^2$, and $\gamma_{dq} = 0.1$. The maximum pretension adjustment velocity of this system is approximately 3 cm/s, imposed by the transmission ratio, chosen electric motors and supply voltage of 48 V.

The results are shown in Fig. 10.7 and 10.8. The torque plots for the ankle (Fig. 10.8a and 10.8b) and knee (Fig. 10.8c and 10.8d) confirm that indeed the net torques $\boldsymbol{\tau}_1$ and $\boldsymbol{\tau}_2$ are nearly identical when comparing the mono- and biarticulated cases, showing that the SEAs can effectively ensure the desired net torque is achieved at the joints, and that the motions are comparable.

Considering on the torque provided by the parallel elastic tendons (red lines in Fig. 10.8a–10.8d) for both joints in both cases, they can be observed to converge to the net desired torque, causing the required SEA torque to converge to zero, unless the desired joint torque is not feasible given the tendon actuation topology. For example, negative ankle torques cannot be provided by the ankle tendon, causing the tendon torque to converge to zero and the SEA providing the full negative torque (e.g. phases C and D, where the center of pressure is behind the ankle joint and the ankle needs to provide negative torque). Furthermore, from the elastic element elongation shown in Fig. 10.8g and 10.8h, it can be observed that the constraint (Sec. 10.2.2) effectively constrains the unidirectional tendons to zero elongation. These results show the gradient descent based control approach is effective at achieving torque control of the system using (multi-)articulated compliant arrangements.

During the cyclic motion part of the reference, the tendon torques are unable to converge to the reference torque entirely, as the pretension adjustment speed limits do not allow for it (and the load motion compensation parameter $\gamma_{dq} = 0.1$); however, their smaller adjustments combined with the optimised design do lead to a substantial reduction of the error, causing the SEAs to need to deliver only a fraction of the net joint torque. This in turn allows to design for small, light, efficient motors. In the monoarticulated knee case, the SEA is providing less than 10 Nm peak torque out of approx. 70 Nm required net peak torque. In the biarticulated case, the SEAs

are providing less than 5 Nm on both the knee and ankle joints. In the monoarticulated ankle case, a smaller reduction in torque requirements is observed; the dependence of ankle load on the configuration of both joints results in the monoarticulated tendon not providing a torque that matches well with the required torque, despite substantial pretension adjustment of the ankle tendon (Fig. 10.8e).

Comparing the two actuation topologies, we observe that the biarticulated configuration is both able to provide the desired net joint torques more accurately, as well as needing significantly smaller pretension adjustments to achieve them. This conclusion is further strengthened by comparing the squared l_2-norm of the error for both cases, shown in Fig. 10.8i and 10.8j. We can therefore conclude that the biarticulated configuration is more suitable for the system under consideration.

10.4 Conclusions

This work has developed a novel model formulation of compliant actuation structures for articulated robots, including multiple branches and multi-articulation. The modular formulation employs a single matrix to describe the entire actuation topology, and formulates the energy exchange between the compliant elements and articulated multi-body robot dynamics using N-D power flows.

Using this formulation, we derived a novel gradient descent based control law for compliant actuation structures with adjustable pretension, with proven convexity for arbitrary actuation topologies. Unidirectional elastic elements were considered through the inclusion of a convex constraint into the formulation.

A simulation study on a model of the 3-DoF prototype leg presented in Chapter 9, using the mono- and biarticulated actuation topologies, reported that the gradient descent based control method is effective for torque control of the parallel tendons, leading to asymptotic convergence of the error. Additionally, the results illustrate that the chosen actuation topology and optimisation of its design parameters are also fundamental for optimal performance.

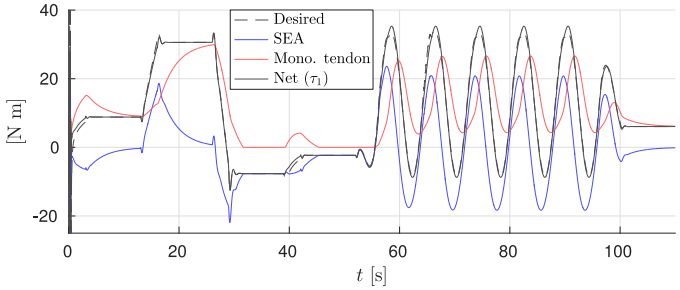

(A) Monoarticulated: Ankle (q_1) torques.

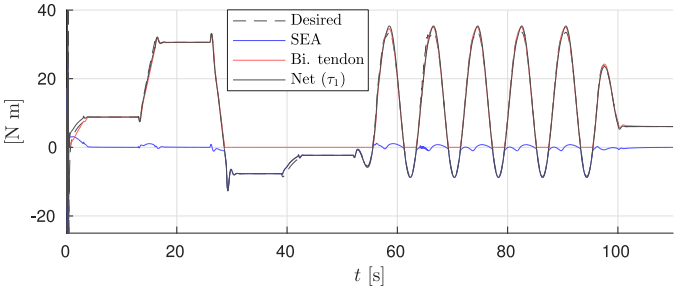

(B) Biarticulated: Ankle (q_1) torques.

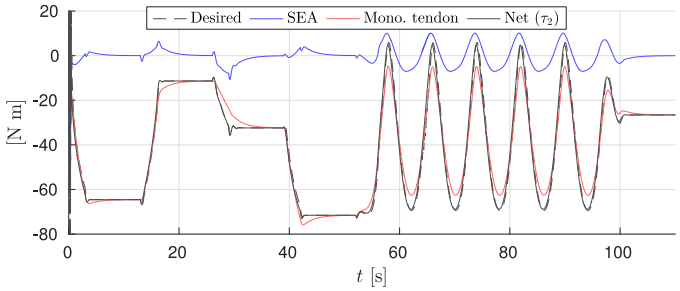

(C) Monoarticulated: Knee (q_2) torques.

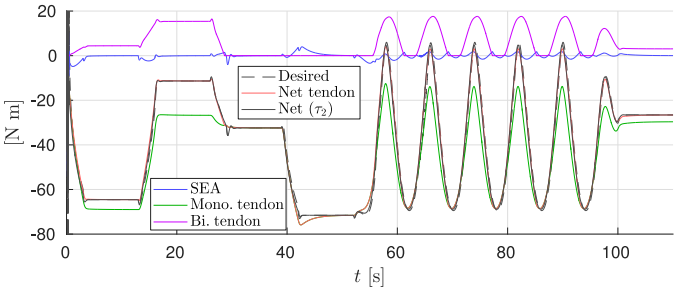

(D) Biarticulated: Knee (q_2) torques.

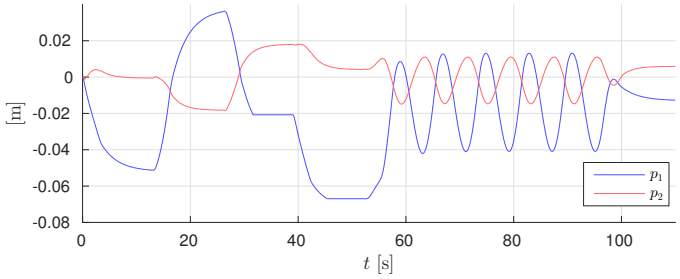

(E) Monoarticulated: Pretension positions.

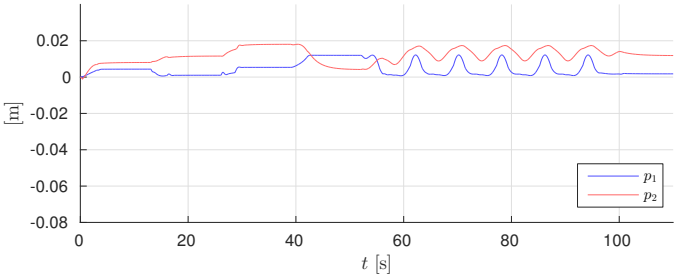

(F) Biarticulated: Pretension positions.

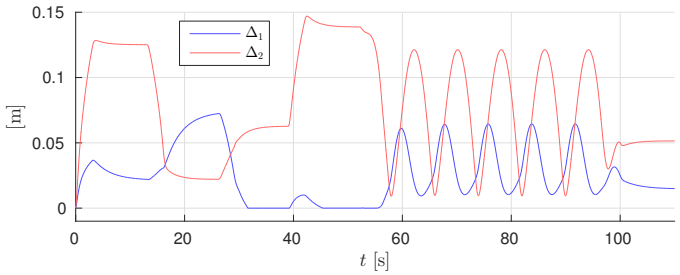

(G) Monoarticulated: Elastic element elongation.

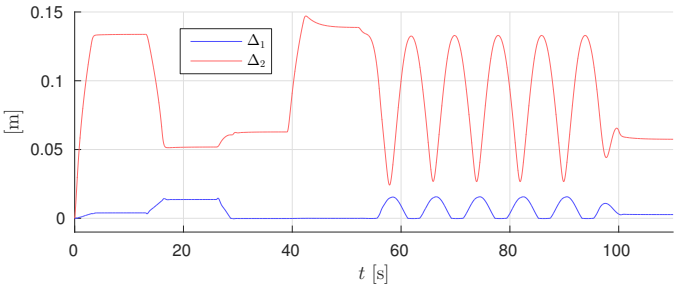

(H) Biarticulated: Elastic element elongation.

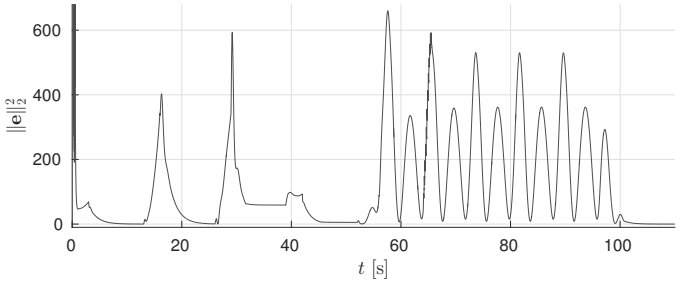

(I) Monoarticulated: Squared l_2-norm of error.

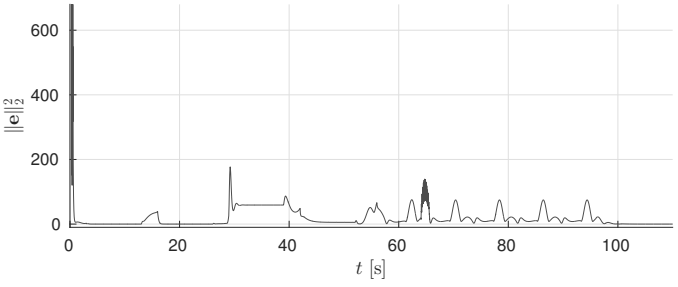

(J) Biarticulated: Squared l_2-norm of error.

FIGURE 10.8: Simulation results for gradient descent based control.

11

Conclusions & Future Work

This thesis has presented a number of contributions that advance the state-of-the-art in compliant robotic actuation. We have taken a two-part approach, within the overarching theme of high-performance compliant robotic actuation. Part I investigated the influence of design and control aspects on the performance of Series-Elastic Actuations (SEAs). Particularly, it investigated the influence of the choice of physical series stiffness on torque controllability, backdrivability/transparency, and impedance rendering. Furthermore, the robust torque control of SEAs through the use of disturbance observers was considered.

Part II considered the augmentation of articulated robots, driven by SEAs, with the addition of adjustable parallel compliance, including multiple branches and multi-articulation. Particularly, parallel compliance with adjustable pretension using secondary motors was considered. Building on a 1-DoF proof-of-concept, the concepts were extended and generalised towards multi-DoF and multi-articulated schemes.

A 3-DoF prototype leg was designed and used to effectively demonstrate the concepts on a real-world system, and advanced control concepts were introduced.

The work presented in this thesis gives rise to a number of open research questions. Hence, we suggest a number of areas for future work.

Further experimental validation of the work presented in Part I would be highly beneficial. Particularly, comparing impedance rendering capability in practice proved difficult; using a secondary motor driving the actuator externally, thereby imposing its output position, should provide further insight. Similarly, the comparison between different DOB structures presented in Chapter 5 would benefit from experimental data.

The optimality criterion for selecting SEA stiffness based on impedance rendering requirements, presented in Chapter 4, can be further extended by considering more criteria than impedance rendering bandwidth alone. Lastly, whereas the SEAs considered in this thesis are those with linear stiffness, the results suggest that nonlinear (stiffening) profiles may combine the low stiffness optimal for transparency with the high stiffness optimal for torque tracking.

With regards to Part II, many potential benefits remain to be explored. Firstly, at this point only initial experiments have been performed with the 3-DoF prototype hardware, which already demonstrated large energy efficiency increases. However, the inclusion of an integrated control strategy that actively utilises the adjustability of the parallel branches, such as those utilised in Chapters 8 and 10, is still underway and is expected to further increase the benefits of the proposed actuation structures. Secondly, while Chapter 10 contained a brief foray into other types of adjustability, such as variable transmission ratios, much work remains.

The systems used throughout Part II of this work have relied on relatively powerful series-elastic actuation as main drives, capable of actuating the robot even without the parallel compliant branches, to allow for direct comparison of the proposed concepts with state-of-the-art SEA based actuation. However, due to the significantly lower torque and power requirements imposed on the SEAs by using the parallel compliance, these can be designed differently. For example, gearbox ratios can be

reduced to improve achievable joint speeds. Alternatively, smaller, lighter and more energy efficient SEAs can be used, further increasing overall system performance.

A further benefit that was envisioned at the start of the works presented in Part II was the use of the parallel branches to improve the high-power performance of robotic systems, for example in explosive motions such as jumping. Work in this direction is currently underway.

The advanced control methods proposed in Chapter 10 lend themselves very well to the inclusion of energy expenditure; the magnitude of pretension adjustment can be considered in the context of energy consumed by the motors to do so. Furthermore, extensions towards predictive control in an energy efficiency context are promising.

Lastly, whereas in the systems considered in Part II series-elastic main drives were augmented with parallel elastic tendons, we believe effective systems can be designed that employ only such elastic tendons, in multi-articulated configurations, similar to the human anatomy.

Publications

This section lists conference and journal publications which are part of the dissemination of the work presented in this thesis, ordered by date and including accepted works (available on request).

- W. Roozing, "Modelling and Control of Adjustable Articulated Parallel Compliant Actuation Arrangements in Articulated Robots," *Frontiers in Bionics and Biomimetics: Advances in Mechatronics and Biomechanics towards Efficient Robot Actuation*, Accepted, 2018.
- W. Roozing, J. Malzahn, N. Kashiri, D. G. Caldwell, and N. G. Tsagarakis, "Design of a Novel 3-DoF Leg with Series and Parallel Compliant Actuation for Energy Efficient Articulated Robots," *IEEE/RSJ International Conference on Robotics and Automation (ICRA)*, Accepted, 2018.
- W. Roozing, J. Malzahn, N. Kashiri, D. G. Caldwell, and N. G. Tsagarakis, "On the Stiffness Selection for Torque Controlled Series-Elastic Actuators," in *IEEE Robotics and Automation Letters*, 2017.
- J. Malzahn, N. Kashiri, W. Roozing, N. G. Tsagarakis, and D. G. Caldwell "What is the Torque Bandwidth of this Actuator," in *Proceedings of the IEEE/RSJ International Conference on Intelligent Robots and Systems (IROS)*, 2017.
- W. Roozing, J. Malzahn, D. G. Caldwell, and N. G. Tsagarakis, "Comparison of open-loop and closed-loop disturbance observers for series elastic actuators," in *Proceedings of the IEEE/RSJ International Conference on Intelligent Robots and Systems (IROS)*, 2016.

- W. Roozing, Z. Li, D. G. Caldwell, and N. G. Tsagarakis, "Design Optimisation and Control of Compliant Actuation Arrangements in Articulated Robots for Improved Energy Efficiency," in *IEEE Robotics and Automation Letters*, vol. 1, no. 2, pp. 1110–1117, 2016.
- W. Roozing, Z. Li, G. A. Medrano-Cerda, D. G. Caldwell, and N. G. Tsagarakis, "Development and Control of a Compliant Asymmetric Antagonistic Actuator for Energy Efficient Mobility," in *IEEE/ASME Transactions on Mechatronics*, vol. 21, no. 2, pp. 1080–1091, 2015.
- N. G. Tsagarakis, H. Dallali, F. Negrello, W. Roozing, G. A. Medrano-Cerda, and D. G. Caldwell, "Compliant antagonistic joint tuning for gravitational load cancellation and improved efficient mobility," in *Proceedings of the 13th IEEE-RAS International Conference on Humanoid Robots (Humanoids)*, 2014.

Bibliography

[1] F. Negrello, M. Garabini, M. G. Catalano, J. Malzahn, D. G. Caldwell, A. Bicchi, and N. G. Tsagarakis, "A modular compliant actuator for emerging high performance and fall-resilient humanoids", IEEE, Nov. 2015, pp. 414–420, ISBN: 978-1-4799-6885-5. DOI: 10.1109/HUMANOIDS.2015.7363567.

[2] N. G. Tsagarakis, D. G. Caldwell, A. Bicchi, F Negrello, M Garabini, W Choi, L Baccelliere, V Loc, J Noorden, M Catalano, *et al.*, "Walk-man: A high performance humanoid platform for realistic environments", *Journal of Field Robotics (JFR)*, 2017.

[3] N. G. Tsagarakis, S. Morfey, H. Dallali, G. A. Medrano-Cerda, and D. G. Caldwell, "An asymmetric compliant antagonistic joint design for high performance mobility", in *Intelligent Robots and Systems (IROS), 2013 IEEE/RSJ International Conference on*, IEEE, 2013, pp. 5512–5517.

[4] N. G. Tsagarakis, H. Dallali, F. Negrello, W. Roozing, G. A. Medrano-Cerda, and D. G. Caldwell, "Compliant antagonistic joint tuning for gravitational load cancellation and improved efficient mobility", in *Humanoid Robots (Humanoids), 2014 14th IEEE-RAS International Conference on*, IEEE, 2014, pp. 924–929.

[5] G. A. Pratt and M. M. Williamson, "Series elastic actuators", in *Intelligent Robots and Systems 95.'Human Robot Interaction and Cooperative Robots', Proceedings. 1995 IEEE/RSJ International Conference on*, vol. 1, IEEE, 1995, pp. 399–406.

[6] M. Laffranchi, N. G. Tsagarakis, and D. G. Caldwell, "Safe human robot interaction via energy regulation control", in *Intelligent Robots and Systems, 2009. IROS 2009. IEEE/RSJ International Conference on*, IEEE, 2009, pp. 35–41.

[7] D. Vischer and O. Khatib, "Design and development of high-performance torque-controlled joints", *Robotics and Automation, IEEE Transactions on*, vol. 11, no. 4, pp. 537–544, 1995.

[8] H. Vallery, R. Ekkelenkamp, H. Van Der Kooij, and M. Buss, "Passive and accurate torque control of series elastic actuators", in *Intelligent Robots and Systems, 2007. IROS 2007. IEEE/RSJ International Conference on*, IEEE, 2007, pp. 3534–3538.

[9] R. Vertechy, A. Frisoli, M. Solazzi, A. Dettori, and M. Bergamasco, "Linear-quadratic-gaussian torque control: Application to a flexible joint of a rehabilitation exoskeleton", in *Robotics and Automation (ICRA), 2010 IEEE International Conference on*, IEEE, 2010, pp. 223–228.

[10] M. A. Hopkins, S. A. Ressler, D. F. Lahr, A. Leonessa, and D. W. Hong, "Embedded joint-space control of a series elastic humanoid", in *Intelligent Robots and Systems (IROS), 2015 IEEE/RSJ International Conference on*, IEEE, 2015, pp. 3358–3365.

[11] K. Kong, J. Bae, and M. Tomizuka, "Control of rotary series elastic actuator for ideal force-mode actuation in human-robot interaction applications", *IEEE/ASME Transactions on Mechatronics*, vol. 14, no. 1, pp. 105–118, Feb. 2009, ISSN: 1083-4435. DOI: 10.1109/TMECH.2008.2004561.

[12] N. Paine, S. Oh, and L. Sentis, "Design and control considerations for high-performance series elastic actuators", *IEEE/ASME Transactions on Mechatronics*, vol. 19, no. 3, pp. 1080–1091, Jun. 2014, ISSN: 1083-4435, 1941-014X. DOI: 10.1109/TMECH.2013.2270435.

[13] N. Paine, J. S. Mehling, J. Holley, N. A. Radford, G. Johnson, C.-L. Fok, and L. Sentis, "Actuator control for the NASA-JSC valkyrie humanoid robot: A decoupled dynamics approach for torque control of series elastic robots: Actuator control for the NASA-JSC valkyrie humanoid robot", *Journal of Field Robotics*, vol. 32, no. 3, pp. 378–396, May 2015, ISSN: 15564959. DOI: 10.1002/rob.21556.

[14] L. Baccelliere, N. Kashiri, L. Muratore, A. Laurenzi, M. Kamedula, A. Margan, S. Cordasco, J. Malzahn, and N. G. Tsagarakis, "Development of a human size and strength compliant bi-manual platform for realistic heavy manipulation

tasks", in *IEEE/RSJ International Conference on Intelligent Robots and Systems*, 2017.

[15] D. Paluska and H. Herr, "The effect of series elasticity on actuator power and work output: Implications for robotic and prosthetic joint design", *Robotics and Autonomous Systems*, vol. 54, no. 8, pp. 667–673, Aug. 2006, ISSN: 09218890. DOI: 10.1016/j.robot.2006.02.013.

[16] A. Velasco, G. M. Gasparri, M. Garabini, L. Malagia, P. Salaris, and A. Bicchi, "Soft-actuators in cyclic motion: Analytical optimization of stiffness and preload", *13th IEEE-RAS International Conference on Humanoid Robots (Humanoids)*, pp. 354 –361, 2013, ISSN: 2164-0572. DOI: 10.1109/HUMANOIDS.2013.7029999.

[17] A. Jafari, N. G. Tsagarakis, and D. G. Caldwell, "Exploiting natural dynamics for energy minimization using an actuator with adjustable stiffness (AwAS)", in *Robotics and Automation (ICRA), 2011 IEEE International Conference on*, IEEE, 2011, pp. 4632–4637.

[18] B. Vanderborght, N. G. Tsagarakis, C. Semini, R. Van Ham, and D. G. Caldwell, "Maccepa 2.0: Adjustable compliant actuator with stiffening characteristic for energy efficient hopping", in *Robotics and Automation, 2009. ICRA'09. IEEE International Conference on*, IEEE, 2009, pp. 544–549.

[19] M. Garabini, A. Passaglia, F. Belo, P. Salaris, and A. Bicchi, "Optimality principles in stiffness control: The VSA kick", in *Robotics and Automation (ICRA), 2012 IEEE International Conference on*, IEEE, 2012, pp. 3341–3346.

[20] A. Bicchi, G. Tonietti, M. Bavaro, and M. Piccigallo, "Variable stiffness actuators for fast and safe motion control", in *Robotics research*, Springer, 2005, pp. 527–536.

[21] D. W. Robinson, J. E. Pratt, D. J. Paluska, and G. A. Pratt, "Series elastic actuator development for a biomimetic walking robot", in *Advanced Intelligent Mechatronics, 1999. Proceedings. 1999 IEEE/ASME International Conference on*, IEEE, 1999, pp. 561–568.

[22] A. Calanca, R. Muradore, and P. Fiorini, "A review of algorithms for compliant control of stiff and fixed-compliance robots", *IEEE/ASME Transactions on*

Mechatronics, vol. 21, no. 2, pp. 613–624, 2015, ISSN: 1083-4435, 1941-014X. DOI: 10.1109/TMECH.2015.2465849.

[23] H. Vallery, J. Veneman, E. van Asseldonk, R. Ekkelenkamp, M. Buss, and H. van Der Kooij, "Compliant actuation of rehabilitation robots", *IEEE Robotics & Automation Magazine*, vol. 15, no. 3, pp. 60–69, Sep. 2008, ISSN: 1070-9932. DOI: 10.1109/MRA.2008.927689.

[24] A. Jafari, N. G. Tsagarakis, and D. G. Caldwell, "A novel intrinsically energy efficient actuator with adjustable stiffness (AwAS)", *IEEE/ASME Transactions on Mechatronics*, vol. 18, no. 1, pp. 355–365, Feb. 2013, ISSN: 1083-4435, 1941-014X. DOI: 10.1109/TMECH.2011.2177098.

[25] M. Laffranchi, N. G. Tsagarakis, and D. G. Caldwell, "Analysis and development of a semiactive damper for compliant actuation systems", *IEEE/ASME Transactions on Mechatronics*, vol. 18, no. 2, pp. 744–753, Apr. 2013, ISSN: 1083-4435, 1941-014X. DOI: 10.1109/TMECH.2012.2184293.

[26] R. Van Ham, B. Vanderborght, M. Van Damme, B. Verrelst, and D. Lefeber, "MACCEPA, the mechanically adjustable compliance and controllable equilibrium position actuator: Design and implementation in a biped robot", *Robotics and Autonomous Systems*, vol. 55, no. 10, pp. 761–768, Oct. 2007, ISSN: 09218890. DOI: 10.1016/j.robot.2007.03.001.

[27] S. Wolf, O. Eiberger, and G. Hirzinger, "The DLR FSJ: Energy based design of a variable stiffness joint", in *Robotics and Automation (ICRA), 2011 IEEE International Conference on*, IEEE, 2011, pp. 5082–5089.

[28] S. S. Groothuis, G. Rusticelli, A. Zucchelli, S. Stramigioli, and R. Carloni, "The variable stiffness actuator vsaUT-II: Mechanical design, modeling, and identification", *IEEE/ASME Transactions on Mechatronics*, vol. 19, no. 2, pp. 589–597, Apr. 2014, ISSN: 1083-4435, 1941-014X. DOI: 10.1109/TMECH.2013.2251894.

[29] A. Jafari, N. G. Tsagarakis, I. Sardellitti, and D. G. Caldwell, "A new actuator with adjustable stiffness based on a variable ratio lever mechanism", *IEEE/ASME Transactions on Mechatronics*, vol. 19, no. 1, pp. 55–63, Feb. 2014, ISSN: 1083-4435, 1941-014X. DOI: 10.1109/TMECH.2012.2218615.

[30] R. Schiavi, G. Grioli, S. Sen, and A. Bicchi, "VSA-II: A novel prototype of variable stiffness actuator for safe and performing robots interacting with humans", in *Robotics and Automation, 2008. ICRA 2008. IEEE International Conference on*, IEEE, 2008, pp. 2171–2176.

[31] M. W. Spong, "Control of flexible joint robots: A survey", *Coordinated Science Laboratory Report no. DC-116 (UILU-ENG 90-2203)*, 1990.

[32] J. W. Sensinger and R. F. F. Weir, "Improvements to series elastic actuators", in *2006 2nd IEEE/ASME International Conference on Mechatronics and Embedded Systems and Applications*, IEEE, 2006, pp. 1–7.

[33] A. Calanca and P. Fiorini, "On the role of compliance in force control", in *Proceedings of the 13th International Conference on Intelligent Autonomous Systems*, E. Menegatti, N. Michael, K. Berns, and H. Yamaguchi, Eds., vol. 302, DOI: 10.1007/978-3-319-08338-4_90, Cham: Springer International Publishing, 2016, pp. 1243–1255, ISBN: 978-3-319-08337-7 978-3-319-08338-4.

[34] T. Boaventura, M. Focchi, M. Frigerio, J. Buchli, C. Semini, G. A. Medrano-Cerda, and D. G. Caldwell, "On the role of load motion compensation in high-performance force control", in *2012 IEEE/RSJ International Conference on Intelligent Robots and Systems*, IEEE, 2012, pp. 4066–4071.

[35] M. Hutter, C. Gehring, D. Jud, A. Lauber, C. D. Bellicoso, V. Tsounis, J. Hwangbo, K. Bodie, P. Fankhauser, M. Bloesch, and others, "ANYmal-a highly mobile and dynamic quadrupedal robot", in *Intelligent Robots and Systems (IROS), 2016 IEEE/RSJ International Conference on*, IEEE, 2016, pp. 38–44.

[36] M. Focchi, G. A. Medrano-Cerda, T. Boaventura, M. Frigerio, C. Semini, J. Buchli, and D. G. Caldwell, "Robot impedance control and passivity analysis with inner torque and velocity feedback loops", *Control Theory and Technology*, vol. 14, no. 2, pp. 97–112, May 2016, ISSN: 2095-6983, 2198-0942. DOI: 10.1007/s11768-016-5015-z.

[37] A. Albu-Schaffer, C. Ott, and G. Hirzinger, "A unified passivity-based control framework for position, torque and impedance control of flexible joint robots", *The International Journal of Robotics Research*, vol. 26, no. 1, pp. 23–39, Jan. 1, 2007, ISSN: 0278-3649. DOI: 10.1177/0278364907073776.

[38] H. S. Lee and M. Tomizuka, "Robust motion controller design for high-accuracy positioning systems", *Industrial Electronics, IEEE Transactions on*, vol. 43, no. 1, pp. 48–55, 1996.

[39] H. Shim and N. H. Jo, "An almost necessary and sufficient condition for robust stability of closed-loop systems with disturbance observer", *Automatica*, vol. 45, no. 1, pp. 296–299, Jan. 2009, ISSN: 00051098. DOI: 10.1016/j.automatica.2008.10.009.

[40] Youngjin Choi, Kwangjin Yang, Wan Kyun Chung, Hong Rok Kim, and Il Hong Suh, "On the robustness and performance of disturbance observers for second-order systems", *IEEE Transactions on Automatic Control*, vol. 48, no. 2, pp. 315–320, Feb. 2003, ISSN: 0018-9286. DOI: 10.1109/TAC.2002.808491.

[41] C. J. Kempf and S. Kobayashi, "Disturbance observer and feedforward design for a high-speed direct-drive positioning table", *Control Systems Technology, IEEE Transactions on*, vol. 7, no. 5, pp. 513–526, 1999.

[42] W. Roozing and J. Malzahn, *Compliant joint toolbox (CJT) - available on GitHub: Https://github.com/geez0x1/CompliantJointToolbox*, 2017.

[43] U. Mettin, P. X. La Hera, L. B. Freidovich, and A. S. Shiriaev, "Parallel elastic actuators as a control tool for preplanned trajectories of underactuated mechanical systems", *The International Journal of Robotics Research*, vol. 29, no. 9, pp. 1186–1198, Aug. 2010, ISSN: 0278-3649, 1741-3176. DOI: 10.1177/0278364909344002.

[44] D. F. B. Haeufle, M. D. Taylor, S. Schmitt, and H. Geyer, "A clutched parallel elastic actuator concept: Towards energy efficient powered legs in prosthetics and robotics", in *Biomedical Robotics and Biomechatronics (BioRob), 2012 4th IEEE RAS & EMBS International Conference on*, IEEE, 2012, pp. 1614–1619.

[45] G. Mathijssen, D. Lefeber, and B. Vanderborght, "Variable recruitment of parallel elastic elements: Series-parallel elastic actuators (SPEA) with dephased mutilated gears", *IEEE/ASME Transactions on Mechatronics*, vol. 20, no. 2, pp. 594–602, Apr. 2015, ISSN: 1083-4435, 1941-014X. DOI: 10.1109/TMECH.2014.2307122.

[46] M. Plooij, M. Wisse, and H. Vallery, "Reducing the energy consumption of robots using the bidirectional clutched parallel elastic actuator", *IEEE Transactions on Robotics*, vol. 32, no. 6, pp. 1512–1523, Dec. 2016, ISSN: 1552-3098, 1941-0468. DOI: 10.1109/TRO.2016.2604496.

[47] G. Mathijssen, T. Verstraten, B. Brackx, J. Premec, D. Lefeber, B. Vanderborght, and others, "+ SPEA introduction: Drastic actuator energy requirement reduction by symbiosis of parallel motors, springs and locking mechanisms", in *2016 IEEE International Conference on Robotics and Automation (ICRA)*, IEEE, 2016, pp. 676–681.

[48] X. Liu, A. Rossi, and I. Poulakakis, "SPEAR: A monopedal robot with switchable parallel elastic actuation", in *Intelligent Robots and Systems (IROS), 2015 IEEE/RSJ International Conference on*, IEEE, 2015, pp. 5142–5147.

[49] T. Yang, E. R. Westervelt, J. P. Schmiedeler, and R. A. Bockbrader, "Design and control of a planar bipedal robot ERNIE with parallel knee compliance", *Autonomous Robots*, vol. 25, no. 4, pp. 317–330, Nov. 2008, ISSN: 0929-5593, 1573-7527. DOI: 10.1007/s10514-008-9096-5.

[50] A. Mazumdar, S. J. Spencer, C. Hobart, J. Salton, M. Quigley, T. Wu, S. Bertrand, J. Pratt, and S. P. Buerger, "Parallel elastic elements improve energy efficiency on the STEPPR bipedal walking robot", *IEEE/ASME Transactions on Mechatronics*, pp. 1–1, 2016, ISSN: 1083-4435, 1941-014X. DOI: 10.1109/TMECH.2016.2631170.

[51] S. Shirata, A. Konno, and M. Uchiyama, "Design and evaluation of a gravity compensation mechanism for a humanoid robot", in *Intelligent Robots and Systems, 2007. IROS 2007. IEEE/RSJ International Conference on*, IEEE, 2007, pp. 3635–3640.

[52] S. Au, J. Weber, and H. Herr, "Powered ankle–foot prosthesis improves walking metabolic economy", *IEEE Transactions on Robotics*, vol. 25, no. 1, pp. 51–66, Feb. 2009, ISSN: 1552-3098, 1941-0468. DOI: 10.1109/TRO.2008.2008747.

[53] R. Jimenez-Fabian, J. Geeroms, L. Flynn, B. Vanderborght, and D. Lefeber, "Reduction of the torque requirements of an active ankle prosthesis using a parallel spring", *Robotics and Autonomous Systems*, vol. 92, pp. 187–196, Jun. 2017, ISSN: 09218890. DOI: 10.1016/j.robot.2017.03.011.

[54] J. Realmuto, G. Klute, and S. Devasia, "Nonlinear passive cam-based springs for powered ankle prostheses", *Journal of Medical Devices*, vol. 9, no. 1, p. 011 007, 2015.

[55] E. J. Rouse, L. M. Mooney, E. C. Martinez-Villalpando, and H. M. Herr, "Clutchable series-elastic actuator: Design of a robotic knee prosthesis for minimum energy consumption", in *Rehabilitation Robotics (ICORR), 2013 IEEE International Conference on*, IEEE, 2013, pp. 1–6.

[56] S. Pfeifer, A. Pagel, R. Riener, and H. Vallery, "Actuator with angle-dependent elasticity for biomimetic transfemoral prostheses", *IEEE/ASME Transactions on Mechatronics*, vol. 20, no. 3, pp. 1384–1394, Jun. 2015, ISSN: 1083-4435, 1941-014X. DOI: 10.1109/TMECH.2014.2337514.

[57] S. Wang, W. van Dijk, and H. van der Kooij, "Spring uses in exoskeleton actuation design", in *Rehabilitation Robotics (ICORR), 2011 IEEE International Conference on*, IEEE, 2011, pp. 1–6.

[58] M. Vermeulen and M. Wisse, "Intrinsically safe robot arm: Adjustable static balancing and low power actuation", *International Journal of Social Robotics*, vol. 2, no. 3, pp. 275–288, Sep. 2010, ISSN: 1875-4791, 1875-4805. DOI: 10.1007/s12369-010-0048-9.

[59] Y. Yesilevskiy, W. Xi, and C. D. Remy, "A comparison of series and parallel elasticity in a monoped hopper", in *Robotics and Automation (ICRA), 2015 IEEE International Conference on*, IEEE, 2015, pp. 1036–1041.

[60] P. Beckerle, T. Verstraten, G. Mathijssen, R. Furnemont, B. Vanderborght, and D. Lefeber, "Series and parallel elastic actuation: Influence of operating positions on design and control", *IEEE/ASME Transactions on Mechatronics*, vol. 22, no. 1, pp. 521–529, Feb. 2017, ISSN: 1083-4435, 1941-014X. DOI: 10.1109/TMECH.2016.2621062.

[61] M. Grimmer, M. Eslamy, S. Gliech, and A. Seyfarth, "A comparison of parallel- and series elastic elements in an actuator for mimicking human ankle joint in walking and running", in *Robotics and Automation (ICRA), 2012 IEEE International Conference on*, IEEE, 2012, pp. 2463–2470.

[62] G. J.V. I. Schenau, "From rotation to translation: Constraints on multi-joint movements and the unique action of bi-articular muscles", *Human Movement Science*, vol. 8, no. 4, pp. 301–337, 1989.

[63] B. I. Prilutsky and V. M. Zatsiorsky, "Tendon action of two-joint muscles: Transfer of mechanical energy between joints during jumping, landing, and running", *Journal of biomechanics*, vol. 27, no. 1, pp. 25–34, 1994.

[64] T. J. Klein and M. A. Lewis, "A robot leg based on mammalian muscle architecture", in *Robotics and Biomimetics (ROBIO), 2009 IEEE International Conference on*, IEEE, 2009, pp. 2521–2526.

[65] F. Iida, J. Rummel, and A. Seyfarth, "Bipedal walking and running with spring-like biarticular muscles", *Journal of Biomechanics*, vol. 41, no. 3, pp. 656–667, Jan. 2008, ISSN: 00219290. DOI: 10.1016/j.jbiomech.2007.09.033.

[66] R. Niiyama, A. Nagakubo, and Y. Kuniyoshi, "Mowgli: A bipedal jumping and landing robot with an artificial musculoskeletal system", in *Robotics and Automation, 2007 IEEE International Conference on*, IEEE, 2007, pp. 2546–2551.

[67] V. Salvucci, Y. Kimura, S. Oh, T. Koseki, and Y. Hori, "Comparing approaches for actuator redundancy resolution in biarticularly-actuated robot arms", *IEEE/ASME Transactions on Mechatronics*, vol. 19, no. 2, pp. 765–776, Apr. 2014, ISSN: 1083-4435, 1941-014X. DOI: 10.1109/TMECH.2013.2257826.

[68] F. C. Loeffl, A. Werner, D. Lakatos, J. Reinecke, S. Wolf, R. Burger, T. Gumpert, F. Schmidt, C. Ott, M. Grebenstein, and others, "The DLR c-runner: Concept, design and experiments", 2016.

[69] J. Babič, B. Lim, D. Omrčen, J. Lenarčič, and F. C. Park, "A biarticulated robotic leg for jumping movements: Theory and experiments", *Journal of Mechanisms and Robotics*, vol. 1, no. 1, p. 011 013, 2009, ISSN: 19424302. DOI: 10.1115/1.2963028.

[70] A. Tözeren, *Human body dynamics: classical mechanics and human movement*. New York: Springer, 2000, 315 pp., ISBN: 978-0-387-98801-6.